Stony Brook University

Synthesis and Characterization of Nanostructured Metal Oxide for Water Remediation and Energy Applications

A Dissertation Presented

by

Jusang Lee

to

The Graduate School

in Partial Fulfillment of the

Requirements

for the Degree of

Doctor of Philosophy

in

Materials Science and Engineering

Stony Brook University

December 2013

Stony Brook University

The Graduate School

Jusang Lee

We, the dissertation committee for the above candidate for the

Doctor of Philosophy degree, hereby recommend

acceptance of this dissertation.

Prof. Pelagia-Irene (Perena) Gouma - Dissertation Advisor
Professor, Materials Science and Engineering

Prof. Aisha S. Haynes- Chairperson of Defense
Adjunct Professor, Materials Science and Engineering

Prof. Maen Alkhader
Assistant Professor, Mechanical Engineering

Dr. Mingzhao Liu
Staff Scientist, BNL- Center for Functional Nanomaterials

This dissertation is accepted by the Graduate School

Charles Taber
Interim Dean of the Graduate School

Abstract of the Dissertation

Synthesis and Characterization of Nanostructured Metal Oxide for Energy and Environmental Remediation Applications.

by

Jusang Lee

Doctor of Philosophy

in

Materials Science and Engineering

Stony Brook University

2013

Over the last few decades environmental pollution and energy consumption has been increasing as a result of a rapidly growing population and global industrialization. Consequently, finding novel and eco-friendly methods of cleaning the environment and exploiting clean energy sources has become a necessity. This thesis focuses on nanostructured materials that are tailored to provide affordable and efficient means for environmental remediation and which may also facilitate clean energy production. Identifying and synthesizing the appropriate nanomaterials in large scale are key issues that determine the adoption of nanotechnology solution to environmental problems and sustainability. This work has identified nanostructured metal oxides photocatalysts of the CuO and/or WO_3, TiO_2 to be appropriate and advanced nanomaterials for the water clean up from pollutants (such as petroleum hydrocarbons and chemical dyes) and the novel synthesis and characterization of these materials is described in detail.

At first, CuO-TiO_2 nanofibrous mats were fabricated by blend electrospinning using a sol-gel precursor. The photocatalytic activities of the pure TiO_2 and CuO-TiO_2 nanofibrous mats catalysts have been demonstrated under UV light and under visible light. The UV-Vis

spectroscopy results indicated that, based on the degradation of methylene blue (MB) dye solutions, the nanofibrous mats are strongly effective visible-light activated photocatalysts that offer 97% dye degradation under such irradiation. The relatively high photocurrent-to-dark-current contrast ratio and the fast responses observed also suggest that the CuO-TiO_2 nanofibrous mats described are potentially useful for highly efficient visible light-activated photocatalysts for environmental and energy applications.

CuO nanogrids were synthesized by direct thermal oxidation of composite substrates consisting of a Cu mesh and PVP nanofibers deposited on it by electrospinning. The unique nanogrids architecture results from the templating action of electrospun nanomats of polymers deposited on the metallic mesh. The estimated band gap energy is ~1.33eV, which is larger than the reported value for bulk CuO (E_g= 1.2eV).

$CuWO_4$ (n- type)–CuO (p-type) nanostructured photocatalysts were synthesized by sol-gel processing. The $CuWO_4$–CuO nanocatalysts are 20-800 nm of diameter with porous surfaces. Photocatalytic test on benzene degradation under natural light showed that a reduction in the concentration of benzene from 43,825 to 2.8 ppm within 3 days. The photocatalytic degradation of methlyene blue using the $CuWO_4$-CuO system resulted in 80% reduction which is better (and faster) that commercial TiO_2. The $CuWO_4$–CuO catalyst generated a photocurrent 140 nA/cm^2 under simulated sun light with 0.1 M benzoic acid/0.1 M KOH.

Finally, nonwoven cellulose acetate (CA) nanofibrous mats were prepared by electrospining process for selective oil sorbent to be interfaced with the photocatalytic nanogrids. The morphology and chemical analysis have done by scanning electron microscope (SEM) and Fourier transform infrared spectroscopy (FT-IR). The sorption capacity results of the CA nanofibrous sorbent for No. 6 fuel oil, vegetable oil, and benzene showed 44, 33, and 22 g/g, respectively. The CA mats have hydrophobic surface with a contact angle 137^o and high buoyancy. The electrospun CA fiber mats is biodegradable, high sorption capacity, fast, and cost-effective solution to remediate oil spill in aqueous environment and potential template of nanostructued catalysts.

The results of the work in this thesis provide very useful information on the impact of morphology and chemical composition on nanostructured metal oxide for catalytic activity. The mechanism we found here could help in the design and tailoring of new types of nanostructured metal oxide for energy and environmental remediation applications.

Dedicate to

My Family

Table of Contents

Contents

List of Figures

List of Abbreviations

3D: Three-dimensional
BET: Brunauer-Emmett-Teller
DSC: Differential Scanning Calorimetry
DTA: Differential Thermal Analysis (DTA)
EDS: Energy dispersive spectrum
FSP: Flame-spray pyrolysis
GC-MS: Gas chromatograph mass spectrometry
HRTEM: High Resolution Transmission Electron Microscopy
JCPDS: Joint Committee on Powder Diffraction Standards
RT: Room temperature
SA: Surface area
SAD/SAED: Selected Area Diffraction/Selected Area Electron Diffraction
SEM: Scanning electron microscopy
SIFT-MS: Selected ion flow tube mass spectrometry
TEM: Transmission Electron Microscopy
TGA: Thermo Gravimetric Analysis
VOC: Volatile Organic Compound
XPS: X-ray photoelectron spectroscopy
XRD: X-ray Diffraction

EC: Conduction band edge
EV: Valence band edge
EF: Fermi energy level
EC0: Conduction band edge before charge transfer from the surface states
EV0: Valence band edge before charge transfer from the surface states
EF0: Fermi energy level before charge transfer from the surface states
LD: Debye length

Acknowledgments

I would like to extend my sincerest gratitude to Prof. P. I. Gouma. Prof. Gouma has been a great mentor throughout the whole period of my graduate study in all aspects. Prof. Gouma's insights, enthusiasm and inspiration have been a true blessing for me. I had numerous opportunities to meet brilliant scientists and work on interesting projects which inspire me a lot.

Many thanks to Dr. Aisha S. Haynes for serving on my defense committee member and her supports during the project. I am very grateful to Dr. Mingzhao Liu for his valuable teach on electrochemistry and hospitality during my visit to Brookhaven National Laboratory (BNL).

I would like to thank Dr. Maen Alkhader for agreeing to serve as a defense committee member. Special thanks to Dr. Quinn for teaching me all the analytical techniques. I would thank like to extend my thanks to my group members Gagan, Shantanu, Selda, Jiahao, Jing, Lynne, Guokuo, Lei, Ruiyao, Zhuolin and former lab member Lisheng, Ruipeng.

Most of all I would like to thank my family for their love and support for me at all times.

Vita

Jusang Lee

EDUCATION

State University of New York at Stony Brook, Stony Brook, New York.
Master of Science, Materials Science and Engineering
Graduated in April 2009
Bachelor of Engineering, Engineering Science
State University of New York at Stony Brook, Stony Brook, New York.

- Engineering Licensure *(EIT)* - Fundamentals of Engineering (FE)
  Apr 2009, New York. (*passed*)

RESEARCH EXPERIENCE

Stony Brook University
Stony Brook, New York
Center for Nanomaterials and Sensor Development (CNSD)
Mar 2008 – Current
(*http://cnsd.matscieng.sunysb.edu*)

- Developing synthesis methods for composite nanofibers using electrospinning and sol- gel process.
- Testing and analyzing TiO_2 chemical sensor in oxidizing/reducing gases.
- Synthesizing 3-D CuO nano-networks for chemosensor and catalyst applications.
- Synthesizing and characterizing visible light- activated oxide photocatalysts.
- Fabricating copper doped epsilon-WO_3 sensor using flame spray pyrolysis for acetone detection.
- Synthesis and characterizing hydrophobic Cellulose acetate (CA) nanocompotie for oil sorbent application.

Brookhaven National Laboratory
Upton ,New York
Center for Functional Nanomaterials(CFN)
Sep 2011–Current

- Investigated surface and interface properties of single crystal/polycrystalline metal oxide and thin films semiconductors.
- Characterized metal oxide semiconductor and thin films, including surface morphology, structure, optical and electric chemical properties.
- Proficient in advanced characterization tools: Electrons microscopy (SEM-EDX, TEM-SEAD; including sample preparation), X-ray techniques (XRD), Spectroscopic characterization (Raman, FT-IR, UV-Vis) and Electrochemical analysis (Cyclic Voltammetry)

Stony Brook University
Stony Brook, New York
Environmental Nanotechnology Research Group
May 2007 - Dec 2007

- Chitosan composites analysis using Raman for dental application.
- Raman analysis on gold nanoparticle coated self cleaning fabrics.

PROFESSIONAL EXPERIENCE

Gouma Inc.(Start-up company) Position: *Chief Research Scientist/ Project Manager*
Jan 2013- Current

- Directing and overseeing all experimental activities on synthesizing visible light activated nanogrids photocatalysts.
- Electrochemical characterizing and testing final product in benzene contaminated water.
- Talking and giving presentations to potential investors for fundraising.

AWARDS

National Science Foundation Innovation Corps (NSF I-Corps)
Oct 2011 (Award # 1156513, Position: Entrepreneurial Lead)

- Investigate commercialization prospects of nanogrids photocatalyst for water remediation. Worked done in conjunction with help of Stanford University's Innovation Corps program.
  "Photocatalysts for Water Remediation", I-Corps team, Stanford University, Palo Alto, CA.

National Science Foundation Small Business Innovation Research I (NSF SBIR I)
Jan 2013 (Award #: 1248807, Position: Principal Investigator)

- Further develop the Gouma Inc's visible-light activated photocatalytic nanofiber mesh technology to clean up hydrocarbon contamination in produced water resulting from oil and gas drilling operations, such as fracking.

Research Fellowship Award - SUNY-Stony Brook
Jun 2009- Dec 2013

REFEREED JOURNAL ARTICLES AND BOOK CHAPTERS

- **Jusang Lee** and Pelagia I. Gouma, "Tailored 3D CuO Nanogrid Formation," Journal of Nanomaterials, vol. 2011, Article ID 863631, 6 pages, 2011. doi10.11552011863631
- **Lee, J.** and Gouma, P. I. (2012), *Sol-gel processed oxide photocatalysts, In Klein, L., Aparicio, M., and Jitianu, A.,*Sol-Gel Processing for Conventional and Alternative Energy (Rev. ed., pp. 217-237), Advances in Sol-Gel Derived Materials and Technologies, New York: Springer.
- **Lee, J**., Divya, S., Shanmugasundaram, P., and Gouma, P.I., Synthesis and Characterization of Visible-Light activated CuO-TiO_2 nanofibrous mats, *Journal of Nanoengineering and Nanomanufacturing (JNAN),* accepted.
- **Lee, J**. and Gouma, P.I. Hydrophobic Fibrous Cellulose Acetate (CA) Mats as Oil Selective Sorbents, *Journal of Materials Science (JMSC),* submitted 10-13-13.

PATENTS AND INVENTION DISCLOSURES

- P. I. Gouma, **Jusang Lee**, "Fiber mats coated with nanogrid visible spectrum photocatalysts for absorption, recovery and oxidative degradation of hydrocarbons", PCT/US12/44327 filed June 27, 2012

– P. I. Gouma, **Jusang Lee**, "Nanogrids for Water Remediation", Invention disclosure, Date: Oct 03, 2011, SUNY-Stony Brook, Reference R-8396

CONFERENCE / ACHIEVEMENT

- "A novel method for synthesis of 3-D WO_3-CuO nanogrids", International Symposium on Olfaction and Electronic Nose (ISOEN 2011), May 2011, NY.
- "Metal oxide photocatalysis under visible light", *Materials* Research Society Symposium *(MRS Fall 2010)*, Dec 2010, Boston, MA.
- "Self supported 3D ceramic photocatalytic nanogrids", Advanced Energy Conference 2010, Nov 2010, New York, NY.
- "Metal oxide photocatalysis for oil decomposition" ,Gulf Oil Spill Conference, Nov 2010, New Orleans, LA
- "Grow Mechanism of 3-D CuO Nanogrids", Undergraduate Research & Creative Activities (URECA) Apr 2008, Stony Brook University, NY.
- "Electrospinning Metal Oxide Nanogrids", Young Investigators Symposium, Nov 2008, Stony Brook University, NY.

TECHNICAL TALK

- **"**Nanosensors and breathalyzers for personalized diagnostics", International Conference on Nanoscience and Technology (ICN+T 2013), Sep 2013, Paris, France.
- "Photocatalytic Activity and Characterization of 3D CuWO4", International Conference on Electrospinning 2012, May 2012, Jeju, Korea.
- "Ferroelectric WO_3 Nanostructures for Nanoelectronics", *Materials Research Society Symposium (MRS Fall 2010)*, Dec 2010, Boston, MA.
- "Tailored 3D CuO Nanogrids Formation for Sensors and Photocatalysts", International Congress on Ceramics (ICC3), Nov 2010, Osaka, Japan.

RELATED SKILL

Fabrication Methods: Wet-Chemical (Sol-Gel), Thin Film (Spin Coating, ALD, and PVD), Nanofabrication (Electrospinning, and Flame Spray Pyrolysis)

Characterization Methods: X-ray Techniques (XRD), Electrons Microscopy (STEM/TEM-SAED, SEM-EDX), Electrochemical Analysis (Cyclic Voltammetry), Optical Spectroscopy (Raman, FT-IR, UV-Vis), and Thermal Analysis (DSC, TGA).

Language: Fluent in English and Korean, Familiar with conversational Japanese.

TEACHING EXPERIENCE

Teaching Assistant, C Programming for Engineers - Fall 2010, Fall 2011, Spring 2012

Teaching Assistant, Electron Microscope-Spring 2011

Chapter 1 Introduction

1.1. Basic principles of photocatalysis using semiconducting oxides

A semiconductor photocatalyst absorbs light with photon energies that are the same or greater than the band gap, $h\nu \geq E_g$, causing electron excitation from the valence band (VB) to the conduction band (CB) of the photocatalyst leaving behind holes (see Figure 1.1) [1]. The activation equation can be written as:

$$TiO_2 + h\nu \rightarrow h^+ + e^- \text{ (Charge Separation)}$$

Photogenerated h^+ and e^- are capable of oxidizing or reducing a surface-adsorbed substrate, forming a singly oxidized electron donor and singly reduced electron acceptor, super oxide $O_2 \bullet^-$ and hydroxyl radical $OH \bullet$:

$$h^+ + OH^- \rightarrow OH \bullet$$

$$e^- + O_{2\,ads} \rightarrow O_2 \bullet^-$$

The relation between energy of photon (E) and threshold wavelength (λ_g), which is the greatest wavelength of radiation for a specified surface for the emission of electrons, can be described by Planck's relation:

$$E = h\nu$$

where h is the Planck's constant, ν ($=c/\lambda_g$) is the frequency and c is speed of light . Therefore, the threshold wavelength (λ_g) also can be expressed as

$$\lambda_g = \frac{hc}{E_g}$$

As an example, the two phases of TiO_2 that is the polymorphs anatase and rutile have different band gaps E_g (anatase) =3.20eV and E_g (rutile) =3.02eV and as such have absorption thresholds of 380 and 410 nm, respectively [2].

Once the charge separation occurs, the photogenerated electron and hole can follow several path ways. Figure 1.1 illustrates the photo-excitation in a semiconductor particle followed by deexcitation events. At the surface of particle, the excited electron can reduce an electron acceptor (a) and a hole can combine with the electron donor species (b). The photogenerated electrons and holes recombination also occurs on the surface (c) and in the volume of particle (d). (The electron transferring process from the adsorbate to the semiconductor is referred as the oxidation mechanism, whereas electron transferring process from the semiconductor to the adsorbate is referred as the reduction mechanism.)

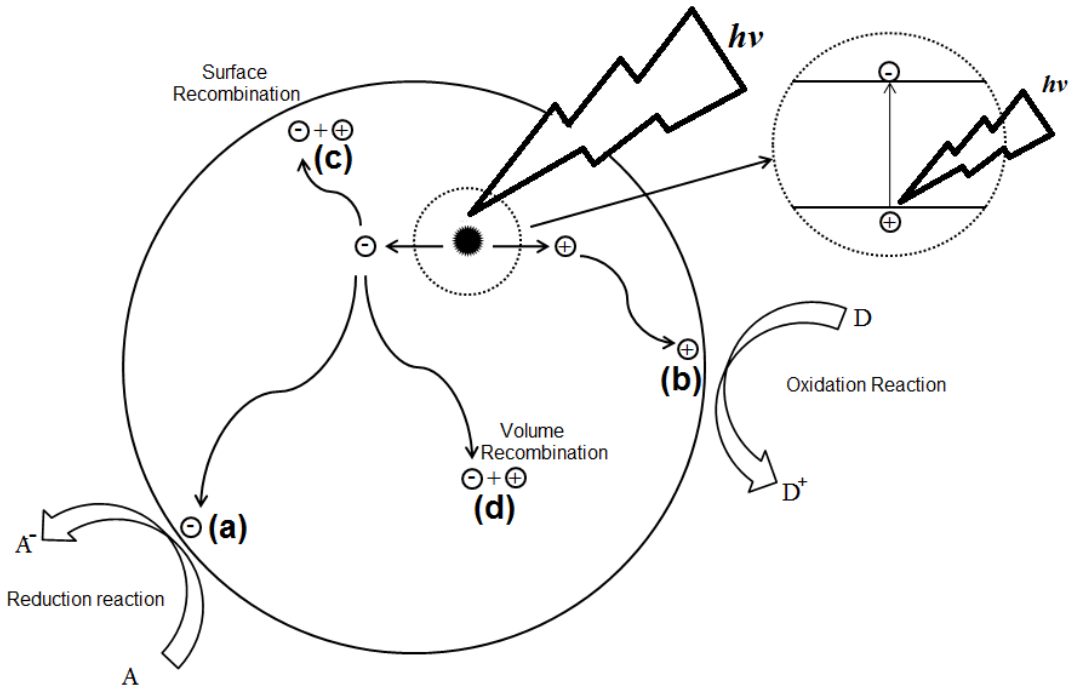

Figure.1.1 Schematic of photo-excitation and photogenerated electron and hole pathways over a semiconductor particle. (Adapted from Linsebigler et al., 1995) [3].

The semiconductors photocatalysis has been used for the decomposition of organic and inorganic contaminants such as “alkanes, aliphatic alcohols, aliphatic carboxylic acids, alkenes, phenols, aromatic carboxylic acids, dyes, PCB's, simple aromatics, halogenated alkanes and

alkenes, surfactants, and pesticides as well as for the reductive deposition of heavy metals (e.g., Pt^{4+}, Au^{3+}, Rh^{3+}, Cr(VI)) from aqueous solution to surfaces"[4].

Reaction for the heterogeneously photocatalyzed oxidation of a typical chlorinated hydrocarbon can be expressed as:

$$C_{\mathrm{x}}\mathrm{H_y\,Cl_z} + \left(\mathrm{x} + \frac{\mathrm{y+g}}{4}\right)\mathrm{O_2} \xrightarrow{h\nu \geq \mathrm{Eg}} \mathrm{xCO_2} + \mathrm{zH^+} + \mathrm{zCl^-} + \mathrm{H_2O}$$

Molecular oxygen adsorbed on the surface of the photocatalyst is activated by charge transfer of electrons generated from band gap excitation of semiconductor photocatalyst. The activated oxygen species are the primary agents and react with chlorinated hydrocarbon to produce CO_2, HCl and H_2O [5].

1.2. Mechanism of photocatalysis

1.2.1. Trapping of charge carrier

Charge carrier trapping is associated with trapping the photogenerated electron, hole or both. It reduces electron hole recombination and increases the life time of electron-hole separation for efficient photocatalytic activity in a semiconductor. During the preparation of colloidal and bulk semiconductor photocatalysts, surface and bulk irregularities *naturally* occur. The irregularities affect the surface electron states which differ in their energy from the bands present in the bulk semiconductor, and these electron states work as charge carrier traps and help to reduce the electron and hole recombination rate [3]

Another way of hole trapping can be achieved by using degradable adsorbates or a sacrificial reagent. Shiragami et al.[6] used triethylamine as sacrificial electron donors in CdS mediated photoreductions, functioning as hole traps, so that the conduction band electron can be transferred more slowly without significant electron hole recombination. In a similar manner, electron trapping is associated with adsorbed oxygen in inert solvent that has almost same energy level of reduction potential with conduction band of TiO_2 [7].

The charge trapping phenomenon has been observed on the surface of an irradiated CdS single crystal electrodes using photoreflectance spectroscopy [8]. The frequency of charge

tapping is dependent on the energy difference between the trap and the bottom of the conduction band (for electrons) or the top of the valence band (for holes), and the decrease in entropy [9].

1.2.2. Diffusion of charge carrier

The mobility of charge carrier in a semiconductor is also an important factor for photocatalysis. In TiO_2 particles, the photogenerated electrons are trapped at Ti^{4+} sites located on the surface, the relaxation into the trap is preceded by diffusion of conduction band electrons to the particle's surface [10]. The average diffusion time (τ_d) of charge carriers from the interior to the surface of colloidal semiconductor is given by:

$$\tau_d = r_0^2/\pi^2 D_{e^-}$$

where r is the particle radius and D_{e^-} is the diffusion coefficient of the carrier. The diffusion coefficient of conduction band electrons in TiO_2 ($D_{e^-} = 1.2t10^{-2}cm^2/s$) is relatively small owing to their heavy effective electron mass (m_{eff}=$30 \times m_e^{14}$) [11] .

The average transition time could be further reduced with presence of electric field in the semiconductor [10].Since the residence time for diffusion in colloidal particle is in the order of picoseconds and recombination time is nanoseconds, the diffusion of charge carriers from the interior to the particle surface can occur more rapidly than their recombination in TiO_2 [3]. A Schematic illustration of charge dynamic is shown Figure 1.2

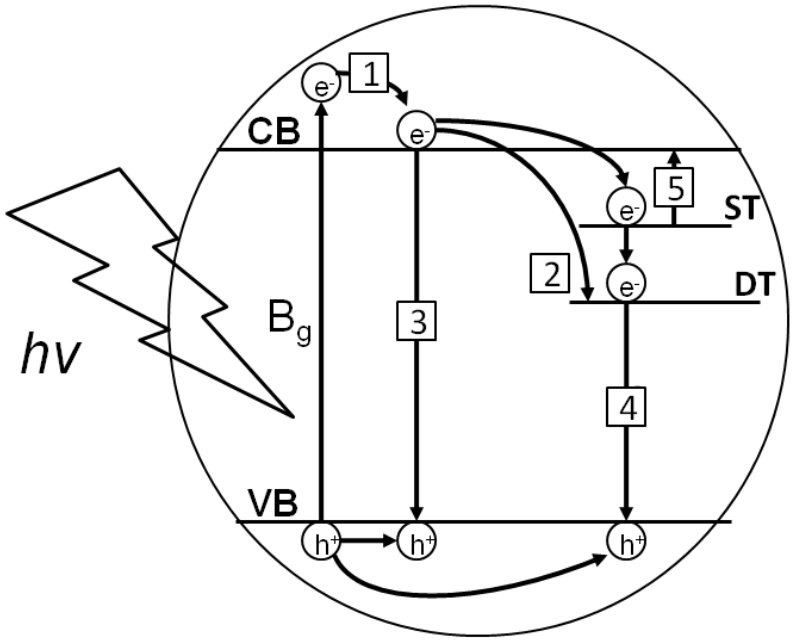

Figure 1.2 Schematic illustration of charge carrier dynamics in a semiconductor nanoparticle. (1) electrons quenched to the bottom of the conduction band, (2) charge carriers captured by shallow trap (ST) and deep trap (DT) states and further trapping from ST to DP, (3) band edge electron-hole recombination, (4) trapped electron-hole recombination, and (5) thermal excitation from traps. (Adapted from Rothenberger et al., 1985) [10].

1.2.3. Band- edge position

Another important fact for the photoinduced electron excitation is band gap edge position and the redox potentials of the adsorbates. The produced electrons and holes may induce redox reactions with adsorbates having suitable redox potential. From the thermodynamic point of view, the relevant potential level of the acceptor species is required to be lower (more negative) than the conduction band potential level of the photocatalyst whereas the potential level of the donor needs to be higher (more positive) than the valence band of the semiconductor in order to donate an electron to the vacant hole [3]. Figure 1.3 illustrate valence and conduction band position of various semiconductors. The energy scale is given versus normal hydrogen electrode (NHE) at pH=1.

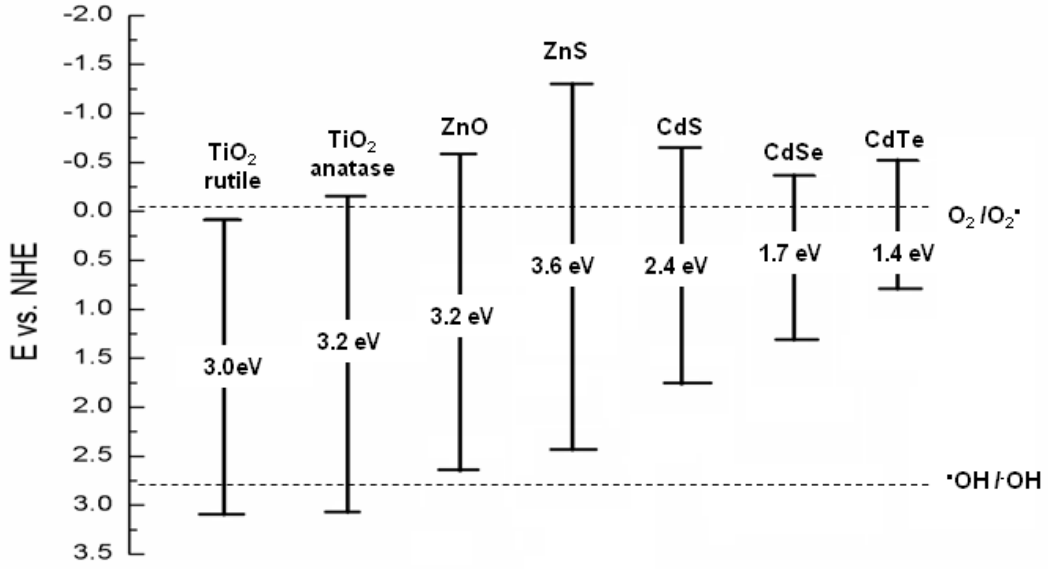

Figure 1.3 Valence and conduction band position for various semiconductors in aqueous electrolytes at pH=1. (Adapted from Langenhove et al., 2007) [12].

1.2.4. Space charge layers (Depletion layer)

At the contact between a solid semiconductor and another compound in a different physical state or of different type (e.g. liquid, gas, or metal), redistribution of electric charges generally occurs and the formation of a double charge layer. A space charge layer is generated when the mobile charge carriers transfer between the semiconductor and the contact phase, or the charge carrier trap at surface states of the interface. When TiO_2, an n-type semiconductor, contact with gas, it will form a surface state for electron trapping. The surface of TiO_2 becomes negative and a positive space charge layer will produce to preserve electrical neutrality just within the semiconductor [3]. This phenomenon changes the electrostatic potential and moves the bands' edge position upward towards the surface. Three kinds of space charge layers may result from the mobility of charge across for a n-type semiconductor, as presented in Figure 1.4.

When two different electrically neutral metal and semiconductor makes contact, electron migration occurs from the semiconductor to the metal until the two Fermi levels are aligned. The electron migration result in excess negative charge of metal surface while excess positive charge

of semiconductor and forms a space charge layer. This depletion layer formed between metal-semiconductor interfaces is called the Schottky barrier [3].

From the electrochemical point of view, it is crucial to know the effective length of space charge layer over which the charge separation occurs and the band bending. Since the effect of band bending may cause a shift in the position of the band edge of the semiconductor that introduce thermodynamic limitations for the onset of photo initiated reactions that can be carried out with charge carriers [13].

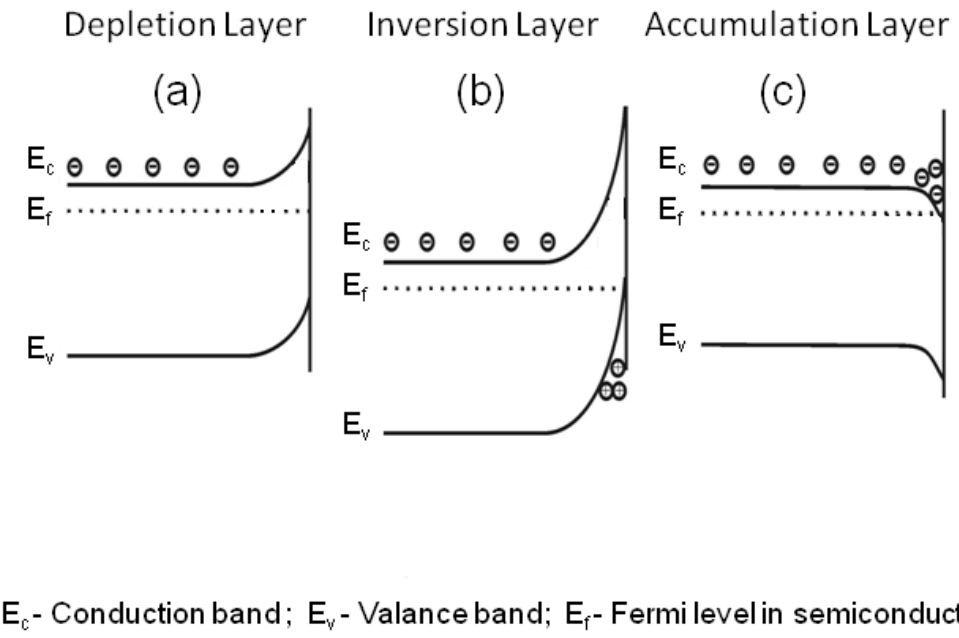

Figure 1.4 Types of charged layers in n-type semiconductors. a) Depletion layer. b) Inversion layer. c) Accumulation layer. (Adapted from Linsebigler et al., 1995) [3].

1.2.5. Quantum size effect (QSE)

The small clusters of atoms of semiconductor (Q-particles) on the order of 10-100Å, having ability of showing quantum size effect (QSE), is an important subject relevant to the electron excitation in photocatalyst [14]. The significant enhancement in photocatalytic reactivity may show when the semiconductor's particle size is comparable to the De Broglie wavelength of the charge carriers in the semiconductor. The Q-particle does not experience electronic

delocalization, instead, the photoinduced electrons and holes are confined in potential wells of a small geometric region. The confinement produces quantization of discrete electronic states and increases the effective band gap of the semiconductor. Such effects can change the color of the material and make a major increase on the band gap, which can reach up to 6 times that of the bulk band gap [3]. The increase in the effective band gap for CdS with decreasing particle size is illustrated in Figure 1.5.

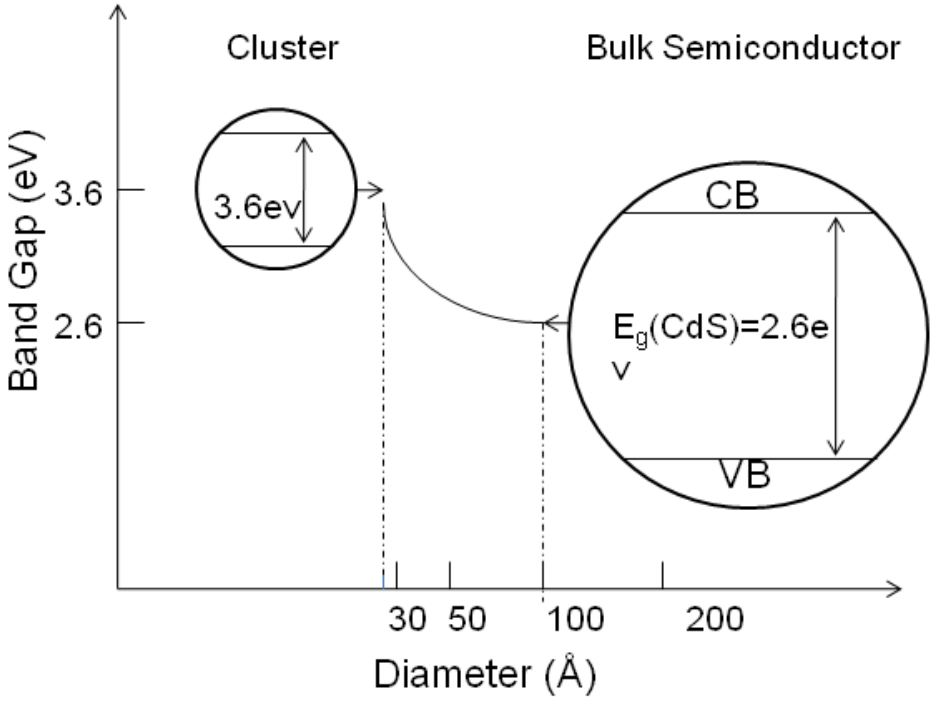

Figure 1.5 Quantum size effect on semiconductor band gap. (Adapted from Linsebigler et al., 1995)[3].

1.2.6. The photocatalytic efficiency

The efficiency of photocatalytic activity can be measured as quantum yield ($\emptyset$) which is defined as number of reactions from the absorption of one photon. However, the measurement of actual light absorption in heterogeneous system is difficult due to the light scattering. Therefore, it is usually assumed that all the light is absorbed and the efficiency is quoted as an apparent

quantum yield. If there are measurable products made during the activity, the efficiency can be express as the yield of products [3]. The quantum yield ($\emptyset$) is defined as follows:

$$\emptyset = \frac{dN_r/dt}{dN_{hv(inc)}/dt} \propto \frac{K_{CT}}{(K_{CT} + K_R)}$$

$\emptyset$ is the ratio between the rate of molecules formed or degraded in the system, dN_r/dt (molecules/s) and the rate of photons absorbed by the system, $dN_{hv(inc)}/dt$ (photons/s) at a given wavelength. Where K_{CT} is the rate of charge transfer and K_R is the electron-hole recombination rate. In ideal case, the quantum yield would be 1 with no recombination of electrons-holes and the rate of charge transfer would be dependent on the diffusion of charge carriers to the surface in the absence of excess surface charge. However, in real condition, recombination does occur and the concentration of electrons (n_s) and hole (p_s) at the surface of photocatalyst is not same in real system. As an example, the concentration of electrons and holes on TiO_2 during photo-oxidation process shows, $n_s > p_s$, owing to the electron process to molecular oxygen trapped at defect sites is relatively slow [3]. In addition, it is not necessary to all the incident photon will act upon the heterogeneous system and initiate the chemical transformation [16].

Therefore, an alternative for comparing efficiencies was introduced by defining relative photonic efficiency, ζ_r. A quantum yield can subsequently be determined from ζ_r, as $\emptyset = \zeta_r \emptyset_{phenol}$, where $\emptyset_{phenol}$ is quantum yield for photocatalyzed oxidation of phenol using Degussa P-25 TiO_2 as the standard catalyst with $\emptyset_{phenol} = 0.14 ol\ st$ at $\lambda = 365$ nm [17].

1.2.7. TiO_2 semiconductors for photocatalyst

Semiconductors are the most commonly used photocatalysts because of their relatively narrow gap (Eg<3.0 eV) whereas metals possess no band gap and insulator (Eg>3.0 eV) has wide gap. Metal oxides (e.g., TiO2, WO_3, ZnO, etc.) and chalcogenides (e.g., CDS, ZnS, CdSe, ZnSe and CdTe) are most commonly studied semiconductor photocatalysts [21]. Among the possible semiconductors, titanium dioxide (TiO_2) is the most extensively used due to its chemical stability, non-toxicity and relatively low cost. Rutile and anatase are commonly used TiO_2 crystal structure in photocatalysis application and it is known that anatase shows higher photocatalytic activity than that of rutile [19]. As previously illustrated (Figure 1.3), the VB redox potential of

both TiO_2 structures are more positive than that of the (·OH/-OH) redox couple, whereas only CB of anatase is at a more negative redox potential than that of $O_2/O_2^{\cdot}$ redox. It means adsorbed water and hydroxyl groups can be oxidized to highly reactive hydroxyl radicals on both TiO_2 structure, but oxygen molecules can be reduced to superoxide radical on anatase only, resulting more competitive than rutile for reduction reaction [11].

For bulk TiO_2, the rutile phase is considered more stable phase than the anatase phase at room temperature. However, Zhang et al. suggested and Gouma has confirmed independently that when the particle size is smaller than the critical size, *ca* 14nm, the total free energy of rutile is higher than anatase so anatase becomes more stable phase [20, 21]. Recent studies have shown that rutile and anatase mixture exhibit higher photocatalytic activity than of pure anatase. The high charge separation in anatase/rutile mixture is result of electron transfer from anatase CB to rutile CB [22, 23]. Now the anatase (70-80%)/rutile (20-30%) mixture, Degussa P25, is most widely used heterogeneous photocatalysis for environmental application [9].

The photocatalytic activity on TiO2 is following: Absorb light having higher energy than its band gap and produce negatively charged electron and positively charged hole pare. The produced holes then oxidize with water resulting in hydroxyl radicals which are powerful oxidizers that can easily oxidize organic contaminants. The electrons in conduction band react with water producing hydroxyl radicals [24]. The processes are summarized below.

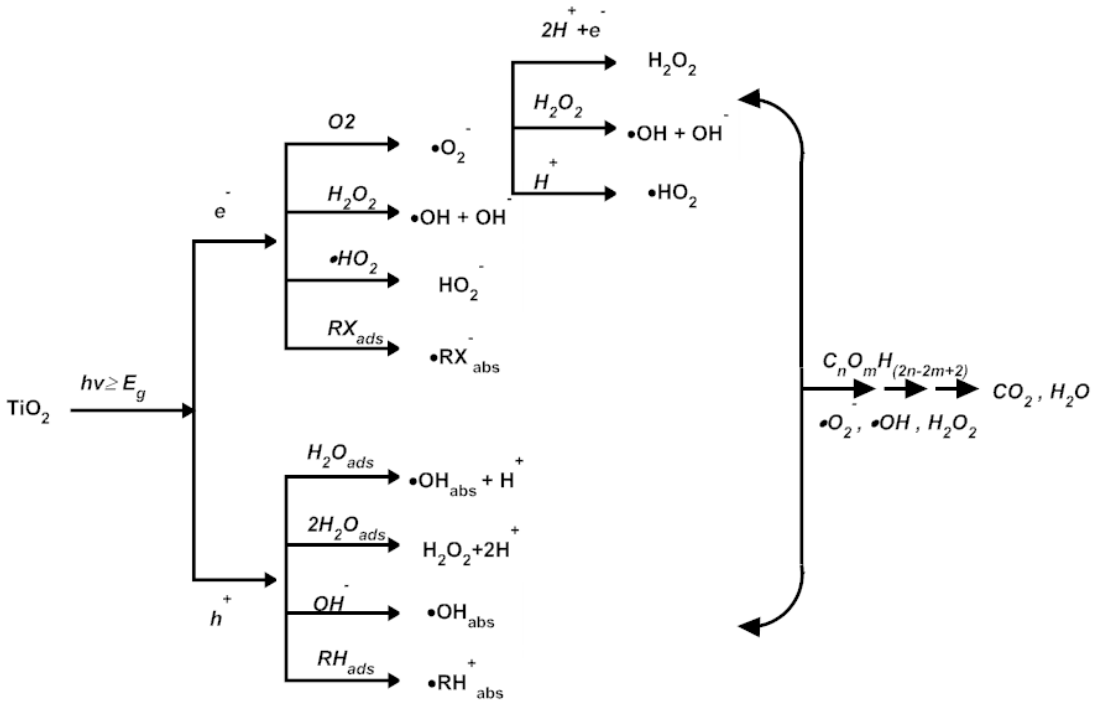

Figure 1.6 Chain of reactions involved in the production activated oxygen species in the photoelectrochemical mechanism. (Adapted from Langenhove et al., 2007) [12].

In the presence of absorbed water and oxygen couple (H_2O/O_2), absorbed water gets oxidized splitting into ·OH and H^+ and absorbed organic pollutants (RH) can be directly oxidized producing cationic radicals $RH^{\cdot +}$ by holes in VB. Absorbed oxygen gets reduced by the electron results in generation of superoxide radical anions ($\cdot O_2^-$), which in turn reacts with H^+ to generate hydrogen dioxide radical ($\cdot HO_2$) in CB. On subsequent reaction with an electron and a hydrogen ion, a molecule of H_2O_2 is eventually produced. Electron also can directly react with adsorbed halogenated organic pollutant (RX) generating anionic radicals ($\cdot RX^-$). These chain reaction result in reactive oxygen species (ROS) such as H_2O_2, O_2- and hydroxyl radical ·OH [20].

It is generally considered that photocatalytic reduction of organic compounds is less important than the oxidation, since the reduction potential of a TiO_2(e-) is lower than the oxidation potentials of a TiO_2(h+). In addition, O_2 shows much higher kinetics as an electron scavenges than most of the reducible substrates [9].

1.2.8. Modification of photocatalyst

In order to determine the right purpose of particular semiconductor photocatalysis system need to consider several factors such as the efficiency of photocatalytic process, stability under light, the selectivity of the product and activation range of wavelength [3]. For example, TiO_2, most extensively studied semiconductor photocatalysis, has strong photostability. However, it only absorb UV light (absorption band at 390-400nm) which is only about 3% of overall solar spectrum [25]. The limitation of certain semiconductors and necessity of optimum efficiency to meet specific application has increased research interest on new materials and the modification of materials. In order to enhance the photocatalytic efficiency, three main aspects should be considered. First, increase of the charge separation and recombination lifetimes of charge carriers. Second, increase of the solar spectrum response range. Third, change the selectivity or yield of a particular product [3].

One way to increasing charge separation and extending the solar spectrum response range is coupling semiconductors. The study of CdS-TiO_2 photocatalyst shows that a photon with wavelength less than 495nm excite an electron from the valance band across the band gap of CdS (E_g=2.5eV) then those photogenerated electrons transfer to the TiO_2 conduction band [26]. The photogenerated holes in the conduction band of CdS particle migrate to the surface and participate in the oxidation of adsorbed organics. The electrons that are transferred to the conduction band of TiO_2 participate in reduction reactions increasing charge separation and photocatalytic efficiency. Figure 1.7 is the illustration of the CdS-TiO_2 coupled semiconductor photocatalyst.

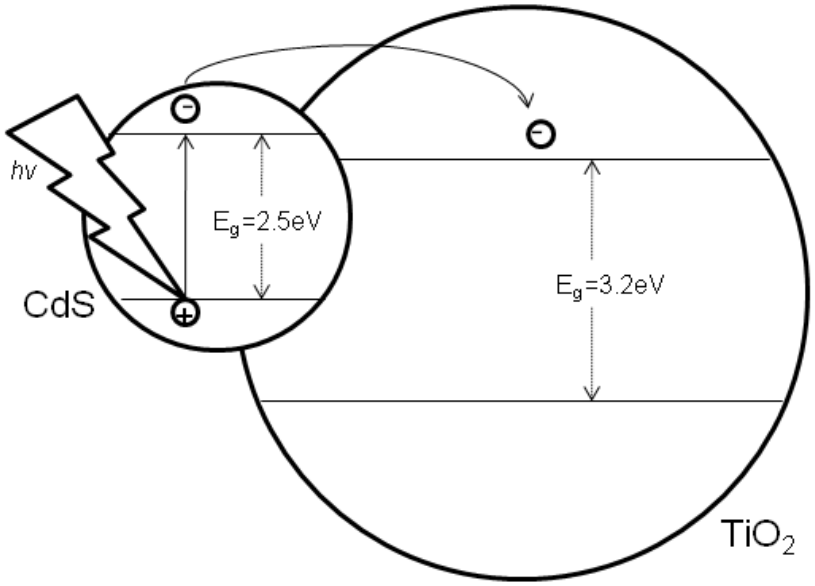

Figure 1.7 Photo-excitation in composite semiconductor-semiconductor photocatalyst. (Adapted from Gaya & Abdullah, 2008) [27].

The recent studies of nonmetal doping on TiO_2, such as carbon [28], nitrogen [29, 30, 31] sulfur [32], phosphate [29, 33] shows that significant improvement utilizing visible spectrum. These anion dopants substitute the oxygen lattice on TiO_2 and lead to a band gap narrowing resulting in high visible absorption [29]. Many doping processes employ a simple sol-gel method adding acid doping source in the precursor [28, 29, 31, and 33]. Moreover, co-doping of double nonmetal elements, such as N-F [34], C-N [35] and S-N [36], also shows high activity towards visible light.

Surface sensitization of wide band gap semiconductor photocatalyst (TiO_2) using common dyes, such as erythrosine B [37], thionine [38], tris ruthenium(II)(RuL_3^{4-}) [39] ,etc., can increase photo-excitation efficiency. If the oxidative energy level of excited state of dye molecule is more negative than conduction band energy of semiconductor, the dye molecule can transfer the electrons to the conduction band of the semiconductor. The transferred electrons are trapped on

surface of semiconductor then react with adsorbed contaminants on the surface of semiconductor.

Addition of noble metal to semiconductor particles is another example to lowering the electron-hole recombination rate. In Pt-TiO_2 metal- semiconductor system, Pt acts as a trapping site of excited electrons which generated from TiO_2 particle. This electron migration effect was confirmed by the reduction in the photoconductance of semiconductor. The photoinduced holes then freely diffuse to semiconductor surface to oxidize adsorbed contaminants. As seen in space charge layers section (3.4), the metal changes the electron distribution which results in decrease in electron density within the semiconductor leading to increase of the hydroxyl group acidity [40]. The addition of Pt on TiO_2 also increases gas evolving, especially hydrogen, which attribute the trapping of electron at the metal site [3]. The study of optimum Pt loading content shows that the loading of 0.6 wt% effect higher photocatalytic activity for H2 evolution to achieve a maximum photocatalytic rate [41].

The relation between photocatalytic property and morphology including shape, size and surface area of particles is important aspect. TiO_2, particularly, shows different photocatalytic activity toward the same substrate in a liquid or a gas phase [42]. The advantage of using nanostructured semiconductor is flowing: (1) high absorption cross section (2) fast carrier diffusion on the interface that, in principle, can reduce recombination, (3) high surface area-to-volume ratios, and (4) blue shift in the light absorption [25]. For example, the relation between the particle size and high reactive and selective of catalysts for the photocatalytic oxidation of organic compounds for nanostructure TiO_2 has been studied. Reaction studies conducted using gas-phase photo-oxidation of toluene as a probe reaction shows that the activity and selectivity of the TiO_2 catalyst were sensitive to the particle size. Higher conversions for toluene photo-oxidation were obtained by decreasing the TiO_2 particle size [43].

From the above it is inferred that there are many factors controlling the photocatalytic activity of a semiconductor and it is difficult to determine s individual contributions. Below, the effect of sol-gel processing on oxide photocatalysts is reviewed, as reported in the literature, focusing on highlighting trends to achieve optimum performance.

1.3. Sol-gel synthesis of metal oxide photocatalysts

The sol-gel technique is a soft chemistry process used to produce metal oxide nanomaterials (see Figure 1.8) It has received a lot of attention due to the high chemical homogeneity achieved, low processing temperature required, and the possibility of controlling the various structural and morphological features of the synthesized product, such as the surface morphology, the surface area, particle size and crystallinity, and the phase of the material [44]. The typical sol-gel process for metaloxides involves the hydrolysis and condensation of metal alkoxides (M(OR)n) as starting/precursor materials. The reaction process proceeds as follows:

1. Hydrolysis

   $M(OR)_n + H_2O \rightarrow M(OR)_{n-1}(OH) + ROH$

2. Condensation

   Dehydration

   $M(OR)_n + M(OR)_{n-1}(OH) \rightarrow M_2O(OR)_{2n-2} + ROH$

   Dealcoholation

   $2M(OR)_{n-1}(OH) \rightarrow M_2O(OR)_{2n-2} + H_2O$

   The net reaction is

   $M(OR)_n + \frac{\mathbf{n}}{\mathbf{2}}H_2O \rightarrow M(OR)_{n/2} + nROH$

Metal alkoxides are hydrolyzed and poly-condensed to form a metal oxide gel, whereas M= Si, Ti, Zr, Al, etc., and R= alkyl group.

The alkoxide groups are removed by acid or base catalyzed hydrolysis reactions and hydroxyl groups. Subsequent condensation and reactions involving the hydroxyl groups yield networks composed of oxo(M-O-M) linkages. Low volume fraction particles in colloidal solution may go through sedimentation or centrifugation methods to obtain gel-like properties. The remaining solvent can be removed by a drying process that causes shrinkage and densification. The solvent removal rate affects the porosity distribution in the gel. For further

poly-condensation and enhancing the structural stability, a subsequent thermal treatment is necessary to acquire the final product. Even a small amount of dopants, such as organic dyes or rare earth metals, can be introduced in the sol and obtain uniformly dispersed in the final product [45].

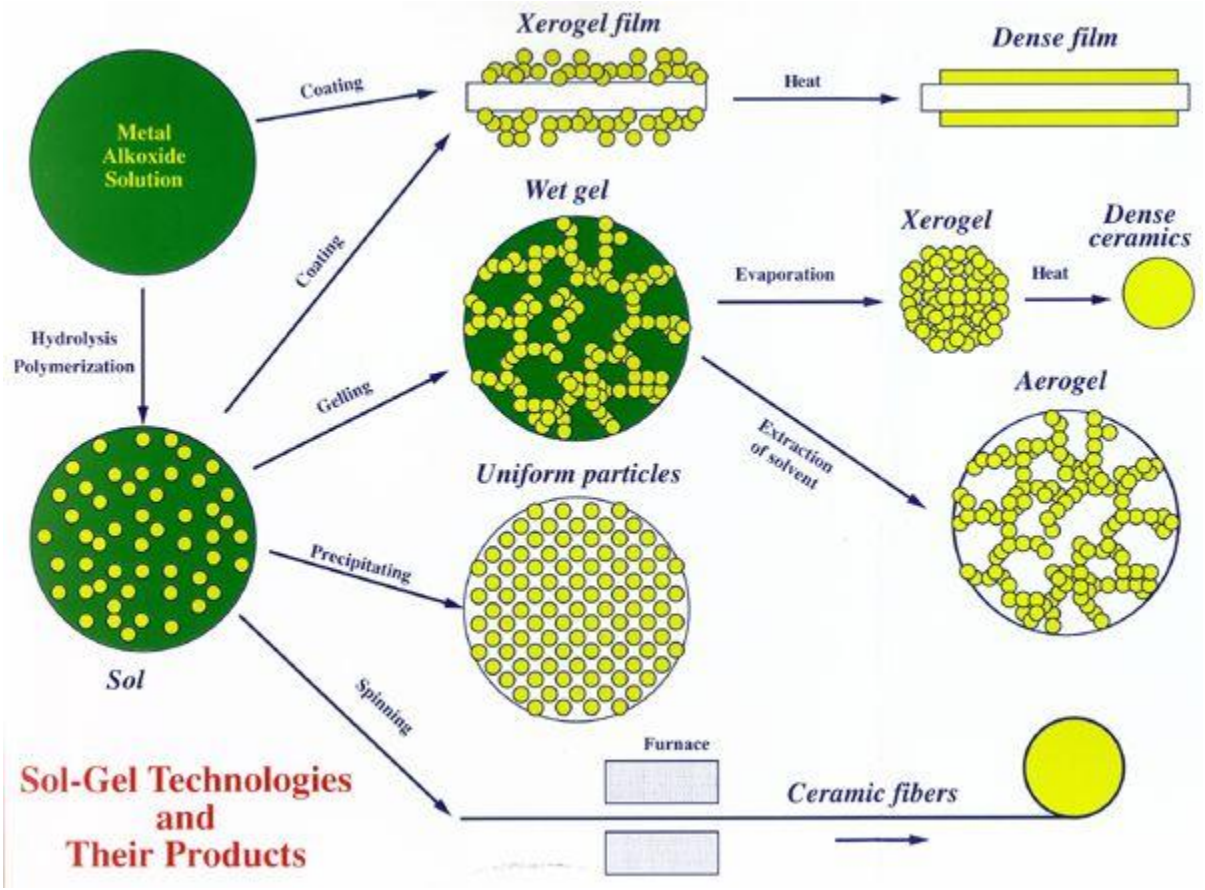

Figure 1.8 Schematic of the Sol-Gel processing (www.chemat.com).

1.3.1. Factors affecting sol-gel process for photocatalyst

pH

The different pH levels in sol-gel process strongly influences particle size and phase composition of final products. Solid oxides in aqueous suspension tend to have electrical charge due to the amphoteric dissociation of surface hydroxyl groups, the adsorption of H^+/OH^- ions, or

metal hydroxo compounds from the hydrolysis of solid material [20]. Bahnemann et al. [51] reported that the surface acidic/basic properties of TiO_2 can be determined by chemisorption of

H^+ ($TiO_2 + nH^+$ iObe dH_n^{n+} , for pH < 3.5)

or

OH^- ($TiO_2 + nOH^- \leftrightarrow TiO_2(OH)_n^{nO}$, for pH > 3.5)

Since the resultant surface charge is pH dependent, the strong repulsive force among charged particles reduces the probability of coalescence and thus more stable sols can be formed in acidic or alkaline media [20]. Wu et al. also suggested that since the isoelectric point of TiO_2 is 6.7, surface modification of colloids could be done by adding inorganic acid which results in preventing aggregation and the formation of a homogeneous colloidal solution [46].

Studies on the oxide crystallinity following sol-gel hydrolysis in different pH levels revealed that the anatase phase content in the products increases with increasing Ph [47]. It was also shown that brookite was produced only in a certain range of acidity and disappeared prior to anatase onset with increasing acidity; and in high acid concentration it was favored compared to rutile crystallization. The study of hydrothermally processed product (Ti^{4+} concentration 0.44 mol dm^{-3}) showed mainly anatase and it contained some brookite and some rutile at pH = 1.0. The rutile phase disappeared in pH=3.4, and pure anatase phase with a granular morphology was obtained in pH=7.1. When the pH >8, an amorphous phase began to appear [47].

Particle growth during hydrothermal aging in different pH values typically follows coarsening and aggregation. Isley and Penn [48] have studied hydrothermal aging with increasing pH in the range of -0.5 to 3. The synthesized TiO_2 showed that a sol-gel pH of -0.5 results in particle coarsening, and sol-gel pH of 3 result in particle growth involving both oriented aggregation and coarsening. The smaller particle size is expected to lead to higher TiO_2 solubility, which is consistent with the increase in the growth rate by coarsening; and the greater surface charge is expected to lead to higher electrostatic repulsions between particles, which is consistent with the decrease in the rate of growth by oriented aggregation [48]. The test results

indicate that the products of hydrothermal aging are influenced by pH since initial phase composition and average particle size are also dependent on the sol-gel's pH.

Additives

It has been reported that additives (or mineralizers) can affect the morphology, phase, particle size and photocatalytic activity of TiO_2 particles [46, 47]. Cheng et al. [47] examined the effects of three mineralizers, NH_4C1, NaC1, and $SnC1_4$, on the titanium dioxide formed in hydrothermal reactions with constant total Cl- concentration. The results showed that all three mineralizers ($SnC1_4$, NaC1 and NH_4C1) are favoring the formation of rutile phase and are decreasing grain size, but NH_4C1 promotes agglomeration among grains. It was considered that the additives could adsorbed on TiO_2 particles and act as an nuclear agents changing the surface state to prevent particle growth and phase change from anatase to rutile As the concentration of NaCl was increased, the size of rutile particle was reduced and rutile formations were promoted [46]. It was found that NaCl serves a dual rule: as a chemical catalyst and as a means of physical confinement. NaCl can favor to rutile formation and crystal growth and it may serve as an electrolyte promoting electrostatic adsorption at high concentrations.

Al-Salim et al. [49] found that alkaline earth ion (20 mol%) additives not only affect the TiO_2 formation but also approximately double the photocatalytic activity of Degussa P-25 without additive. The increasing concentration of alkaline earth ion additives resulted in the inhibition of anatase crystallization (Ba > Sr > Ca) and increase of surface areas with constant porosity. They also suggested that the high photodecomposition rate of aqueous oxalic acid on TiO_2 with alkaline earth additives might be due to an increase in the surface area of the TiO_2 crystallites.

Reaction Temperatures and Time

Reaction temperature and time have important role of thermodynamic and kinetic factors for hydrothermal reaction [46]. It is known that increasing reaction temperature may cause aggregation and/or phase and structure change of product, whereas lowering reaction temperature may decrease grain size and/or agglomeration among particles [50, 51].

Wu et al.[46] showed that 0.5M of Titanium n-butooxide(TNB) and HCl mixture at 100℃ initially showed mainly anatase with trace of rutile and brookite. Overall increase of reaction temperature and time accelerate the phase transformation from anatase (metastable) to rutile(stable) phase and condenser phase formation. Increasing reaction temperature caused the gradual disappearance of brookite and anatase phases and eventually led to the formation of a pure rutile phase and by prolonging the reaction time, an increased average grain size.

Cheng et al. [51] suggested that increase of reaction temperature generated a large amount of Cl^- coming from hydrolysis of $[Ti(OH)_nCl_m]^{2-}$ complex ions and gradually substituted OH^- ligands, while the linking between $[TiO_6]$ was carried out by the dehydration in $[Ti(OH)_nCl_m]^{2-}$. The produced TiO_2 crystallite formed an aggregate easily due to its large surface area.

H_2O/ alkoxide molar ratio

The Ti/alkoxide molar ratio is an important parameter which has an impact on both the titania product mixture and the average particle sizes during hydrolysis reaction of sol-gel. Isley et al. found that decreasing the Ti/H_2O molar ratio (from 1:4 to 1:700) resulted in both decreasing brookite content and anatase particle size in sol-gel synthesized TiO_2 nanocrystallines [52]. Wang et al. also showed effect of water: titania ration during the sol-gel synthesis at 450℃ and it was note that increasing water: alkoxide ratio led to reduced crystal size. As seen in hydrolysis equation above, high water: alkoxide ratios the generally promote hydrolysis, f1avoring nucleation versus particle growth [53]. Li et al. pointed out that as water concentration increase the gelation time is significantly reduced during the hydrolysis and polycondensation reaction of $Ti(O\text{-}Bu)_4$. [54]. In high water concentration, macromolecular networks form rapidly through the reactions of hydrolysis and condensation, and have low interconnectivity. Whereas, in low water concentration, networks form slowly, leading to a denser structured.

References

[1] Xu, Y., and Schoonen, M.A.A. The absolute energy positions of conduction and valence band of selected semiconducting minerals, *Am. Mineral*. 85, 543–556, 2000.

[2] Dvoranov, D. (2002). Investigations of metal-doped titanium dioxide photocatalysts. *Applied Catalysis B: Environmental*, *37*(2), 91-105. doi: 10.1016/S0926-3373(01)00335-6.

[3] A. Linsebigler, G. Lu, and J. Yates, J, Chem. Rev. 1995, 95, 735-758.

[4] Hoffmann, M. R., Martin, S. T., Choi, W., & Bahnemann, D. W. (1995). Environmental Applications of Semiconductor Photocatalysis. *Chemical Reviews*, *95*(1), 69-96. doi: 10.1021/cr00033a004.

[5] Hoffmann, M. R., Martin, S. T., Choi, W., & Bahnemann, D. W. (1995). Environmental Applications of Semiconductor Photocatalysis. *Chemical Reviews*, *95*(1), 69-96. doi: 10.1021/cr00033a004.

[6] Shiragami, T., Pac, C., & Yanagida, S. (1989). Nonmetallised CdS-catalysed Photoreduction of Aromatic Ketones to Alcohols and / or. *Photochemistry*, 0-1.

[7] Fox, M. A., & Chen, C. C. (1981). Mechanistic features of the semiconductor photocatalyzed olefin-to-carbonyl oxidative cleavage. *Journal of the American Chemical Society*, *103*(22), 6757-6759. doi: 10.1021/ja00412a044.

[8] Nakabayashi, S., & Kim, A. (1991). Surface-Trapped Charge at CdS Electrode in Aqueous Solution As Observed by Photoreflectance Spectroscopy, (16), 9961-9965.

[9] Fox, M. A. and M. T. Dulay (1993). "Heterogeneous photocatalysis." Chemical Reviews 93(1): 341-357.

[10] Rothenberger, G., J. Moser, et al. (1985). "Charge carrier trapping and recombination dynamics in small semiconductor particles." Journal of the American Chemical Society 107(26): 8054-8059.

[11] *Gratzel, M.*; *Frank, A. J.* J. *Phys. Chem. 1982, 86, 2964.*

[12] Langenhove, K. D. J. D. H. V. and (2007). "Heterogeneous Photocatalysis as an Advanced Oxidation Process for the Abatement of Chlorinated, Monocyclic Aromatic and Sulfurous Volatile Organic Compounds in Air: State of the Art." Critical Reviews in Environmental Science and Technology 37(6): 489 - 538.

[13] Vinodgopal, K., S. Hotchandani, et al. (1993). "Electrochemically assisted photocatalysis: titania particulate film electrodes for photocatalytic degradation of 4-chlorophenol." The Journal of Physical Chemistry 97(35): 9040-9044.

[14] Alivisatos, P., Semiconductor clusters, nanocrystals, and quantum dots, Science, 1996, 271: 933937

[15] D. F. Ollis and H. Al.-Ekabi, *Photocatalytic Purification and Treatment of Water and Air*, Elsevier, Amsterdam, The Netharlands, 1993.

[16] Serpone, N., & Emeline, a V. (2005). Modelling heterogeneous photocatalysis by metal-oxide nanostructured semiconductor and insulator materials: factors that affect the activity and selectivity of photocatalysts. *Research on Chemical Intermediates*, *31*(4), 391-432. doi: 10.1163/1568567053956789.

[17] Serpone, N. (1997). Relative photonic efficiencies and quantum yields in heterogeneous photocatalysis. *Journal of Photochemistry and Photobiology A: Chemistry*, *104*(1-3), 1-12. doi: 10.1016/S1010-6030(96)04538-8.

[18] Prousek, J. Advanced oxidation processes for water treatment. Photochemical processes, *Chem. Listy* 90, 307–315, 1996.

[19] Augustynski, J. (1993). "The role of the surface intermediates in the photoelectrochemical behaviour of anatase and rutile TiO2." Electrochimica Acta 38(1): 43-46.

[20] Zhang, H., & Banfield, J. F. (1998). Thermodynamic analysis of phase stability of nanocrystalline titania. *Journal of Materials Chemistry*, *8*(9), 2073-2076. doi: 10.1039/a802619j.

[21] Gouma, P. I. (2003). NANOSTRUCTURED POLYMORPHIC OXIDES FOR ADVANCED CHEMOSENSORS, *5*, 147-154.

[22] Hurum, D. C., A. G. Agrios, et al. (2003). "Explaining the Enhanced Photocatalytic Activity of Degussa P25 Mixed-Phase TiO2 Using EPR." The Journal of Physical Chemistry B 107(19): 4545-4549.

[23] *Wang, R.*, Hashimato, K., Fujishima, A. *et al.*, *Light induced amphiphilic surface*,*Nature*, *1997*, *388*: *431*—432

[24] A. Mills and S. L. Hunte, J of Photochemistry and Photobiology A: Chemistry 108 (1997) 1-3.

[25] Hashimoto, K. I., Hiroshi; Fujishima, Akira (2005). "TiO2 Photocatalysis: A Historical Overview and Future Prospects." Japanese Journal of Applied Physics 44(12): 8269

[26] Gopidas, K. R., M. Bohorquez, et al. (1990). "Photophysical and photochemical aspects of coupled semiconductors: charge-transfer processes in colloidal cadmium sulfide-titania and cadmium sulfide-silver(I) iodide systems." The Journal of Physical Chemistry 94(16): 6435-6440.

[27] Gaya, U., & Abdullah, a. (2008). Heterogeneous photocatalytic degradation of organic contaminants over titanium dioxide: A review of fundamentals, progress and problems. *Journal of Photochemistry and Photobiology C: Photochemistry Reviews*, *9*(1), 1-12. doi: 10.1016/j.jphotochemrev.2007.12.003.

[28] Sakthivel, S., & Kisch, H. (2003). Daylight photocatalysis by carbon-modified titanium dioxide. *Angewandte Chemie (International ed. in English)*, *42*(40), 4908-11. doi: 10.1002/anie.200351577.

[29] Asahi, R.; Morikawa, T.; Ohwaki, T.; Aoki, K.; Taga, Y. Visible-Light Photocatalysis in Nitrogen-Doped Titanium Oxides. Science 2001, 293, 269–271.

[30] Hou, Y. D., Wang, X. C., Wu, L., Chen, X. F., Ding, Z. X., Wang, X. X., et al. (2008). N-doped SiO2/TiO2 mesoporous nanoparticles with enhanced photocatalytic activity under visible-light irradiation. *Chemosphere*, *72*(3), 414-21. doi: 10.1016/j.chemosphere.2008.02.035.

[31] Yokosuka, Y.; Oki, K.; Nishikiori, H.; Tatsumi, Y.; Tanaka, N.; Fujii, T. Photocatalytic degradation of trichloroethylene using N-doped TiO2 prepared by a simple sol-gel process. Res. Chem. Intermediat. 2009, 35, 43–53.

[32] Umebayashi, T., Yamaki, T., Itoh, H., & Asai, K. (2002). Band gap narrowing of titanium dioxide by sulfur doping. *Applied Physics Letters*, *81*(3), 454. doi: 10.1063/1.1493647.

[33] Lin, L.; Lin, W.; Xie, J.L.; Zhu, Y.X.; Zhao, B.Y.; Xie, Y.C. Photocatalytic properties of phosphor-doped titania nanoparticles. Appl. Catal. B 2007, 75, 52-58.

[34] Huang, D.-G., Liao, S.-J., Liu, J.-M., Dang, Z., & Petrik, L. (2006, December 15). Preparation of visible-light responsive N–F-codoped TiO2 photocatalyst by a sol–gel-

solvothermal method. *Journal of Photochemistry and Photobiology A: Chemistry*. doi: 10.1016/j.jphotochem.2006.04.041.

[35] Li, Q., Xie, R., Li, Y. W., Mintz, E. a, & Shang, J. K. (2007). Enhanced visible-light-induced photocatalytic disinfection of E. coli by carbon-sensitized nitrogen-doped titanium oxide. *Environmental science & technology*, *41*(14), 5050-6. Retrieved from http://www.ncbi.nlm.nih.gov/pubmed/17711222.

[36] Naik, B., Parida, K. M., & Gopinath, C. S. (2010). Facile Synthesis of N- and S-Incorporated Nanocrystalline TiO 2 and Direct Solar-Light-Driven Photocatalytic Activity. *Society*, 19473-19482.

[37] Kamat, P. V.; Fox, M. A. *Chem. Phys. Lett.* 1983, 102, 379.

[38] Patrick, B.; Kamat, P. V. *J. Phys. Chem.* 1992,96, 1423.

[39] Vlachopoulos, N.; Liska, P. Augustynski, J.; Gratzel, M. *J. Am. Chem.* SOC. 1988, 110, 1216.

[40] Jafiezic-Renault, N.; Pichat, P.; Foissy, A,; Mercier, R. *J. Phys. Chem.* 1986, 90, 2733.

[41] Sreethawong, T., & Yoshikawa, S. (2006, May). Enhanced photocatalytic hydrogen evolution over Pt supported on mesoporous TiO2TiO2 prepared by single-step sol–gel process with surfactant template. *International Journal of Hydrogen Energy*. doi: 10.1016/j.ijhydene.2005.06.015.

[42] Maldotti, A., A. Molinari, et al. (2003). "Photocatalysis with Organized Systems for the Oxofunctionalization of Hydrocarbons by O2." ChemInform 34(4): no-no.

[43] Maira, A. J., K. L. Yeung, et al. (2001). "Gas-phase photo-oxidation of toluene using nanometer-size TiO2 catalysts." Applied Catalysis B: Environmental 29(4): 327-336.

[44] Baiju, K. V.; Sibu, C. P.; Rajesh, K.; Mukundan, P.; Warrier, K. G. K.; Wunderlich, L. *Mater Chem. Phys.* 2005, *90*, 123.

[45] Klein, L. C. (1993). Sol-Gel Optical Materials. *Annual Review of Materials Science*, *23*(1), 437-452. doi: 10.1146/annurev.ms.23.080193.002253.

[46] Wu, M., G. Lin, et al. (2002). "Sol-Hydrothermal Synthesis and Hydrothermally Structural Evolution of Nanocrystal Titanium Dioxide." Chemistry of Materials 14(5): 1974-1980.

[47] Cheng, H., Ma, J., Zhao, Z., & Qi, L. (1995). Hydrothermal Preparation of Uniform Nanosize Rutile and Anatase Particles. *Chemistry of Materials*, *7*(4), 663-671. doi: 10.1021/cm00052a010.

[48] Isley, S. L., & Penn, R. L. (2008). Titanium Dioxide Nanoparticles : Effect of Sol-Gel pH on Phase Composition , Particle Size , and Particle Growth Mechanism. *Society*, 4469-4474.

[49] Al-Salim, N. I., Bagshaw, S. a, Bittar, A., Kemmitt, T., James McQuillan, a, Mills, A. M., et al. (2000). Characterisation and activity of sol–gel-prepared TiO2 photocatalysts modified with Ca, Sr or Ba ion additives. *Journal of Materials Chemistry*, *10*(10), 2358-2363. doi: 10.1039/b004384m.

[50] Su, C., B. Y. Hong, et al. (2004). "Sol-gel preparation and photocatalysis of titanium dioxide." Catalysis Today 96(3): 119-126.

[51] Cheng, H., Ma, J., Zhao, Z., & Qi, L. (1995). Hydrothermal Preparation of Uniform Nanosize Rutile and Anatase Particles. *Chemistry of Materials*, *7*(4), 663-671. doi: 10.1021/cm00052a010.

[52] Isley, S. L., & Penn, R. L. (2008). Titanium Dioxide Nanoparticles : Effect of Sol-Gel pH on Phase Composition , Particle Size , and Particle Growth Mechanism. *Society*, 4469-4474.

[53] Wang, C.-C. and J. Y. Ying (1999). "Sol−Gel Synthesis and Hydrothermal Processing of Anatase and Rutile Titania Nanocrystals." Chemistry of Materials 11(11): 3113-3120.

[54] Li, Y., White, Ã. T. J., & Lim, S. H. (2004). Low-temperature synthesis and microstructural control of titania nano-particles. *Journal of Solid State Chemistry*, *177*, 1372-1381. doi: 10.1016/j.jssc.2003.11.016.

Chapter 2 Novel Materials Synthesis and Fabrication and Characterization methods

2.1. Electrospinning

Electrospinning is the process used for producing micro to nano scale fibers from polymer precursor. The fibers obtained from electrospinning are extremely fine which have large surface area to volume ratio. Electrospinning is extensive studied by Zeleny [1] on the behavior of droplet at Taylor cone in 1914 and patented by Formhals et. al. in 1934. Electrospinning was harnessed as the primary nanofabrication route for polymer fibers. The electrospinning process operates on the principle that material is extracted under the action of an electric field from a polymer solution bath. At a critical intensity of the electric field, a jet forms and flies toward the opposite electrode. During this flight, the jet thins and undergoes a series of hydrodynamic instabilities that lead to jet braking and splitting. Solvent evaporation leads to the deposition of polymer fibers of nanometer scale diameter as non woven mats. The advantages of utilizing electrospinning for the formation of nanostructured composite mats include the room temperature processing, no special requirements for the processing environment (air vs. controlled atmospheres), and wide range of appropriate precursor materials (polymers or biologicals) – such as proteins, tissue, etc. leading to many different applications. A typical electrospinning set-up consists of a high voltage power supply, a programmable syringe pump, syringe, needle, and a grounded collector screen as illustrated in Figure 2.1.

Electrospinning now finds several applications such as automobile industry for purpose like air filter, medical industry, tissue engineering, composite, electronics and many more industrials and research fields[2].

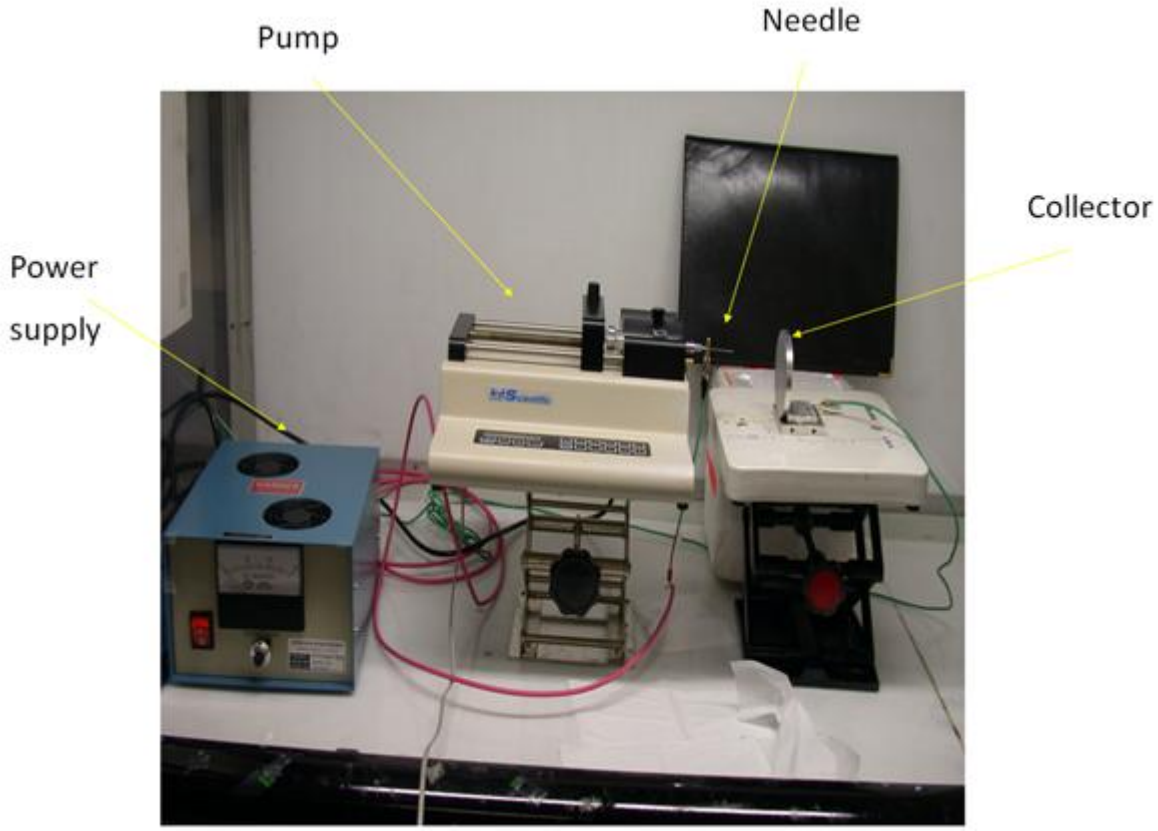

Figure 2.1 Image of conventional electrospinning setup.

There are numbers of parameters affect the characteristics of the electrospun fibers formed. Those parameters can be divided into mainly two groups a) solution parameters and B) process parameters [3]. The affect of the each of these parameters on the structure and properties of the materials obtained are discussed below:

2.1.1. Solution Parameters

a. Concentration- Generally, as increasing the concentration of the solution, the fiber diameters will be increased. However, if the solution's concentration is too low, micro (nano) polymeric beads will be obtained. If the concentration is too high, helix-shaped micro belts or ribbon will be formed.

b. Molecular Weight- In principle, molecular weight represents the entanglement of the polymer chain in solution. Therefore, higher molecular weight polymers are usually used since

they assist in uniform fiber formation and provide sufficient viscosity. However, too high molecular weight polymer favors the formation of the micro belts or ribbon.

c. Viscosity- Finding optimized viscosity is very important to determine the electrospun fibers morphology. With too low viscosity precursor there is no continuous fiber formation whereas with too high viscosity precursor ejection of fibers become difficult

d. Surface Tension- surface tension is related to the composition of the solution[3]. Generally, too high surface tension hamper the process due the instable jet and high chance of droplet formation.

e. Conductivity/Surface Charge Density- Conductivity of precursor is usually determined by the solvent type, polymer class, and the availability of ionizable salts. Therefore adding salt may be used to eliminate beads forming during the electrospinning. Generally, increasing conductivity favors the formation of thinner fibers.

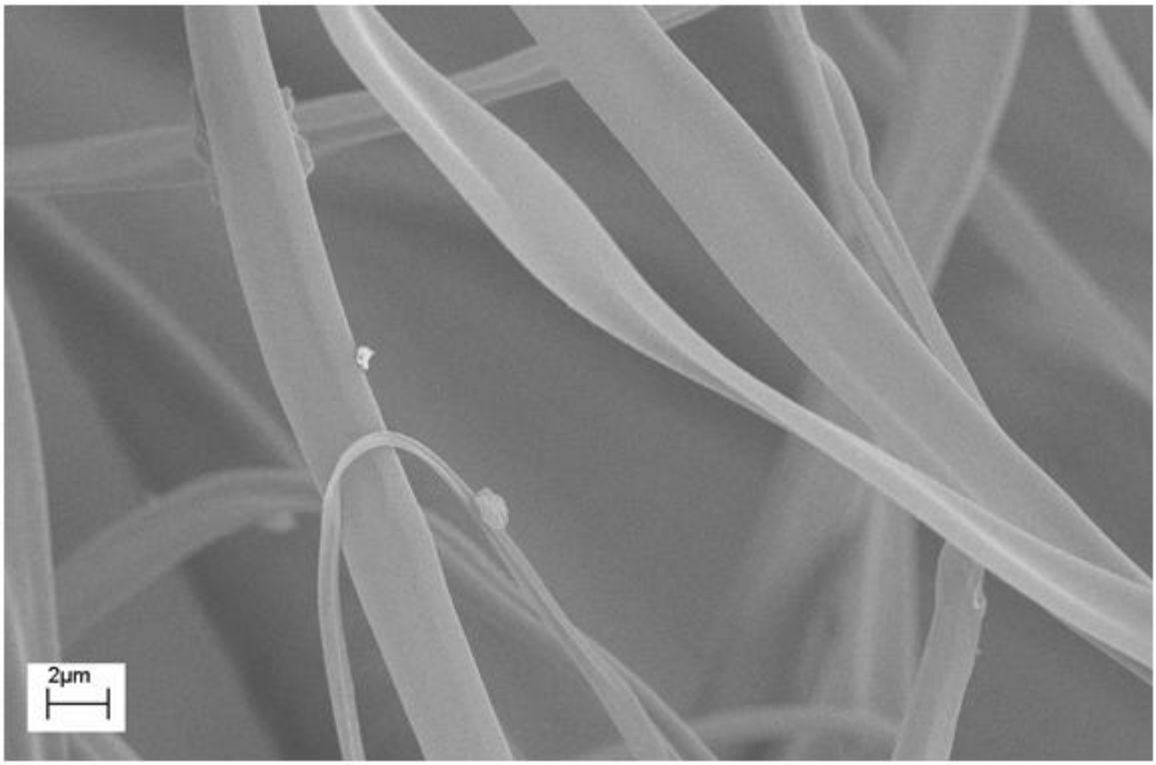

Figure 2.2 SEM micrograph of high concentration (20wt% in acetone) Polyvinylpyrrolidone fibers with micro belt morphology.

2.1.2. Processing parameters

a. Applied Voltage- Only the applied voltage is exceed the threshold limit, charged jets ejected from the Taylor Cone[3]. It is generally considered that high applied voltage favors the narrowing of fiber diameter due to high electrostatic force.

However, the level of affect varies depending on the solution parameters.

b. Flow rate/Feed rate- Flow rate is the rate at which the precursor is ejected from a syringe by syringe pump. Generally, as the flow rate increase, the diameters of electrospun fibers also increase. If the flow rate is too high, bead fibers form easily because the short evaporation time of solvent reduce before it deposit the collector.

c. Type of Collector used- A conductive substrate is commonly use as the collector. Aluminium foil is the most common however other types of collectors such as, rotating rod and rotating wheel have been used to produce aligned fibers.

d. Tip to Collector Distance- Tip to collector distance is determined by a minimum distance requiring the fibers to dry before reaching the collector. If the distance is too short or far, bead fibers or nanotube formation has been observed.

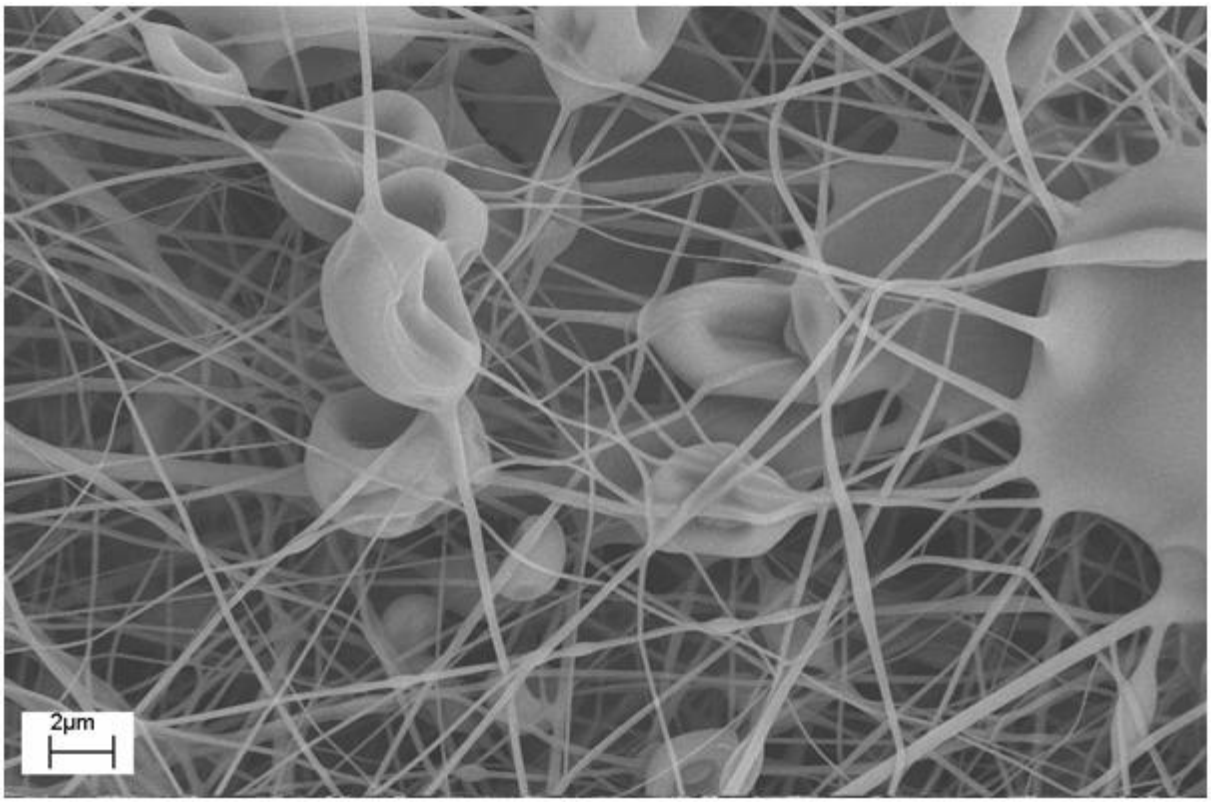

Figure 2.3 SEM micrograph of Polyvinylpyrrolidone (10wt% in ethanol) bead nanofibers with too high flow rate (0.08ml/min).

2.1.3. Ambient parameters

Other than parameters mentioned above, temperature and humidity are other importance parameters.

a. Temperature- Mittuppatham et al.[4] have shown that as ambient temperature is increased, the fiber diameters is decreased with polyamide-6 fibers.

b. Humidity- It is generally known that low humidity is preferred electrospinning since polymer jets easily evaporate solvent during the extrusion. Whereas high humidity gives beads formation so it needs extra attention dealing with water soluble polymers.

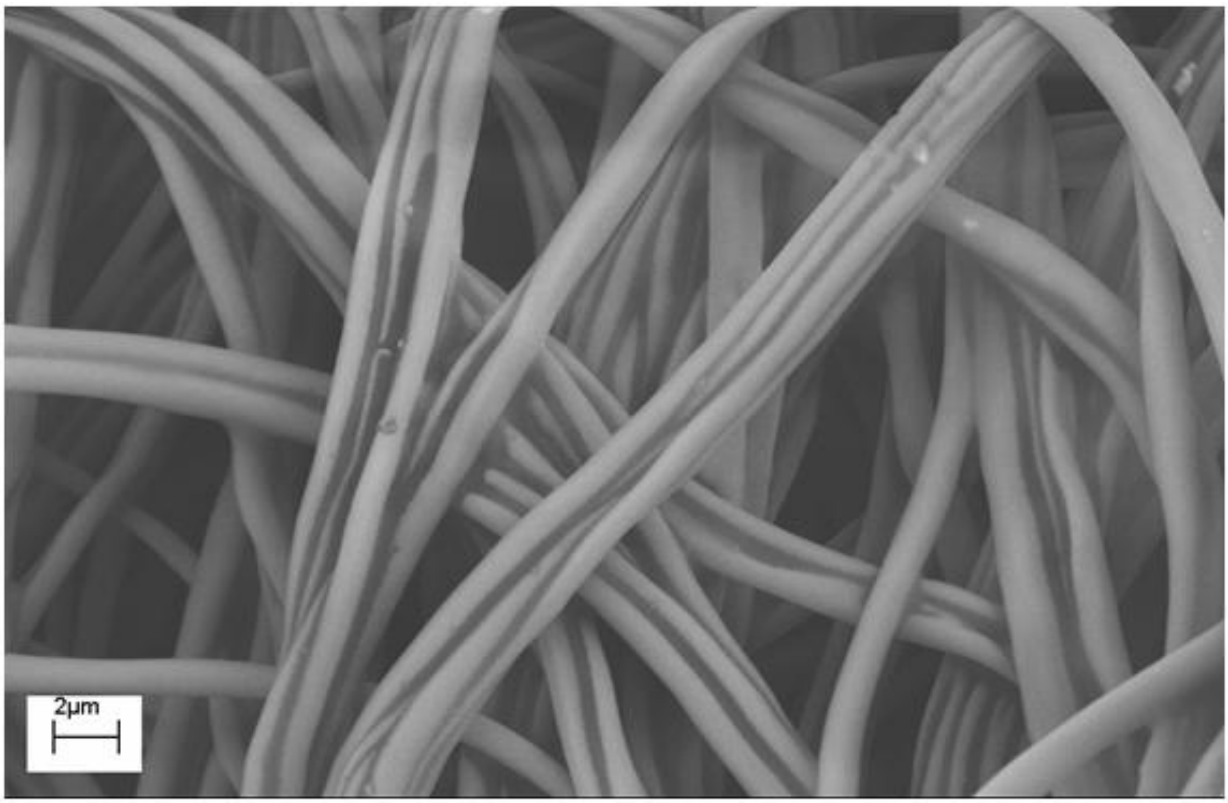

Figure 2.4 SEM micrograph of Polyvinylpyrrolidone (10wt% in ethanol) nanofibers in high humidity with fiber bundle morphology.

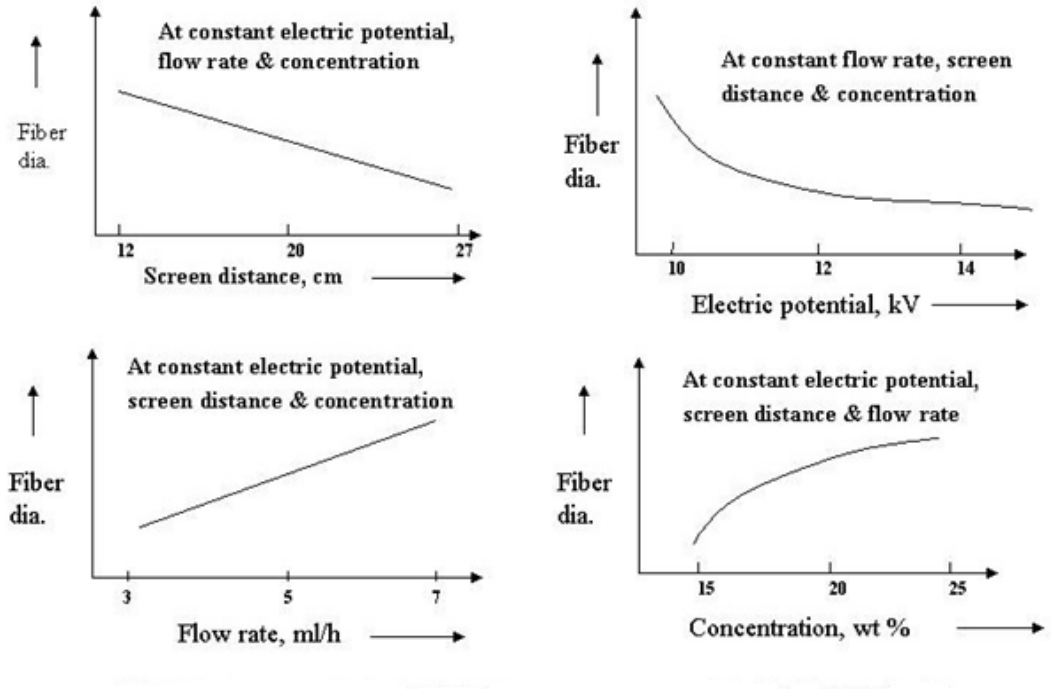

Figure 2.5 Effect of several parameters on electrospun fiber diameters (Wilkes, Garth, Electrospinning. retrieved October 13, 2013, from http://www.che.vt.edu).

2.2. Scanning Electron Microscope (SEM)

Scanning Electron Microscope (SEM) is a type of electron microscope which utilizes a beam of electrons produced from heating metallic filament to produce image. A largely magnified SEM Image obtains from electron beam interaction with the atoms of the specimen, producing signals containing information of the sample's topography, composition and properties like electrical conductivity and more. With SEM's narrow electron beams, high resolution and high depth of field can be achieved.

In this project LEO 1550 Schottkey field emission SEM was used to analyze the synthesized nanostructured metal oxides. The analysis was done to observe the morphology, including the grain sizes, grain distribution. SEM images obtained with back scattered signal of EHT 15~20 kV and working distance 7~15 mm depending on their conductivity of specimens. Some of the samples were coated with a thin layer of gold to enhance the surface conducted of samples.

2.3. Transmission Electron Microscope (TEM)

Transmission electron microscope (TEM) is another type of electron microscope which utilizes a beam of electron to transmit through a thin sample producing high resolution images and electron diffraction patterns. An electron beam source located at top of the TEM travel through vacuum in the column of the microscope. Some of the electrons are scattered and disappear from the beam An image is formed from the interaction of the electrons transmitted through the specimen and focused onto a fluorescent screen.

In this project, we use JEOL 1400 and 2100 with copper grid to observe the morphology and diffraction pattern of crystals.

2.4. Ray Diffraction (XRD)

X-Ray Diffraction (XRD) is a versatile and non-destructive analytical technique in which helps to examine the phase of a crystalline of materials. The atomic planes of crystal cause an incident beam of X-rays to the interference with one another as they leave the crystal. The interaction of the projected rays onto the specimen produces constructive interference when conditions satisfy Bragg's Law:

$n\lambda = 2d \sin \theta$

where n is an integer, λ is the X-ray wavelength, d is the interplanar spacing of the crystal and θ is the angle of incidence

Every crystalline phase produce corresponding diffraction pattern therefore the diffraction patterns are considered as "finger prints" for each phase.

The obtained XRD patterns can be used to calculate the size of crytalities by using Scherrer equation:

$$\tau = \frac{\kappa\lambda}{\beta \cos\theta}$$

Where, τ is the mean size of grain size, κ is a dimensionless shape factor commonly 0.9, λ is the wavelength of the incident X-rays, β is the line broadening at half the maximum intensity, and θ is the Bragg angle.

In this thesis, a Philips powder XRD was used to characterize the synthesized specimens.[11]

Reference

1. Zeleny, J., The Electrical Discharge from Liquid Points, and a Hydrostatic Method of Measuring the Electric Intensity at Their Surfaces. Physical Review, 1914. **3**(2): p. 69-91.

2. Reneker, D.H. and A.L. Yarin, Electrospinning jets and polymer nanofibers. Polymer, 2008. **49**(10): p. 2387-2425.

3. Zhenyu Li and C. Wang, One-Dimensional nanostructures

   Electrospinning Technique and Unique Nanofibers. SpringerBriefs in Materials

   2013: Springer. 179

4. Mit-uppatham, C., M. Nithitanakul, and P. Supaphol, Ultrafine Electrospun Polyamide-6 Fibers: Effect of Solution Conditions on Morphology and Average Fiber Diameter. Macromolecular Chemistry and Physics, 2004. **205**(17): p. 2327-2338.

5. Wegner, K. and S.E. Pratsinis, Scale-up of nanoparticle synthesis in diffusion flame reactors. Chemical Engineering Science, 2003. **58**(20): p. 4581-4589.

6. Teoh, W.Y., R. Amal, and L. Madler, Flame spray pyrolysis: An enabling technology for nanoparticles design and fabrication. Nanoscale, 2010. **2**(8): p. 1324-1347.

7. Strobel, R., A. Alfons, and S.E. Pratsinis, Aerosol flame synthesis of catalysts. Advanced Powder Technology, 2006. **17**(5): p. 457-480.

8. Ulrich, G.D., Theory of Particle Formation and Growth in Oxide Synthesis Flames. Combustion Science and Technology, 1971. **4**(1): p. 47-57.

9. Marshall, B.S., I. Telford, and R. Wood, A field method for the determination of zinc oxide fume in air. Analyst, 1971. **96**(1145): p. 569-578.

10. Sokolowski, M., et al., The "in-flame-reaction" method for Al2O3 aerosol formation. Journal of Aerosol Science, 1977. **8**(4): p. 219-230.

11. Patterson, A.L., The Scherrer Formula for X-Ray Particle Size Determination. Physical Review, 1939. **56**(10): p. 978-982.

Chapter 3 Synthesis and Characterization of Visible-Light Activated CuO-TiO_2 Nanofibrous Mats

3.1. Introduction

Ever since Fujishima and Honda[1] discovered water-splitting effect on TiO_2, there have been extensive studies on TiO_2. Titanium oxide has many advantages as a photocatalyst, such as chemical stability, inert nature, and cost effectiveness, resulting in one of the most commonly used photocatalyst in the environmental and energy- related fields[2, 3].

However, pure TiO_2 is not used in water remediation due to the dispersed nature of the catalytic nanoparticles and the need for UV illumination. In addition, the major disadvantage of TiO_2 is its relatively wide band gap necessitating light wavelengths below 400nm for electron and hole separation [2b]. Researchers have developed two strategies to expand its light absorption range. The first one is by incorporating an organic dye as a photosensitizer; the second is by doping TiO_2 with metallic/nonmetallic elements[4].

This doping introduces either occupied orbitals (which leads to negative doping) or unoccupied orbitals (which leads to positive doping) in the band gap area of the semiconductor, thereby reducing the band gap. In the past, TiO_2 has been doped with various metals like Fe, Pd, Pt, Cr, and rare-earth metals causing a large shift in its absorbance band, moving into the visible region [5]. It has been observed that there is an optimal value or level for doping TiO_2 which in many cases is between 3-7 wt% in order to reach maximum efficiency of the catalyst[6]. Although doping with novel metals like Pt exhibited high photocatalytic activity by reducing the recombination of photogenerrated electron-hole pairs, its high cost and indefinite sustainability have led researchers to use other potential dopants[7]. Transition metals like copper are available at low cost. There have been few investigations done on the doping of copper with titania[8] resulting in enhanced photocatalytic activity, hydrogen generation [9] and carbon dioxide reduction[10]. Helaili et al. [11] in 2009 have shown that a modification to the optical property of TiO_2 was brought about by the copper doped TiO_2 nanoparticles, enabling the composite material to show activity in the UV-visible region of solar radiation, enhancing the degradation of organic pollutants 32 times faster than bare TiO_2. However, the photocatalytic nanoparticles combined to form aggregates which become attractive sites for the photogenerated electrons and holes,

leading to recombination reactions and rapid loss in active sites ultimately hindering photocatalysis [12,13]. Considering these effects of nanoparticles, research has advanced and synthesized nanotubes of CuO which had TiO_2 nanoparticles decorated on it which was shown be highly active photocatalysts when used to decolorize methyl orange dye [14]. Nevertheless, it was noticed that this morphology of the TiO_2 nanoparticles on the CuO nanotube resulted in low surface area of the nanotube available for dye adsorption [14]. Particle agglomeration produced an uneven structure, decreasing the contact between CuO nanotubes and TiO_2 nanoparticle[14]. Hence, it has been a challenge to eliminate this agglomeration effect so as to produce effective and efficient photocatalysts.

The fabrication of micro- or nano- TiO_2 structures with different morphologies and properties has been investigated by several researchers[3] and especially one-dimensional structure of fibers, which can be obtained from electrospinning or anodization methods, may show lower levels of recombination because of the short distance for charge carrier diffusion[15].

In this study, CuO-TiO_2 nanofibrous mats photocatalysts were successfully fabricated by a blend electrospinning method. The key features of the synthesized photocatalysts were: nanofibrous mats for high surface area with no agglomerates and copper doping for reducing the band gap for visible light activation.

3.2. Experimental Procedure/Methods:

3.2.1. Preparation of pure TiO_2 and CuO-TiO_2 nanofibrous mats

All the chemicals were used as-received without further treatment. In the case of doping titania with copper, 5 atom weight percent of copper with respect to titanium, was decided to be used for doping after a literature review of the doping levels and their effects[6]. The titanium precursor was prepared by mixing 2ml Titanium isopropoxide, Ti $(OC_4H_9)_4$ (Alfa Aesar) with 2ml of acetic acid in N_2 atmosphere. The precursor was allowed to rest for 30 min before being added into 4 ml of 0.1mM polyvinylpyrrolidone (PVP, M_W= 1,300,000)(Sigma Aldrich) solution in ethanol. The CuO-TiO_2 nanofibrous mats precursor was prepared by adding 0.5ml of 2.6×10^{-4} mol $3HO_2{\bullet}Cu(NO_3)_2$ (sigma-aldrich) in ethanol into the titanium precursor. The prepared solutions were ultrasonicated for 60min before being poured into a plastic syringe for further electrospinning process. A blunt-ended 22-gauge stainless needle was used as nozzle. A

high voltage power supply was attached to needle as working electrode and aluminum foil was used as ground electrode placed on collecting screen. The steady jet was maintained for all combinations at a flow rate of 0.045ml/min, applied voltage of 19-22kV, and a fixed needle-to-collector distance of 15cm. The as-received fibrous mats were placed in a humidity controlled chamber. The collected as-electrospun fibers were subsequently subjected to an oxidizing heat-treatment in a tube furnace (Lindberg Blue) at 450℃ for 1 hour. In order to analyze the microstructure, electrospun mats were characterized by scanning electron microscopy (SEM, LEO 1550 Schottkey Filed Emission SEM) and transmission electron microscopy (TEM, JEOL 1400). The light absorbance of the electrospun mats was examined with the UV-Vis Spectrometer (UV-Vis, Jasco J-815).

3.2.2. Photocatalytic degradation of Methylene Blue (MB)

In a typical experiment, 0.018g of the catalysts was added to a 4ml methylene blue (MB) dye solution of 50ppm concentration in distilled water. This was kept in the dark for 1 hour to obtain an adsorption-desorption equilibrium. A light source with a 150W Xenon light bulb (Newport) with AM 1.5 was used as the source for UV-visible and visible light by using a 400nm cut-on filter in the same set up. The solution was then kept under the UV-visible or visible light for 3 hours. Every 1 hour 2ml of the solution was taken out to measure its absorbance value with the spectrophotometer and it was poured back after the measurements. The degradation of methylene blue was evaluated by studying the changes in the absorbance value at a wavelength of 665nm using UV/Vis spectrophotometer (HR 4000, Ocean Optic) with halogen and deuterium as light sources.

3.2.3. Photoelectrochemical characterization

Photo-electrochemical measurements were carried out in a conventional three-electrode, single-compartment glass cell fitted with a quartz window. Working electrodes were prepared by mixing the pure TiO_2 nanofibrous mats or the CuO-TiO_2 nanofibrous mats annealed at 450℃ for 1h with 0.1mM PVP in isopropanol alcohol and drop casting onto ITO glass substrate to form a thin film. The pure TiO_2 and CuO-TiO_2 nanofibrous mats deposited on ITO glass were annealed at 450℃ for 10 min with rapid thermal processor (RTP). The electrolyte used was a 0.1M KOH solution after being de-aerated by bubbling with N_2. A platinum wire (BASi) was used as a

counter electrode and an SDR-2 (World precision Instruments) as a reference electrode. The working electrode was placed at the optical path with $1cm^2$ of electrode area. A potentiostat (Princeton Applied research) was employed for the cyclic voltammetry and chronoamperometry measurements. The surface of the working electrode was illuminated with light intensity of $113.0mW/cm^2$ from a 150W Xenon lamp (Newport) equipped with an AM1.5G filter.

3.3. Experimental results

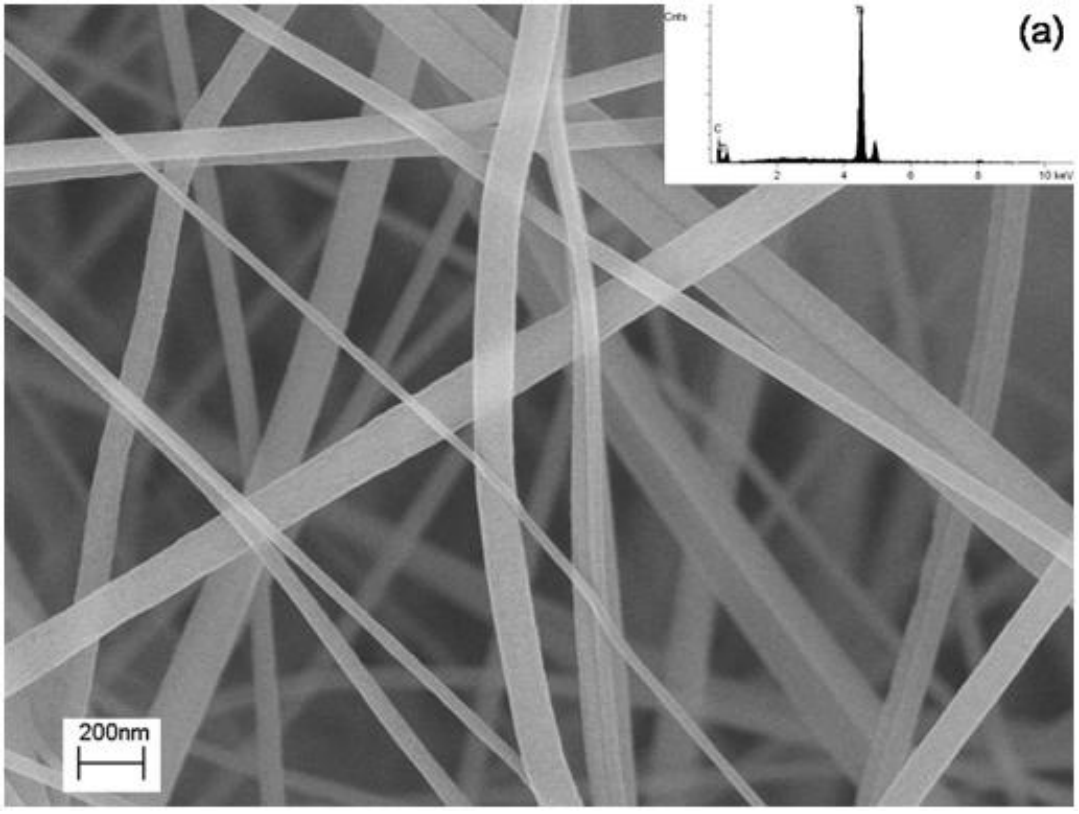

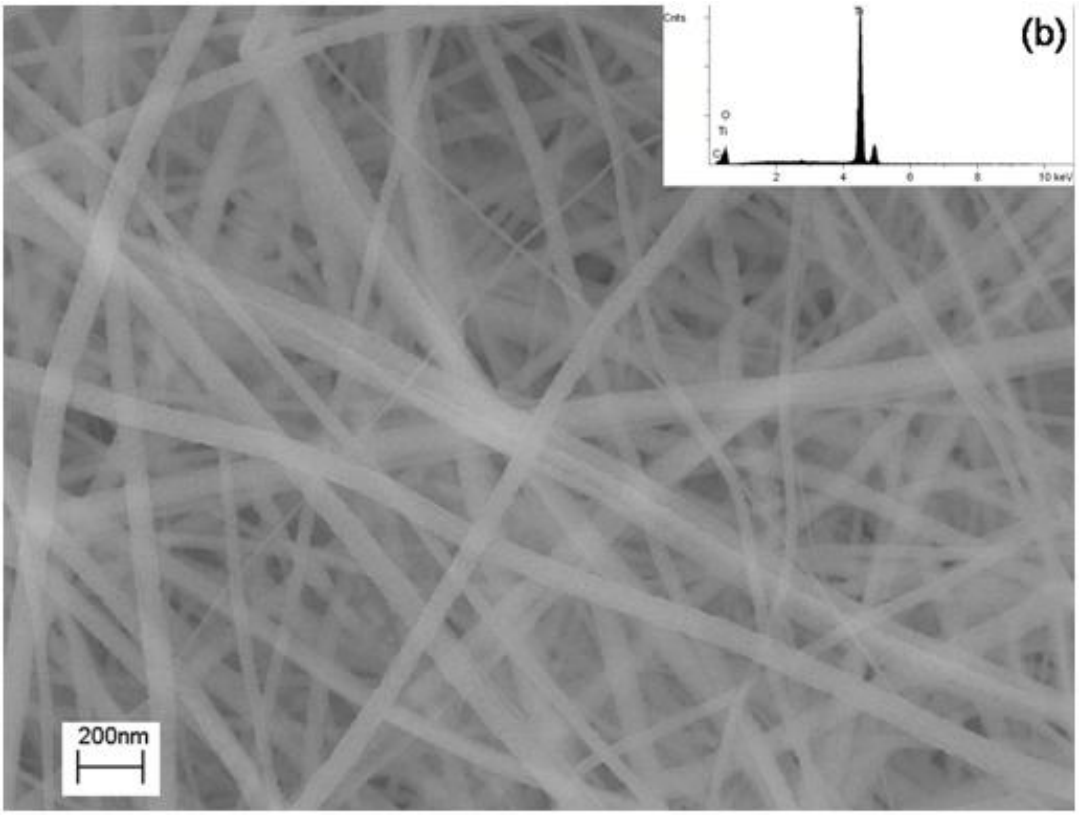
(b)
Cnts
Ti
O
Ti
2
4
6
8
10 keV
200nm

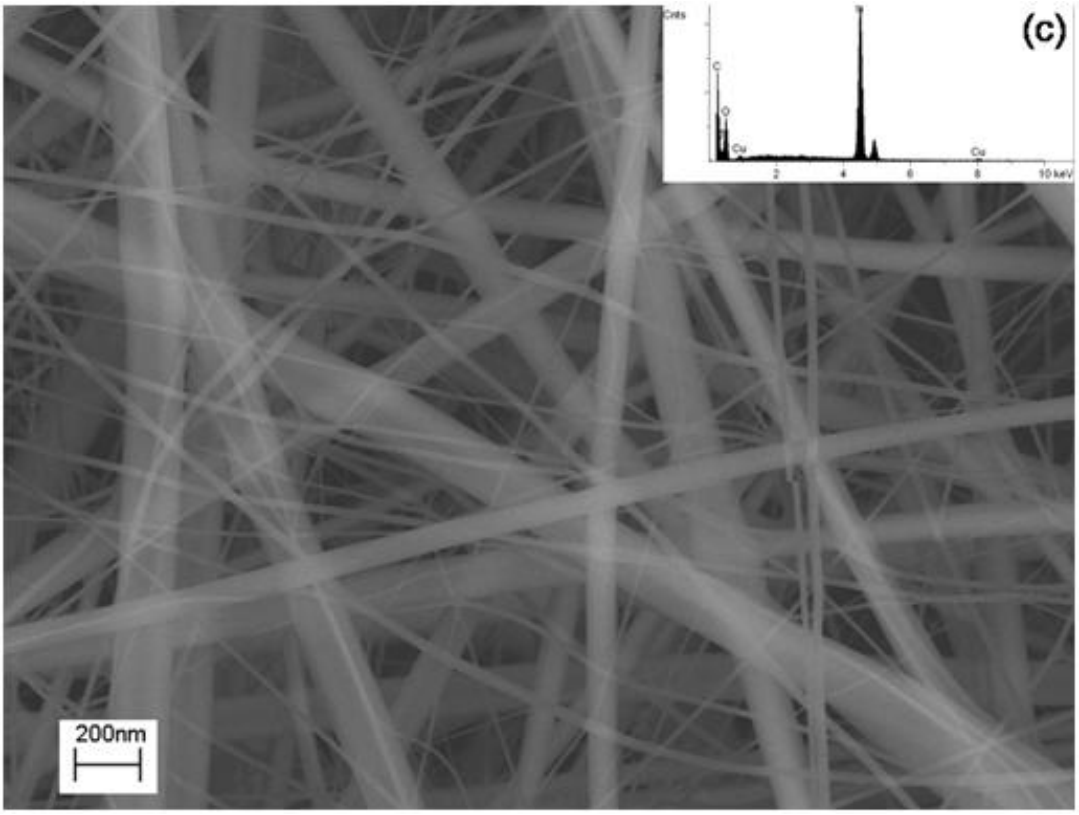
(c)
Cnts
Ti
C
O
Cu
Cu
2
4
6
8
10 keV
200nm

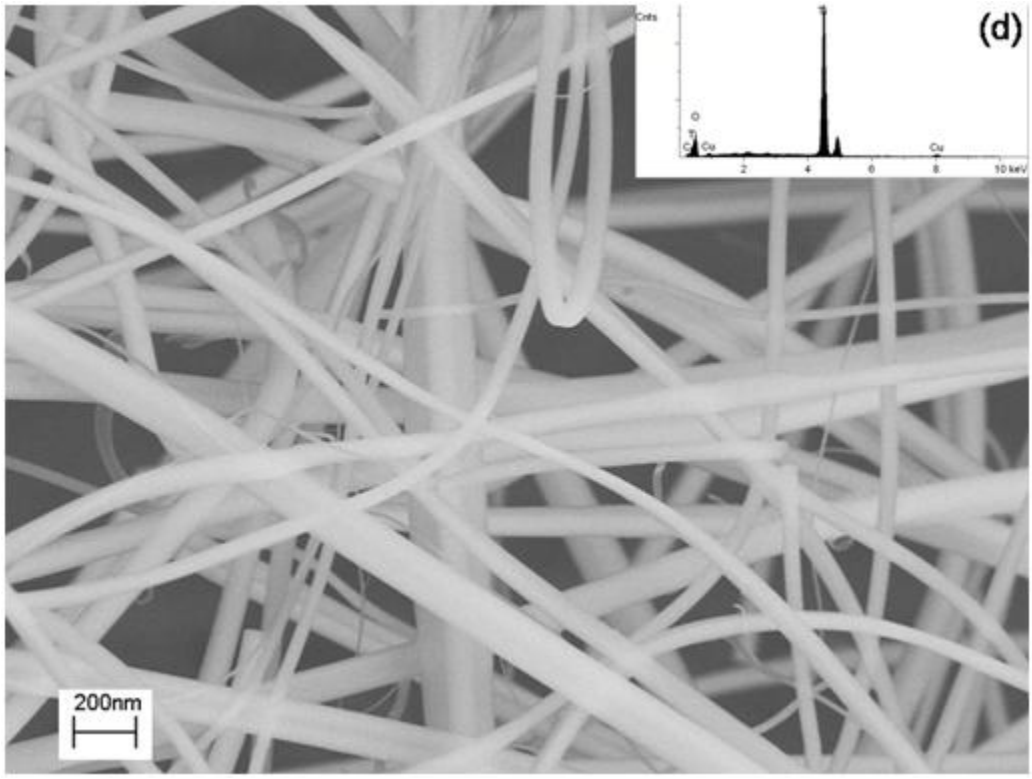

Figure 3.1 (a) SEM image of as-spun pure TiO_2 nanofibrous mats, (b) pure TiO_2 nanofibrous mats annealed at 450 ℃, (c) As-spun CuO-TiO_2 nanofibrous mats, and (d) CuO-TiO_2 nanofibrous mats annealed at 450 ℃ with EDAX as insets.

The morphology and structural properties of the electrospun mats before and after annealing were studies using a SEM (LEO 1550). The samples were coated with gold using a vacuum sputter-coater before imaging to reduce charging effects. Figures 3.1(a) and(c) below show the SEM images of as-spun TiO_2 fibers and of the CuO-TiO_2 fibers respectively while Figures 3.1(b) and (d) show images of their counterparts heat-treated at 450^0C for 1 hour. The EDX spectra (insets) are also attached

The differences in morphology and size of fibers can be observed in both these images. The as-spun fibers of both types have diameters in the range of 50-200nm whereas the heat-treated fibers which have diameters in the range of 20-100nm. This decrease in size of the fibers after calcination is due to the loss of the carrier polymer during the heat treatment. The polymer used in this work was PVP which has a melting point of 150°C. At 450°C, most of the PVP was

burned out. Another noted morphological difference is the smoothness of fibers in the as-spun fiber image. These seem to have well defined contrary to the annealed fibers that seem to have rough outlines or edges. This is due to the crystallization of the oxide fibers.

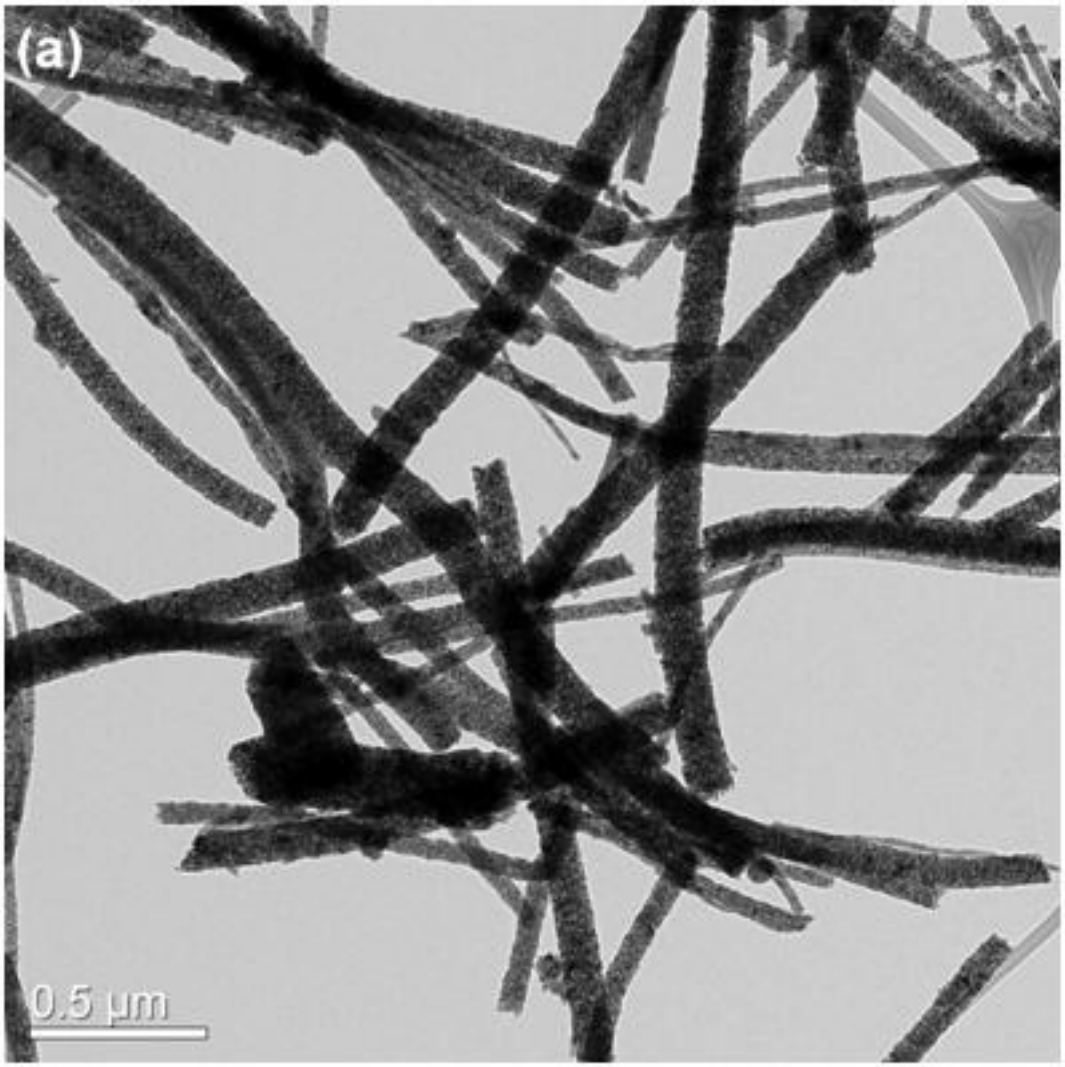

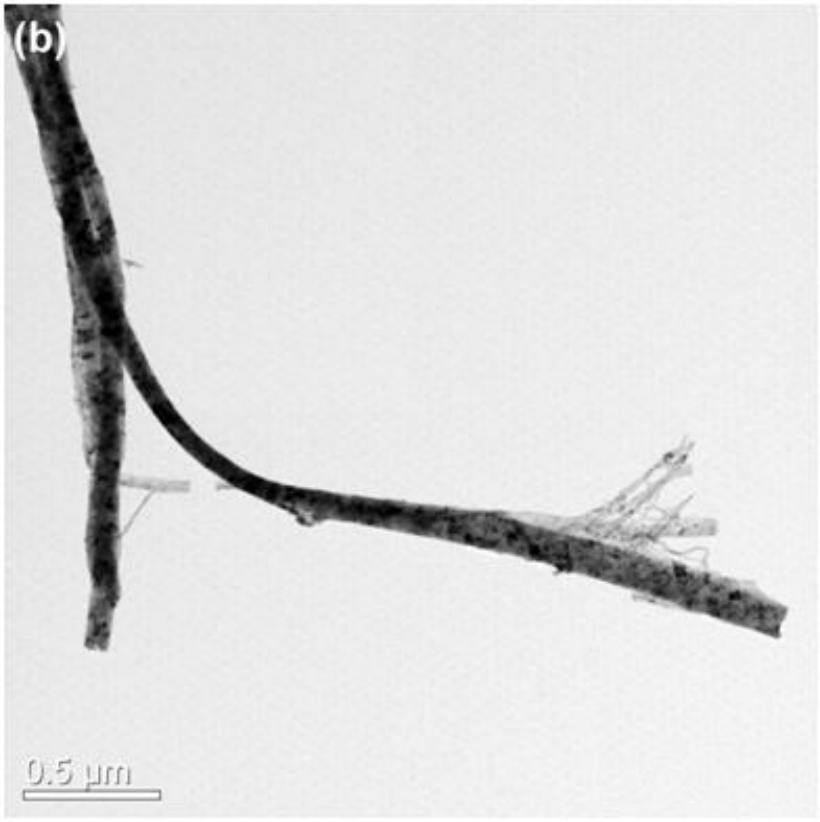
(b)
0.5 µm

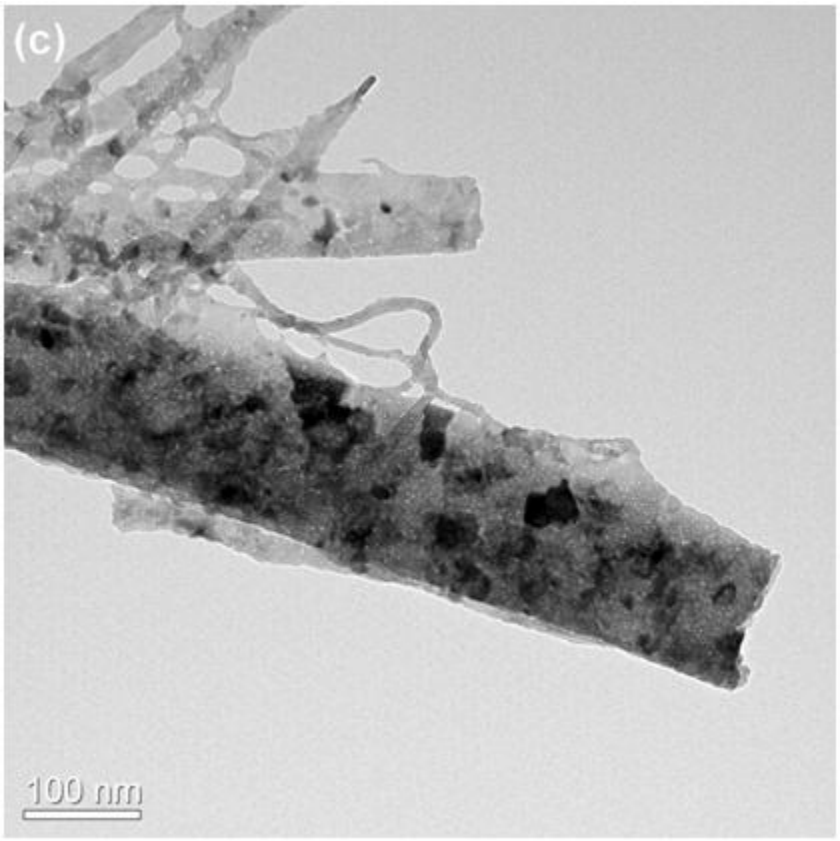
(c)
100 nm

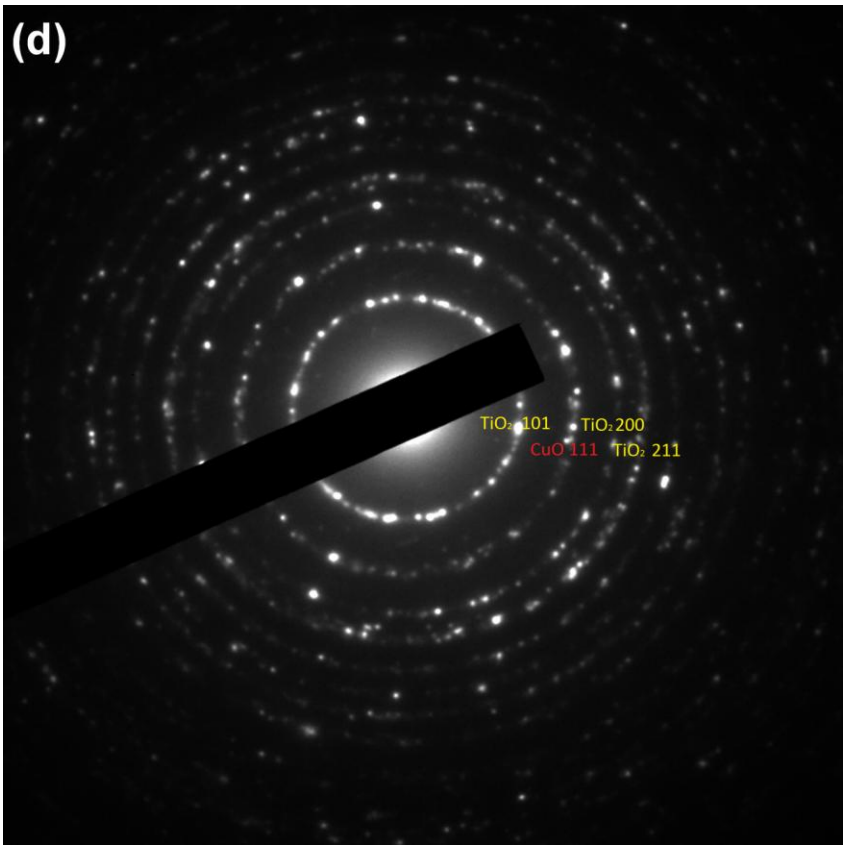

Figure 3.2 (a) TEM image of pure TiO_2 nanofibrous mats annealed at 450^0C, (b) CuO-TiO2 nanofibrous mats annealed at 450 ℃, low magnification, (c) high magnification, and (d) SAED patterns of CuO-TiO2 nanofibrous mats annealed at 450 ℃.

Degussa P-25 is the most commonly used commercial photocatalyst which contains physical mixing anatase and rutile in a ratio of about 3:1 [26]. Ohno et al.[26] showed that the average sizes of the anatase and rutile elementary parties are 85 and 25 nm. The corresponding XRD test results, Figure S3.2, also show that phase change occurred upon heat treatment. When the annealing temperature is at 400℃, there are only anatase peaks appealed and as heating temperature is increasing anatase peaks disappeared and rutile peaks were grown. The XRD peak result at 550℃ showed most similar to P-25 but low intensity. For the future synthesis process, it may worth to try heating at 550℃ and longer annealing time.

Figure 3.2 (a) shows the TEM image of pure TiO_2 nanofibers. It is observed in these images that the TiO_2 nanofibers have a polycrystalline nature with fiber diameters in the range of 100nm and the surface of fibers is rough and highly porous.

The TEM image of CuO-TiO_2 nanofibrous mats is shown in Figure 3.2 (b) and (c). The selected area diffraction patterns (SAED) of the same fibers is shown in Figure 3.2(d). The ring pattern indicates that the fibers consist of nanocrystals and the ring pattern corresponds to planes: TiO2 (101), CuO (111), TiO2 (200), TiO2 (211), and TiO2 (204), respectively. (JCPDS 21-1272 and 45-937).

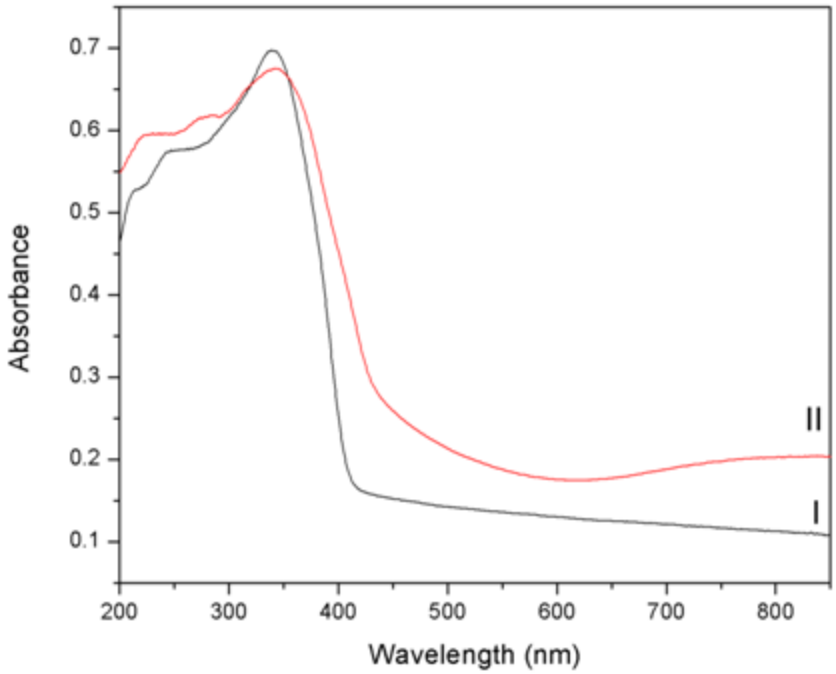

Figure 3.3 UV-Vis spectra of I. pure TiO_2 and II. CuO-TiO_2 nanofibrous mats annealed at 450 ℃.

Figure 3.3 shows the UV-Visible spectra of pure TiO_2 and CuO-TiO_2 nanofibrous mats respectively. The absorption spectrum of pure TiO_2 nanofibrous mats was cut off at ~405nm,

from which the band gap of the pure TiO_2 nanofibrous mats was estimated to be 3.06eV. For the CuO-TiO_2 nanofibrous mats, the cutoff edge of the adsorption spectrum extended to 450nm (corresponding band gap 2.76eV) along with an observed baseline curve shift up, corresponding to their brown color. Energy gap of the CuO-TiO_2 system allows for light absorbance enhancement from 405 to 450 nm in the near-UV region and in the visible light range [16].

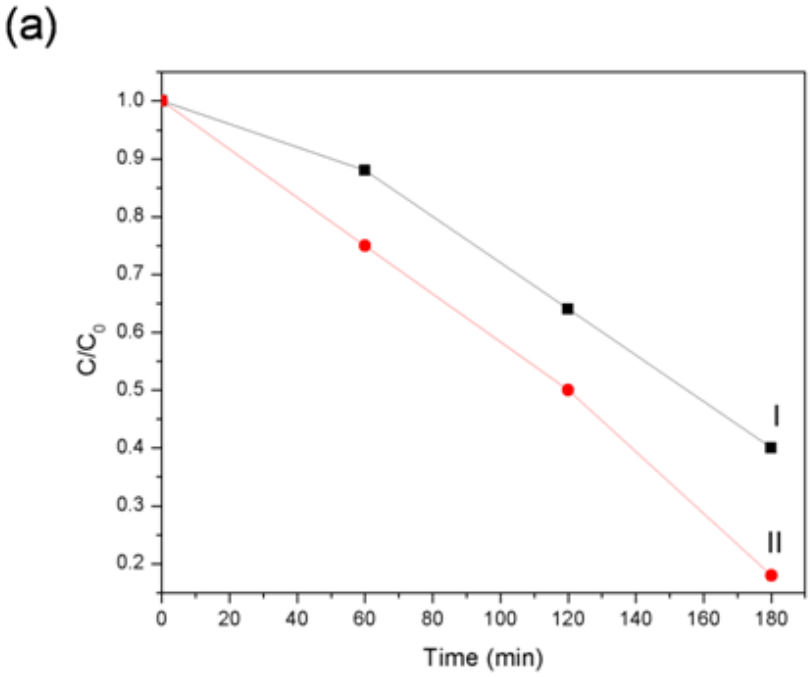

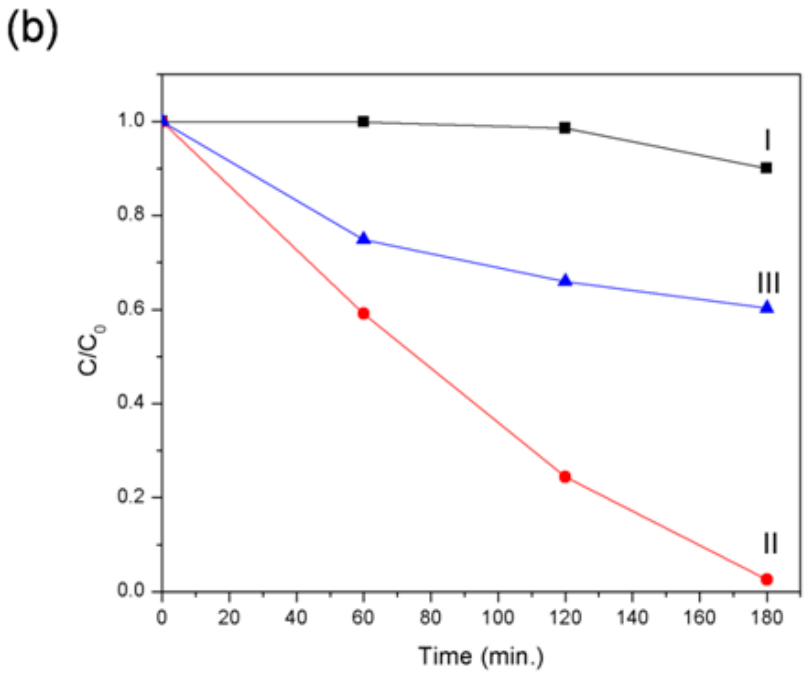

Figure 3.4 Photodegradation of MB under (a) UV-visble light and b) visible spectrum (λ>400nm) of I. P25, II. TiO_2/CuO nanofibrous mats , and III. pure TiO_2 nanofibrous mats.

The photocatalytic activities of the fibers were evaluated by monitoring the degradation of methylene blue (MB) solutions (50ppm MB in distilled water) under UV-visible and visible light irradiation, respectively. The Y-axis has the absolute value of absorbance obtained by dividing the absorbance value at time C by the absorbance value at time C_0= 0 minutes. These absolute absorbance values were plotted against time for each catalyst. Figure 3.4(a) shows degradation curve of methylene blue by P25 and CuO-TiO_2 nanofibrous mats under 150W xenon lamp light irradiation with AM1.5. The photocatalytic activity result showed that CuO-TiO_2 nanofibrous mats performed better than P25 under UV and UV-visible spectrum. Figure 3.4(b) shows pure TiO_2 nanofibrous mats, CuO-TiO_2 nanofibrous mats and P25 (Sigma Aldrich) under visible light (λ > 400nm). There is a large increase in the degradation percentage (97%) by using the CuO-TiO_2 nanofibrous mats upon visible light irradiation. Furthermore, it is worth to noticing that there was 40% of degradation of MB pure TiO_2 nanofibrous mats as well.

To the best of my knowledge, there is just a single report in the literature for electrospun CuO doped titania fibrous photocatalysts by Lee. et al. [17], the TiO_2/CuO composite nanofibers was synthesized by electrospinning a mixture of PVP, $Ti(oBu)_4$, and $Cu[CH_3(CH_2)_3CH(C_2H_5)CO_2]_2$) and their photocatalytic degradation of Acid Orange 7(AO7) was tested by measuring H_2 generation only under UV-visible light illumination. Our research shows for the first time that a visible light activated self-supporting CuO-TiO_2 nanomats can achieve a degradation level of 97% for methylene blue aqueous solutions.

3.4. Understanding the operating mechanism for the photocatalytic of the cuo-tio2 system

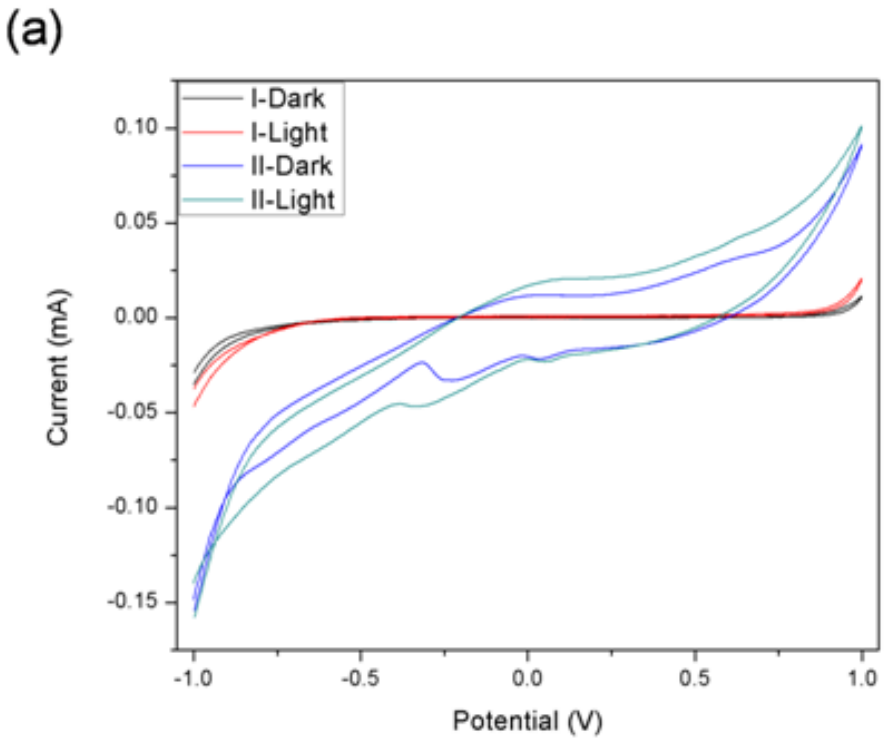

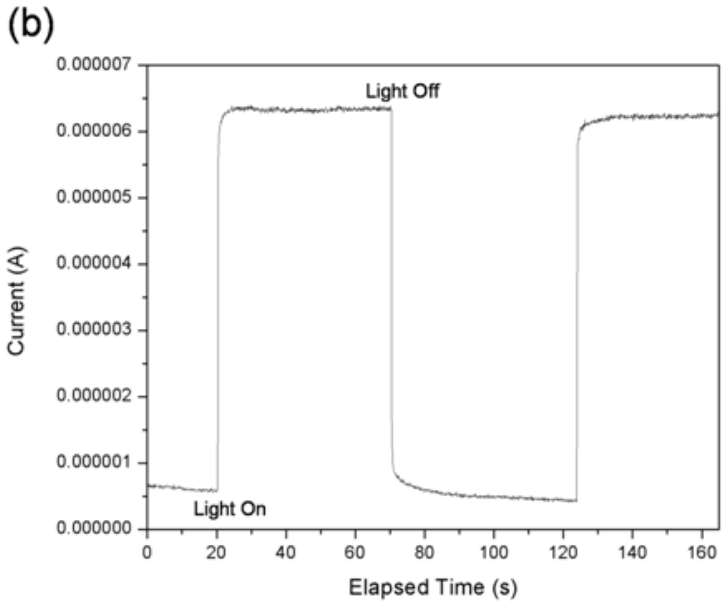

Figure 3.5 (a) Cyclic voltammograms of the I. pure TiO_2 and II. CuO- TiO_2 nanofibrous mats both in the dark and with light irradiation in 0.1M KCl solution.(b) Chronoamperometry curve of CuO-TiO_2 nanofibrous mats corresponding light switching "ON" and "OFF" curve.

The electrochemical behavior of CuO-TiO_2 nanofibrous mats was studied using cyclic voltammetry (CV) in 0.1M KOH solution in the range of -1 to 1V. Figure 3(a) shows the CV curves of the pure TiO_2 and of the CuO-TiO_2 nanofibrous mats taken at a scanning rate of 20 mV/s under dark and light conditions. The cyclic voltammetry curve of the pure TiO_2 fibers shows no obvious oxidation or reduction peaks. The difference in the current values on the edge of the curves may be due to photocurrent from pure TiO_2 nanofibrous mats upon light illumination [18].

For CuO-TiO_2 nanofibrous mats, one anodic peak at around -0V(A_1) and two cathodic peaks at around -0.25V (C_1) and 0.04V(C_2) are seen here. The large peak potential separation between the anodic and cathodic peaks may relate to the low electronic conductivity of the nanofibrous mats [19,20]. The appearance of an anodic peak, A_1 and cathodic peak, C_1 and C_2 may be related to the following chemical reactions: [21,22]

$$Cu(OH)_2 + 2\,e \leftrightarrow Cu + 2\,OH^- \qquad (A_1)$$

$$½\ Cu_2O + ½\ H_2O + e \leftrightarrow Cu + OH^- \qquad (C_1)$$

$$Cu(OH)_2 + \ e \leftrightarrow ½\ Cu_2O + OH^- + ½\ H_2O \qquad (C_2)$$

$$E = E^0 - \frac{0.05916}{n} \log_{10} \frac{[Red]}{[Ox]}$$

The value of E^0 of A_1, C_1, and C_2 is -0.222, -0.360, and -0.080 V (vs. Ag/AgCl). The calculated E of A_1, C_1, and C_2 is -0.163, -0.301, and -0.021 (vs. Ag/AgCl). It is worth to note that broad oxidation peak A_1 is corresponding to the 2 electrons pair Cu^{II}/Cu^0 and each reduction peak is corresponding to a 1 electron pair, namely Cu^{II}/Cu^I and Cu^I/Cu^0.

The redox reaction involves transition between Cu and Cu(I) oxide and similar behavior has been reported for transition metals in alkali solutions. Cu(II) oxide only formed in solution from the slow dehydration of $Cu(OH)_2$. During the CV measurement whole cycle was completed with approx 1min therefore CuO is not expected to form. The peak potential shifted to more anodic and cathodic direction under light illumination.

The photoresponsive switching behavior of the CuO-TiO_2 nanofibrous mats is shown in Figure 3(b), which illustrates that the photocurrent can be reproducibly switched "Light On" and "Light Off", under Xenon 150W lamp with AM 1.5. The response and decay time is almost instant and the photocurrent was stable and reproducible. With a 0.5V applied bias, the dark reverse leakage current of the CuO-TiO_2 nanofibrous mats was approximately 0.675 μA but the current increased rapidly to 6.45 μA upon light illumination. In the dark, a low-conductivity depletion layer formed near the surface due to the capturing of free electrons in the n-type semiconductor by absorbed oxygen molecules on the oxide surface [$O_2(g) + e^- \rightarrow g_2^-(ad)$]. Upon light illumination, photogenerated holes from the charge separation discharge adsorbed oxygen ions [$h^+ + O_2^- \rightarrow O_2(g)$], enhancing the materials' conductance [25].

The relatively high photocurrent-to-dark-current contrast ratio and the fast responses observed suggest that the CuO-TiO_2 nanofibrous mats described in this work are potentially

useful for highly efficient visible light-activated photocatalysts. The observed improvement in the photocatalytic properties could STEM from a number of factors that need to be studies further. P-n junctions or spillover effects may contribute to the observed results and further studies are under way to elucidate the operating mechanism in our system.

3.5. Conclusions

The photocatalytic activities of the pure TiO_2 and CuO-TiO_2 nanofibrous mats catalysts have been demonstrated under UV light and under visible light. Electron microscopy characterization methods used that helped us understand the morphology and structure of the nanofibrous mats. The UV-Vis spectroscopy results indicated that, based on the degradation of MB solution, the nanofirbous mats are strongly effective visible light activated photocatalysts that offer 97% dye degradation under visible light. Under the same conditions, the commercial titanium dioxide (degussa P25) showed a weak 11% degradation. The relatively high photocurrent-to-dark-current contrast ratio and the fast responses also suggest that the CuO-TiO_2 nanofibrous mats described are potentially useful for highly efficient visible light-activated photocatalysts for environmental and energy applications.

Reference

1. Fujishima, A.; Honda, K., Electrochemical Photolysis of Water at a Semiconductor Electrode. Nature 1972, 238 (5358), 37-+.

2. (a) Carp, O.; Huisman, C. L.; Reller, A., Photoinduced reactivity of titanium dioxide. Progress in Solid State Chemistry 2004, 32 (1-2), 33-177; (b) Colmenares, J. C.; Luque, R.; Campelo, J. M.; Colmenares, F.; Karpinski, Z.; Romero, A. A., Nanostructured Photocatalysts and Their Applications in the Photocatalytic Transformation of Lignocellulosic Biomass: An Overview. Materials 2009, 2 (4), 2228-2258.

3. Nakata, K.; Fujishima, A., TiO2 photocatalysis: Design and applications. Journal of Photochemistry and Photobiology C: Photochemistry Reviews 2012, 13 (3), 169-189.

4. (a) Pichat, P.; Guillard, C.; Maillard, C.; Amalric, L.; D'Oliveira, J., Titanium dioxide photocatalytic destruction of water aromatic pollutants: intermediates; properties-degradability correlation; effects of inorganic ions and titanium dioxide surface area; comparisons with hydrogen peroxide processes. Photocatalytic Purification and Treatment of Water and Air 1993, 207-23; (b) Yamashita, H.; Takeuchi, M.; Anpo, M., Visible-Light-Sensitive Photocatalysts. Encyclopedia of nanoscience and nanotechnology 2004, 10 (1), 639-654; (c) Bacsa, R.; Kiwi, J.; Ohno, T.; Albers, P.; Nadtochenko, V., Preparation, testing and characterization of doped TiO2 active in the peroxidation of biomolecules under visible light. Journal of Physical Chemistry B 2005, 109 (12), 5994-6003; (d) Jin, Z. L.; Zhang, X. J.; Li, Y. X.; Li, S. B.; Lu, G. X., 5.1% Apparent quantum efficiency for stable hydrogen generation over eosin-sensitized CuO/TiO2 photocatalyst under visible light irradiation. Catalysis Communications 2007, 8 (8), 126 7-1273; (e) Jin, Z. L.; Zhang, X. J.; Lu, G. X.; Li, S. B., Improved quantum yield for photocatalytic hydrogen generation under visible light irradiation over eosin sensitized TiO2 - Investigation of different noble metal loading. Journal of Molecular Catalysis a-Chemical 2006, 259 (1-2), 275-280; (f) Abe, R.; Sayama, K.; Arakawa, H., Dye-sensitized photocatalysts for efficient hydrogen production from aqueous I- solution under visible light irradiation. Journal of Photochemistry and Photobiology a-Chemistry 2004, 166 (1-3), 115-122; (g) Karakitsou, K. E.; Verykios, X. E., Effects of Altervalent Cation Doping of Tio2 on Its Performance as a Photocatalyst for Water Cleavage. Journal of Physical Chemistry 1993, 97 (6), 1184-1189.

5. Colmenares, J. C.; Aramendía, M. A.; Marinas, A.; Marinas, J. M.; Urbano, F. J., Synthesis, characterization and photocatalytic activity of different metal-doped titania systems. Applied Catalysis A: General 2006, 306 (0), 120-127.

6. (a) Chen, L. C.; Huang, C. M.; Tsai, F. R., Characterization and photocatalytic activity of K+-doped TiO2 photocatalysts. Journal of Molecular Catalysis a-Chemical 2007, 265 (1-2), 133-140; (b) Okato, T.; Sakano, T.; Obara, M., Suppression of photocatalytic efficiency in highly N-doped anatase films. Physical Review B 2005, 72 (11); (c) Fu, G.; Vary, P. S.; Lin, C.-T., Anatase TiO2 nanocomposites for antimicrobial coatings. The Journal of Physical Chemistry B 2005, 109 (18), 8889-8898; (d) Bensaha, R.; Bensouyad, H., Synthesis, Characterization and Properties of Zirconium Oxide (ZrO2)-Doped Titanium Oxide (TiO2) Thin Films Obtained via Sol-Gel Process. 2012.

7. Chong, M. N.; Jin, B.; Chow, C. W. K.; Saint, C., Recent developments in photocatalytic water treatment technology: A review. Water research 2010, 44 (10), 2997-3027.

8. (a) Park, H. S.; Kim, D. H.; Kim, S. J.; Lee, K. S., The photocatalytic activity of 2.5 wt% Cu-doped TiO2 nano powders synthesized by mechanical alloying. J Alloy Compd 2006, 415 (1-2), 51-55; (b) Xu, Y. H.; Liang, D. H.; Liu, M. L.; Liu, D. Z., Preparation and characterization of Cu(2)O-TiO(2): Efficient photocatalytic degradation of methylene blue. Materials Research Bulletin 2008, 43 (12), 3474-3482; (c) Tseng, I. H.; Wu, J. C. S.; Chou, H. Y., Effects of sol-gel procedures on the photocatalysis of Cu/TiO2 in CO2 photoreduction. Journal of Catalysis 2004, 221 (2), 432-440.

9. Teleki, A.; Bjelobrk, N.; Pratsinis, S. E., Flame-made Nb- and Cu-doped TiO2 sensors for CO and ethanol. Sensors and Actuators B-Chemical 2008, 130 (1), 449-457.

10. (a) Li, Y.; Wang, W. N.; Zhan, Z. L.; Woo, M. H.; Wu, C. Y.; Biswas, P., Photocatalytic reduction of CO2 with H2O on mesoporous silica supported Cu/TiO2 catalysts. Applied Catalysis B-Environmental 2010, 100 (1-2), 386-392; (b) Sakata, Y.; Yamamoto, T.; Okazaki, T.; Imamura, H.; Tsuchiya, S., Generation of visible light response on the photocatalyst of a copper ion containing TiO2. Chemistry Letters 1998, (12), 1253-1254.

11. Helaili, N.; Bessekhouad, Y.; Bouguelia, A.; Trari, M., Visible light degradation of Orange II using xCu(y)O(z)/TiO2 heterojunctions. Journal of Hazardous Materials 2009, 168 (1), 484-492.

12. Choi, S. K.; Kim, S.; Lim, S. K.; Park, H., Photocatalytic Comparison of TiO2 Nanoparticles and Electrospun TiO2 Nanofibers: Effects of Mesoporosity and Interparticle Charge Transfer. Journal of Physical Chemistry C 2010, 114 (39), 16475-16480.

13. Pan, J. H.; Dou, H. Q.; Xiong, Z. G.; Xu, C.; Ma, J. Z.; Zhao, X. S., Porous photocatalysts for advanced water purifications. Journal of Materials Chemistry 2010, 20 (22), 4512-4528.

14. Wu, S. D.; Zhu, Y. Q.; Li, C.; Wei, Y. L., A Novel CuO-TiO2 Composite Photocatalyst and its Degradation of Methyl Orange under UV Irradiation. Advanced Materials Research 2011, 295, 1129-1132.

15. Nakata, K.; Liu, B.; Goto, Y.; Ochiai, T.; Sakai, M.; Sakai, H.; Murakami, T.; Abe, M.; Fujishima, A., Visible Light Responsive Electrospun TiO₂ Fibers Embedded with WO₃ Nanoparticles. Chemistry Letters 2011, 40 (10), 1161-1162.

16. Shiping Xu, Jiawei Ng, Xiwang Zhang, Hongwei Bai, Darren Delai Sun, Fabrication and comparison of highly efficient Cu incorporated TiO2 photocatalyst for hydrogen generation from water, international journey hydrogen energy, 35, 2010, 5 2 5 4e5 2 6 1

17. Lee, S. S.; Bai, H.; Liu, Z.; Sun, D. D., Novel-Structured Electrospun TiO< sub> 2</sub>/CuO Composite Nanofibers for High Efficient Photocatalytic Cogeneration of Clean Water and Energy from Dye Wastewater. Water research 2013.

18. Gross, P. A.; Pronkin, S. N.; Cottineau, T.; Keller, N.; Keller, V.; Savinova, E. R., Effect of deposition of Ag nanoparticles on photoelectrocatalytic activity of vertically aligned TiO2 nanotubes. Catalysis Today 2012, 189 (1), 93-100.

19. Qin Xu, Yu Zhao, Jin Zhong Xu, Jun-Jie Zhu, Preparation of functionalized copper nanoparticles and fabrication of a glucose sensor, Sensors and Actuators B 114, 2006, 379–386

20. Huang, J.; Zhu, J.; Cheng, K.; Xu, Y.; Cao, D.; Wang, G., Preparation of Co3O4 nanowires grown on nickel foam with superior electrochemical capacitance. Electrochimica Acta 2012, 75 (0), 273-278.

21. Macdonald, F.; Lide, D. R., CRC handbook of chemistry and physics: From paper to web. Abstr Pap Am Chem S 2003, 225, U552-U552.

22. Endut, Z.; Hamdi, M.; Basirun, W. J., Pseudocapacitive performance of vertical copper oxide nanoflakes. Thin Solid Films 2013, 528 (0), 213-216.

23. Nakayama, S.; Kimura, A.; Shibata, M.; Kuwabata, S.; Osakai, T., Voltammetric Characterization of Oxide Films Formed on Copper in Air. Journal of The Electrochemical Society 2001, 148 (11), B467-B472.

24. Burke, L. D.; Ahern, M. J. G.; Ryan, T. G., An Investigation of the Anodic Behavior of Copper and Its Anodically Produced Oxides in Aqueous Solutions of High pH. Journal of The Electrochemical Society 1990, 137 (2), 553-561.

25. Soci, C.; Zhang, A.; Xiang, B.; Dayeh, S. A.; Aplin, D. P. R.; Park, J.; Bao, X. Y.; Lo, Y. H.; Wang, D., ZnO Nanowire UV Photodetectors with High Internal Gain. Nano Letters 2007, 7 (4), 1003-1009.

26. Ohno, T.; Sarukawa, K.; Tokieda, K.; Matsumura, M., Morphology of a TiO2 Photocatalyst (Degussa, P-25) Consisting of Anatase and Rutile Crystalline Phases. *Journal of Catalysis* 2001, *203* (1), 82-86.

Supplementary Images

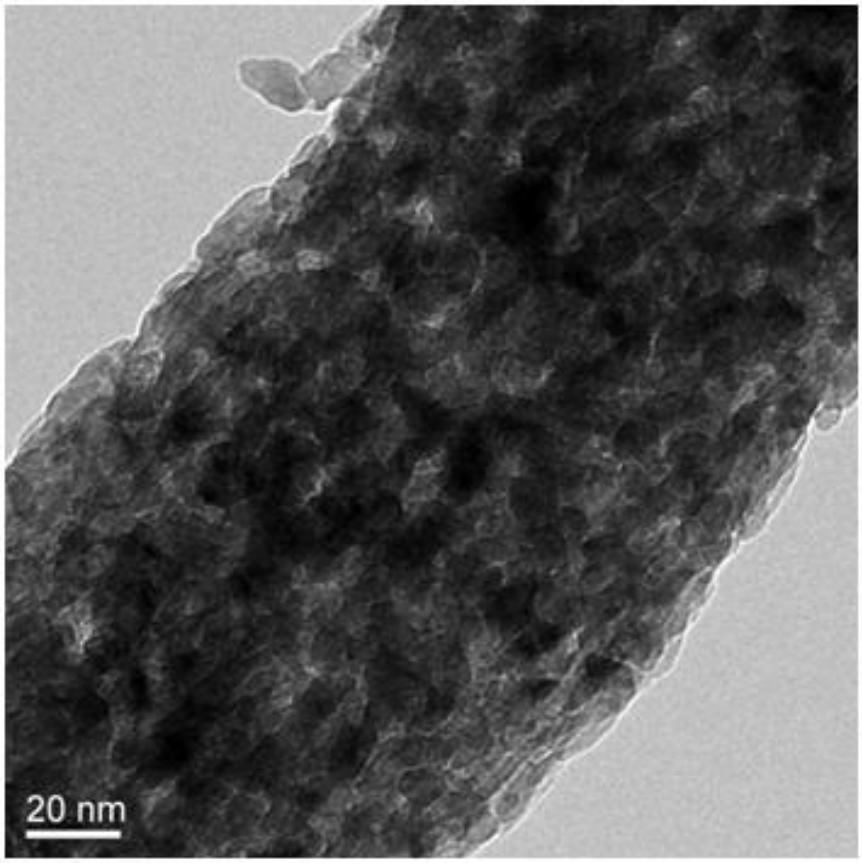

Figure S3.1 TEM image of electrospun pure TiO2 nanofiber annealed at 450 ^{o}C for 1h. TiO_2 nanoparticles, diameter in the range of 5-10 nm, are interconnected to form a fiber shape.

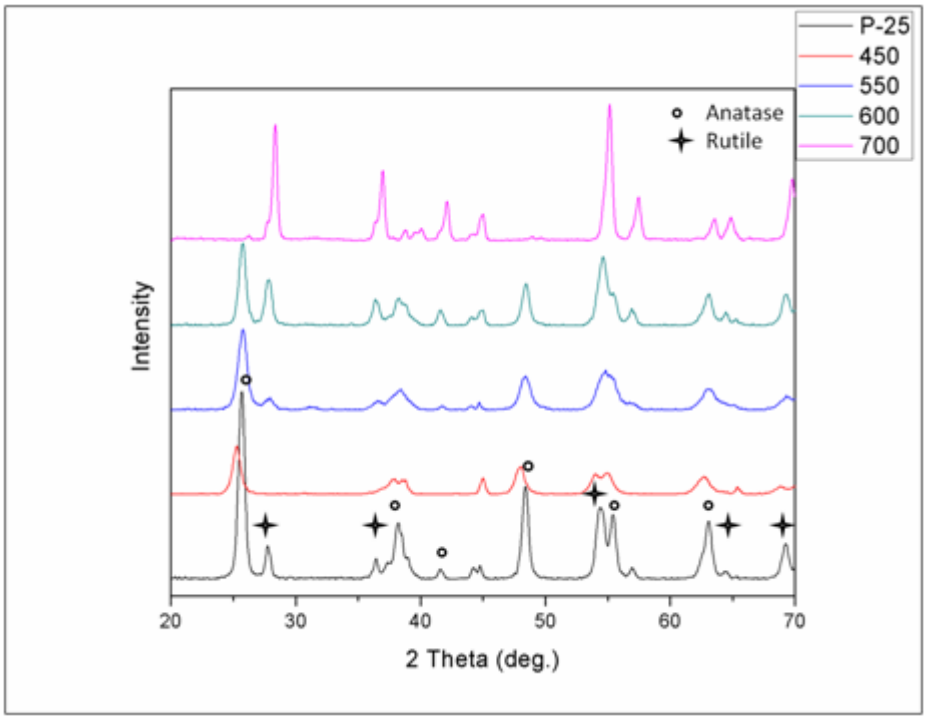

Figure S3.2 Results XRD analyses of CuO-TiO_2 nanofibrous mats annealed at different temperatures. As heating temperature increased, the phase of TiO_2 change from anatase to rutile phase. Since P-25 is one of the most efficient photocatalyst in industry, an optimized heating temperature of CuO-TiO_2 can be selected with respect to XRD pattern of P-25.

Chapter 4. Tailored Growth of 3D CuO Nanogrids

4.1. Introduction

Cupric oxide (CuO), as seen Figure 4.1, is a p-type semiconducting oxide with a monoclinic structure and an indirect band gap of 1.2eV, which has interesting electrochemical, photovoltaic and catalytic properties [1-3] Due to its versatile properties, CuO has been attracted a great deal of attention in important fields of science and technology such as heterogeneous catalysts[1], solar cell applications [3], gas sensors [4], magnetic storage media [5], and lithium ion electrode materials [6] etc. With decrease on the crystal size and high surface area, shorter ion diffusion, and electrochemical activity, nanosized CuO structures offers highly reactive surfaces, and prominent optical, electrical, catalytic properties.[7] In addition, a close relation between bandgap energies of CuO nanostructures and their shapes and sizes in developing various synthesis methods [8,9].

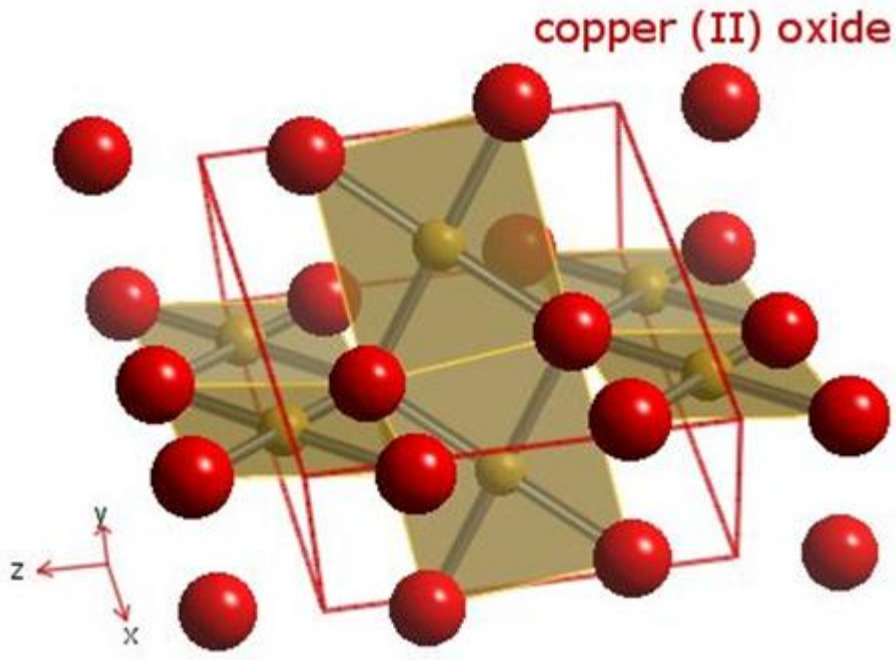

Figure 4.1 Schematic of CuO crystal structure.

A variety of CuO nanostructures including, nanoneedles, nanoribbons, nanowires, nanorods and nanosheet, have been fabricated by pulsed laser deposition, electrospinning, so-gel technique, and thermal oxidation, which was employed in this study [10-19]. For 3D CuO structure , Liu and Zeng synthesized 'dandelion-like' 3D CuO microspheres by hydrothermal synthesis method mixing copper nitrate $Cu(NO_3)_2 \cdot 3H_2O$ in ethanol solvent, followed by addition of NaOH, $NaNO_3$, and ammonia in Teflon-lined stainless steel autoclave at 100℃ for 24-36h [10]. Zhang et al. also fabricated 3D hierarchical CuO butterfly-like structures in a solution of cupric chloride ($CuCl_2 \cdot 2H_2O$) and NaOH at 100 ℃ for 15 h by using sodium dodecyl benzenesulfonate (SDBS) as surfactant[11]. However, to our knowledge, there have been no reports on the preparation of 3D CuO nanogrids.

4.2. Novel synthesis of cuo nanogrids

It was previously reported that copper clusters can nucleate the growth of copper nanostructures in carbon nanotubes by diffusing through them [20]. With this knowledge, it was hypothesized that the organic nanofibers onto the surface of copper substrate with heat treatment could result in Cu filling nanofibers. In the present work, we investigate the direct oxidation and growth of 3D CuO nanogrids from Cu filled nanofibers which were produced by the thermal interaction of copper mesh with a mat of polyvinylpyrrolidone (PVP) nanofibers prepared by electrospinning and act as templates guiding the growth of the 3D nanopaticle oxide networks. This unique CuO nanostructure, in comparison to CuO nanowires, would serve as continuous and self-supported nanostructures with higher porosity and surface area and extensive open networks ideal for 3D nanobattery electrode, noble catalyst and p-type chemosensors.

The synthesis of 3D CuO nanogrids was carried out by thermal oxidation of copper mesh substrates on which PVP mats were deposited by electrospinning. In a typical procedure, PVP (*Sigma*-Aldrich, M_w=1,300,000) was mixed with ethanol solvent. After mixing the solutions by ultrasonication, it was filled into a syringe with a needle made of stainless steel. The needle was connected to a high-voltage supply and positioned vertically 7 cm above a piece of aluminum foil grounding electrode. Upon applying a high voltage of 18kV, a solution jet was ejected from the needle tip. The solvent evaporated and web of fibers deposited on a Cu mesh (TWP Inc., 200 mesh, wire dia. 51μm) placed on the aluminum foil. The Cu mesh was first cleaned with ethyl

alcohol then rinsed with deionized water followed by ultrasonic bath in acetone. The syringe pump was programmed to dispense 5ml of 8% PVP solution at a flow rate of 30µl/min.

Thermal oxidation of PVP deposited Cu substrate was carried out in a resistively heated furnace at a constant rate of 11^{o}C/min to the oxidation temperature from 200 to 600^{o}C and held for 2 to 5 hours then cooled to ambient temperature. The sample temperatures were monitored by placing a thermocouple in vicinity of the samples.

The morphologies and dimensions of the samples were studied using a scanning electron microscopy (SEM) and high-resolution transmission electron microscopy (HRTEM). HRTEM and energy dispersive spectroscopy (EDS) were used in the analysis of diffusion characteristics and the chemical characterization of the samples. The optical absorption spectra of samples were recorded using UV-Visible spectrometer in the wavelength range, 250 -1000 nm at room temperature.

4.3. Results and Discussion

4.3.1. Morphology Aanalysis

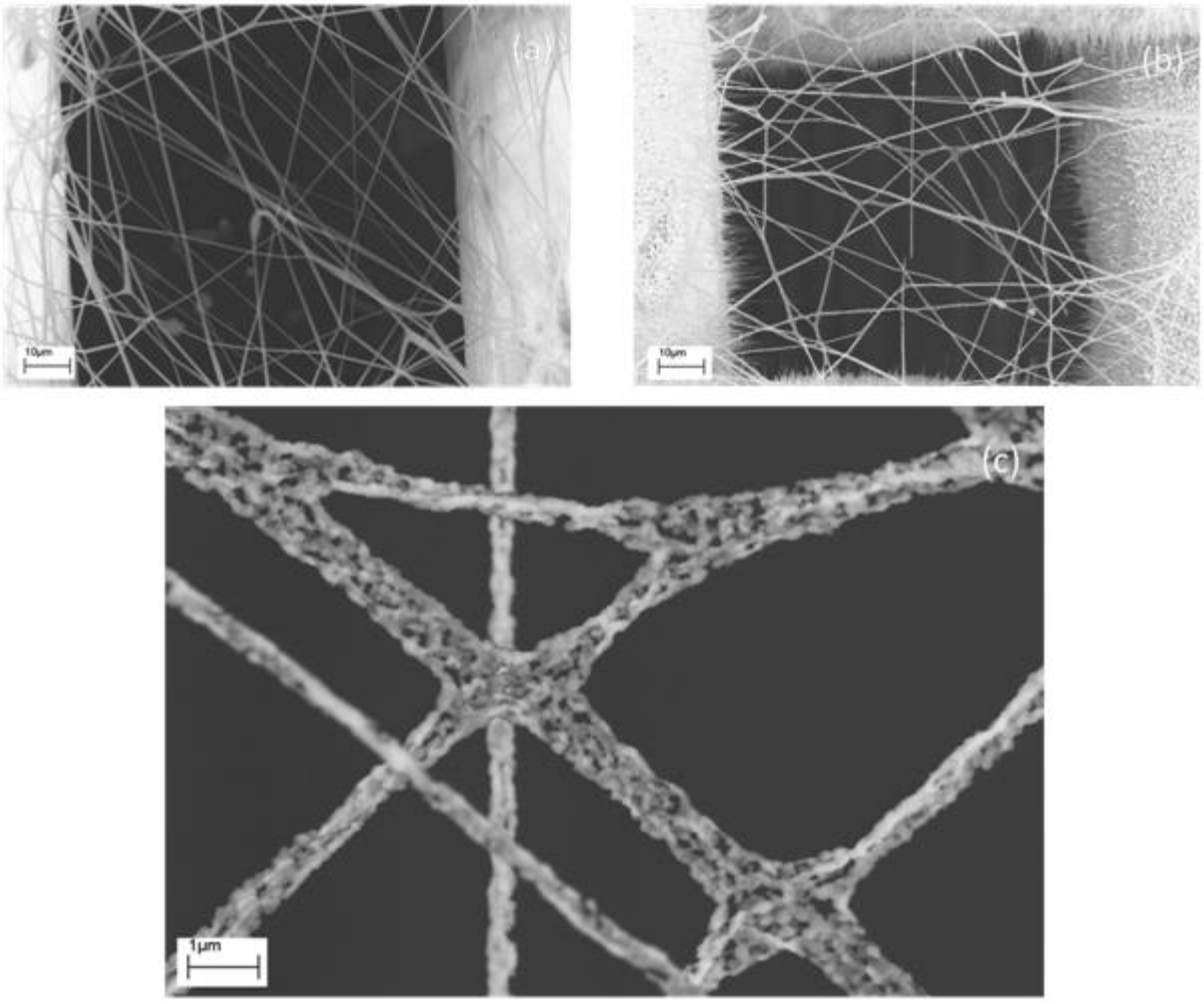

Figure 4.2 (a) SEM image of PVP nanofibers deposited on the Cu mesh substrate by electrospinning (b) Low magnification and (c) high magnification of SEM image of synthesized composite substrate thermal oxidation at 500^{o}C for 4 h.

Figure 4.2 (a) shows the SEM micrographs of the nanofibers onto Cu mesh by electrospinning of PVP polymer solution. The smooth nanofibers have random orientation and diameters ranging 0.40 to 0.80 μm. The morphology of 3D nanogrids structure as-prepared by thermal oxidation at 500^{o}C for 4 hours is shown in Figure 4.2(b), (c). The diameter of the primary 3D nanogrids are measured from the magnified image (Figure 4.2(c)) as 0.30-0.98 μm.

During the thermal oxidation process, the PVP was selectively incinerate then the CuO 3D nanogrids remained.

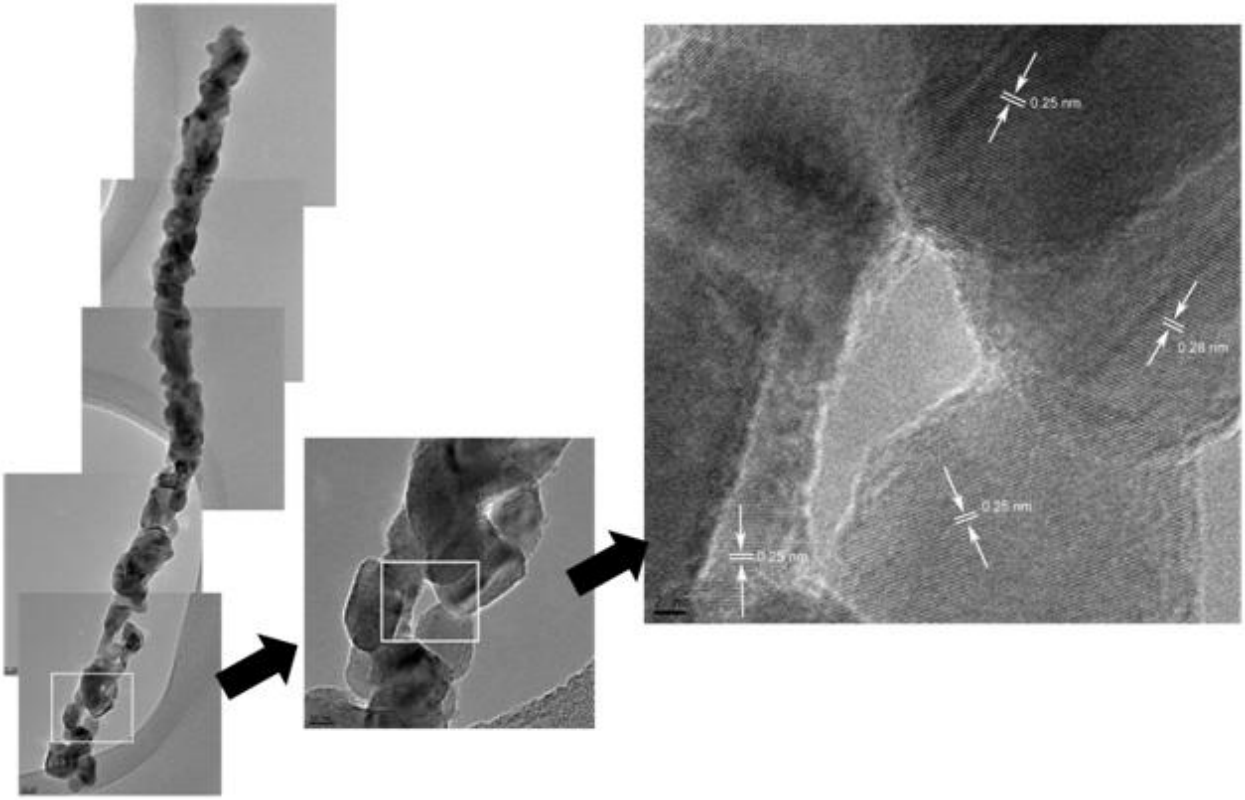

Figure 4.3 HRTEM image of 3D nanogrids oxidized at 400˚C for 2h in air.

HRTEM was further used to characterize the morphology and crystallinity of 3D nanostructure. HRTEM images (see Figure 5.3) of 3D nanogrids heated in air at 400 ˚C and held for 2 hours show numerous primary nanocrystals, size ranged from 16 to 60 nm, interconnected to each other to form larger secondary 3D nanogrids with high porosity. Clearly, the CuO nanostructures composed of networks of continuous, self-supported, and 3-dimentional particles, crystals and nanorods, providing increased surface area, porosity, and extensive open networks. Figure 4.3 shows the interplanar spacing for each nanocrystals which forms 3D nanogrids. These spacing are 0.25 and 0.28 nm corresponding to the distance of the CuO (-111) and CuO (110), respectively.

To get a better understanding of the growth mechanism of 3D nanogrids, the reaction products were captured and analyzed different formation stage.

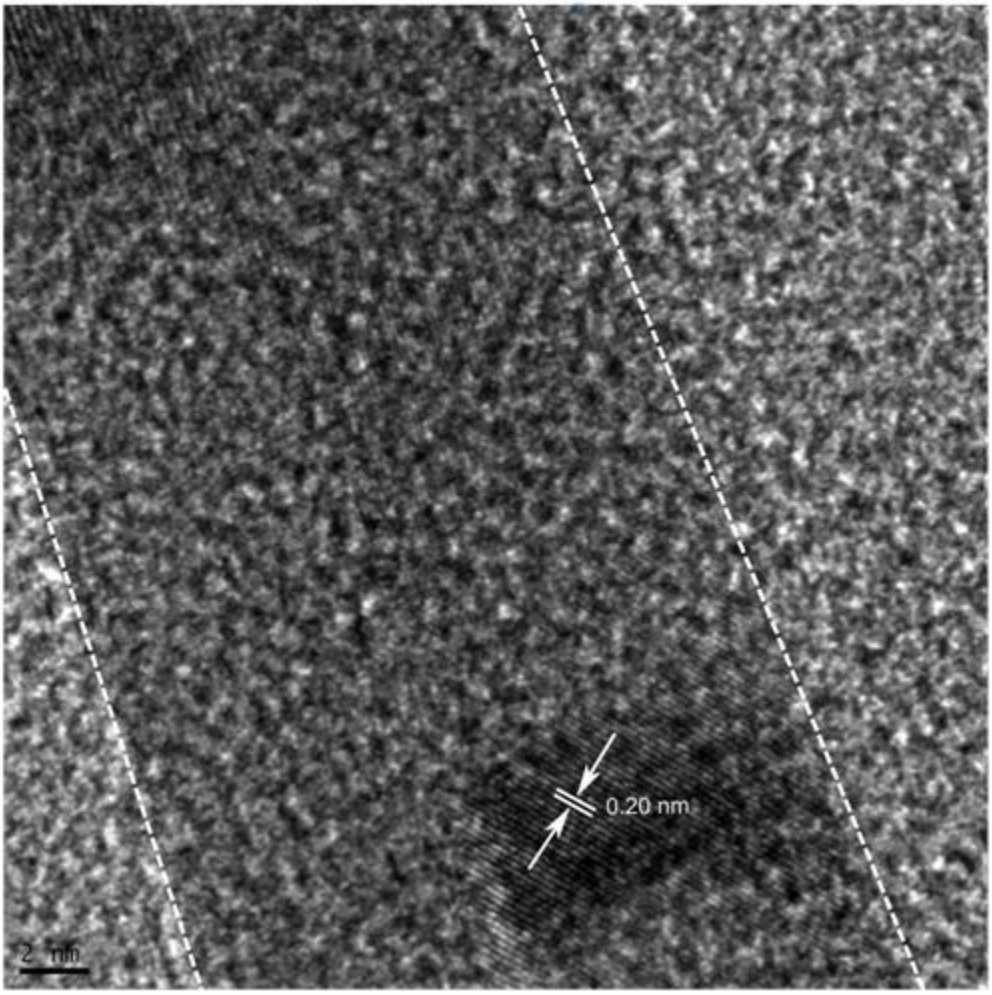

Figure 4.4 HRTEM image of Cu filled PVP nanofiber. The white dash lines highlight the interface between Cu and PVP nanofiber.

Figure 4.4 is HRTEM image of PVP nanofibers heat treated at 400 ˚C and held for 2h. From this picture, the Cu atoms particles shiftly migrate the PVP nanofibers axis and even form a wire strucuture.[20] The interplanar spacing of some of these inner structure, 0.20nm, is corresponding to Cu (111).

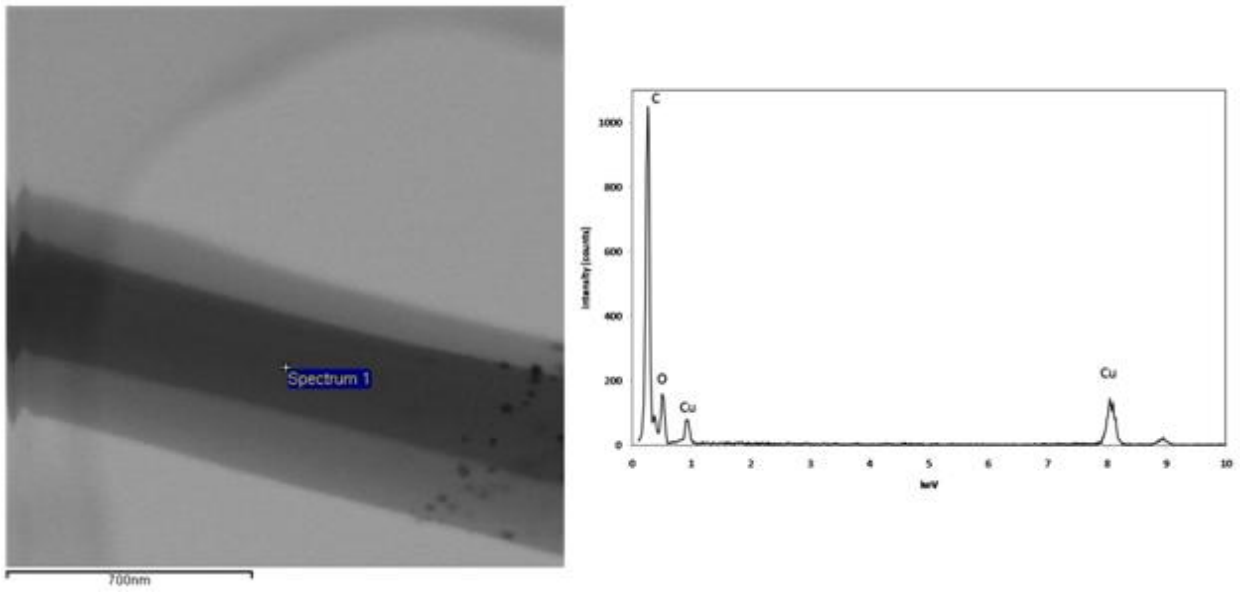

Figure 4.5 HRTEM image and EDS spectra of the as-prepared copper filled nanofiber heated at 200˚C for 2h. The "+" on the image shows the location of the spectra collected.

The energy dispersive spectrum (EDS) further confirms that formation of Cu filling polymer fibers. At the early formation stage of the reaction product, as-prepared copper filled nanofiber heated at 200˚C for 2h of EDS analysis were carried out at positions where the core of the fibers, as shown in figure 4.5.

4.3.2. Thermal analysis

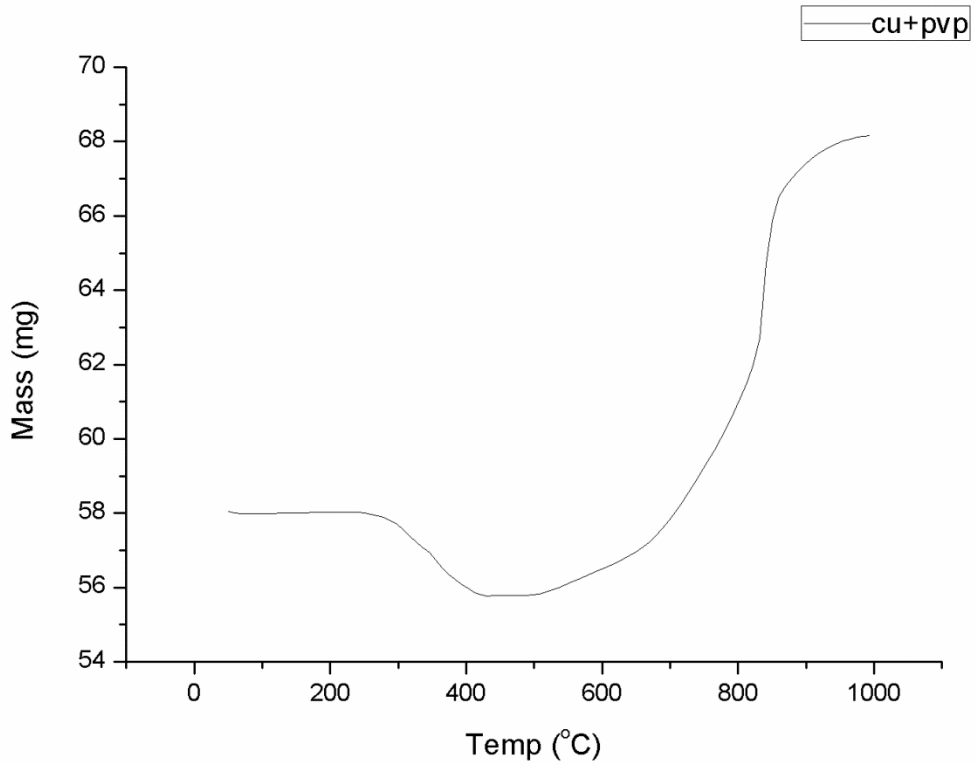

Figure 4.6 TGA test results of PVP electrospun fiber mats deposited copper mesh.

As seen in TGA curve, Figure 4.6, PVP fibrous mats started to decrease due to PVP calcination at 260C°. The curve seemed no obvious temperature change between 400 C° to 500 C°. The mass start to increase from 500 C° might be due to the phase transition Cu → Cu2O → CuO [23].

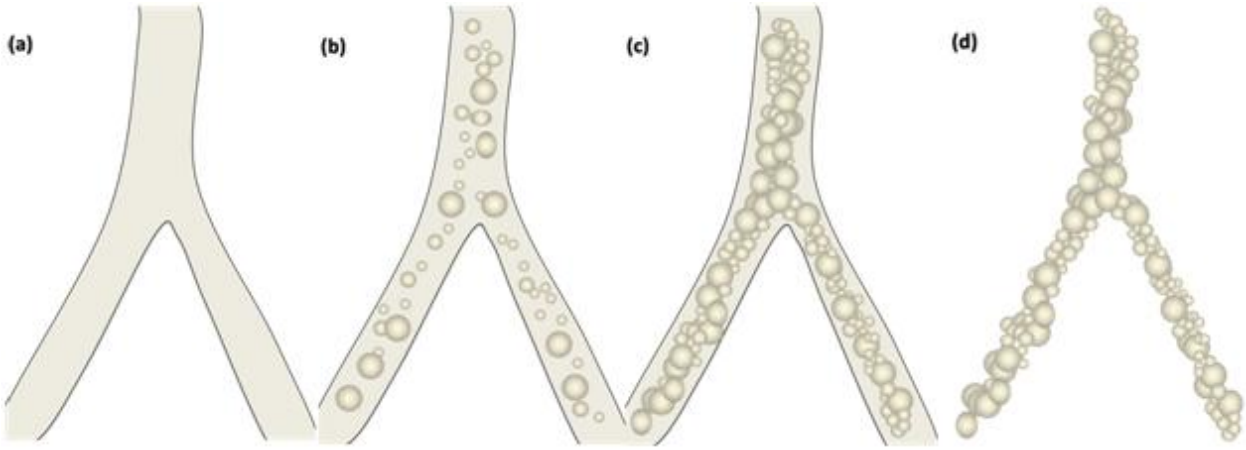

Figure 4.7 A schematic illustration of the formation of CuO 3D nanogrids. a) PVP mats deposit on Cu mesh by electrospinning; b) Cu particles diffuse and migrate through PVP nanofibers; c) Diffused Cu particles entangles; and d) after the thermal oxidation, polymers removed and 3D CuO nanogrids remain.

These EDS spectra clearly indicate that the copper element diffusion and migration occurred during the thermal oxidation because the Cu element detected in the fibers.

On the basis of combined SEM, HRTEM and EDS analysis, the growth mechanism of CuO nanogrids occur the migration and diffusion of Cu substrate through the polymer fiber templates that CuO is formed upon further oxidation. (Figure 4.7) This 3D nanogrids growth mechanism could also be applicable to other metal oxide by creating geometric constraints for constructional units.

4.3.3. Spectroscopic Analysis

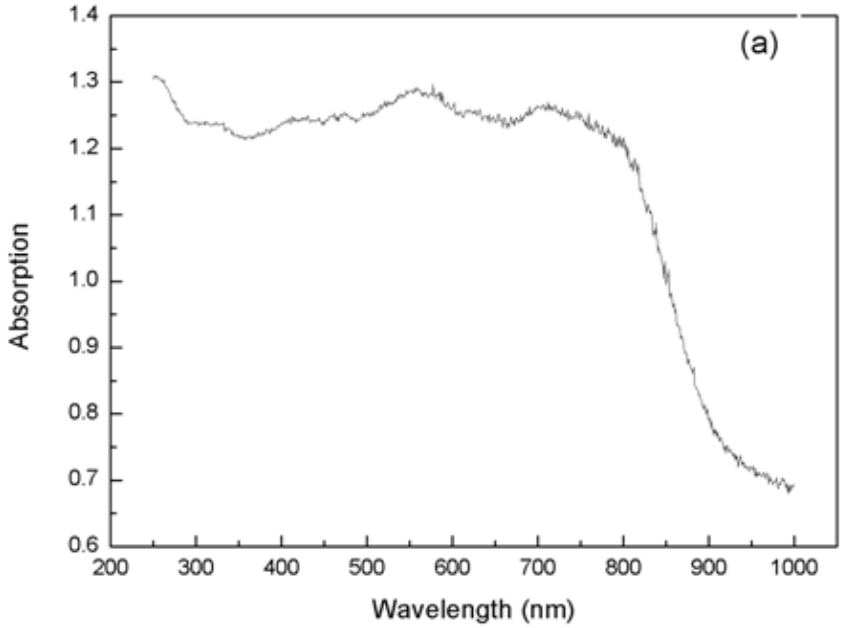

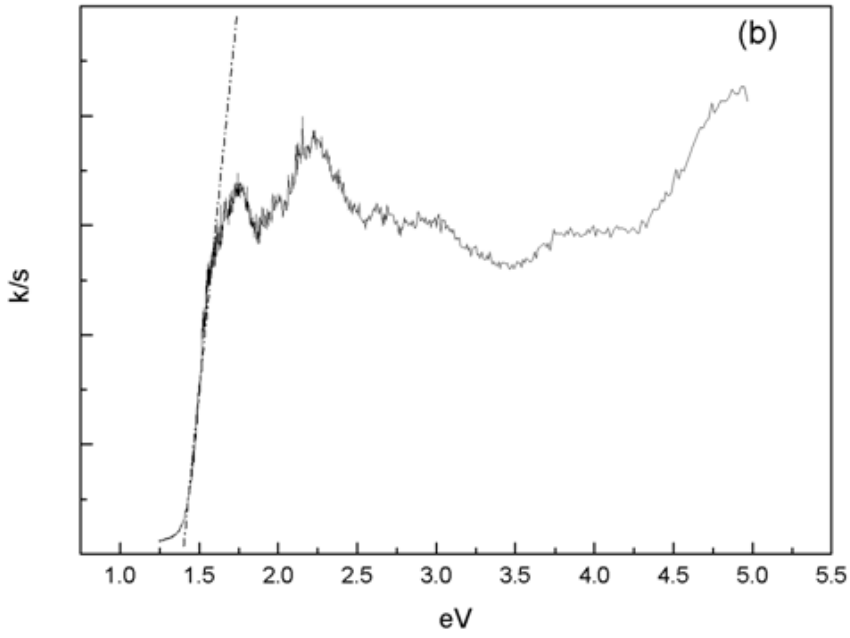

Figure 5.8 (a) UV-vis absortion spectrum of the 3D CuO nanogrids. (b) The corresponding $(\alpha hv)^2$ vs. E_{phot} curve, indicating that the band gap is 1.33 eV.

UV-Visible spectrum of CuO 3D nanogrids is presented in figure 5.8(a), which shows the shoulder near 809 nm. The optical bandgap energy is estimated using the Kubelka-Munk function,

$$F(R) = (1- R)^2 /2R = k/s , \quad (3.1)$$

where R is the reflectance, k absorption coefficient, and S scattering coefficient, respectively. [21] The figure 5.8(b) shows a plot of (k/s) spectrum vs. photon energy derived from Kubelka-Munk function. The extrapolated value of photon energy at k/s=0 indicates an bandgap energy (E_g)= 1.33eV. The calculated band gap is slightly larger than the previous reported value for bulk CuO(E_g= 1.2eV)[1].

4.4. Summary

In brief, 3D CuO nanogrids were synthesized by direct thermal oxidation of composite substrates consisting of a Cu mesh and PVP nanofibers deposited on it by electrospinning. It results from the templating action of electrospun nanomats of polymers deposited on Cu mesh.

The average diameter of the CuO grains is 23 to 60 nm and the diameter of the primary 3D nanogrids are 0.30-0.98 μm. The estimated band gap energy is ~1.33eV, which is larger than reported value for bulk CuO (E_g= 1.2eV). CuO anode for lithium battery test showed stable capacity around 680 $mAhg^{-1}$ (See Appendix 1). Considering its easy preparation procedure and novel, self-supported CuO nanostructures in an open 3D configuration formed continuous networks of extreme surface area may be used in 3D nanobattery electrode, noble catalyst and p-type chemo sensors.

Reference

[1] Switzer, J. A.; Kothari, H. M.; Poizot, P.; Nakanishi, S.; Bohannan, E. W., *Nature* **2003,** *425* (6957), 490-493.

[2] Nagase, K.; Zheng, Y.; Kodama, Y.; Kakuta, J., *J. Catal.* **1999,** *187* (1), 123-130.

[3] E. Barrera-Calva, J. M.-V., M. Ortega-López, L. Huerta-Arcos, J. Morales-Corona, and R. Olayo-González, *Res. Lett. Mater. Sci.* **2008,** *2008*, 5.

[4] Zhang, J. T.; Liu, J. F.; Peng, Q.; Wang, X.; Li, Y. D. *Chem. Mater.***2006**, *18*, 867.

[5] Kumar, R. V.; Diamant, Y.; Gedanken, A. *Chem. Mater.***2000**, *12*, 2301.

[6] Wu, H.; Lin, D.; Pan, W., *Appl. Phys. Lett.* **2006,** *89* (13), 133125-3.

[7] Hong, Z.-s.; Cao, Y.; Deng, J.-f., *Mater. Lett.* **2002,** *52* (1-2), 34-38.

[8] Hong-Mei Xiao; Shao-Yun Fu; Lu-Ping Zhu; Yuan-Qing Li; Guo Yang, *Eur. J. Inorg. Chem.* **2007,** *2007* (14), 1966-1971.

[9] S. Anandan, S. H. Yang, *J. Experi. Nanosci.* **2007**, *2*, 23–56.

[10] Wang, S. Q.; Zhang, J. Y.; Chen, C. H., *Scr. Mater.* **2007,** *57* (4), 337-340.

[11] Yajing Zhang; Siu Wing Or; Xiaolei Wang; Tieyu Cui; Weibin Cui; Ying Zhang; Zhidong Zhang, *Eur. J. Inorg. Chem.* **2009,** *2009* (1), 168-173.

[12] Guan, H.; Shao, C.; Chen, B.; Gong, J.; Yang, X., *Inorg. Chem. Commun.* **2003,** *6* (11), 1409-1411.

[13] Qian, W.; Wei, F.; Liu, T.; Wang, Z. W., *Solid State Commun.* **2003,** *126* (7), 365-367.

[14] Chen, A.; Long, H.; Li, X.; Li, Y.; Yang, G.; Lu, P., *Vacuum* **2009,** *83* (6), 927-930.

[15] Liu, Y. L.; Liao, L.; Li, J. C.; Pan, C. X., *J. Phys. Chem. C* **2007,** *111* (13), 5050-5056.

[16] Jiang, X.; Herricks, T.; Xia, Y., *Nano Lett.* **2002,** *2* (12), 1333-1338.

[17] Kumar, A.; Srivastava, A. K.; Tiwari, P.; Nandedkar, R. V., *J. Phys.: Condens. Matter.* **2004,** *16* (47), 8531-8543.

[18] Xu, J. F.; Ji, W.; Shen, Z. X.; Tang, S. H.; Ye, X. R.; Jia, D. Z.; Xin, X. Q., *J. Solid State Chem.* **1999,** *147* (2), 516-519.

[19] Han, S.; Chen, H.-Y.; Chu, Y.-B.; Shih, H. C, *J. Vac. Sci. Technol, B: Microelectron Nanomet.* **2005,** *23* (6), 2557-2560.

[20] Hwang, H. J.; Kwon, O. K.; Kang, J. W., *Solid State Commun.* **2004,** *129* (11), 687-690.

[21] Yamashita, N. N. *J. Phys. Soc. Jpn.* **1973** 35 1089.

[22] Xiang, J. Y., Tu, J. P., Huang, X. H., & Yang, Y. Z. (2007). A comparison of anodically grown CuO nanotube film and Cu2O film as anodes for lithium ion batteries. *Journal of Solid State Electrochemistry*, *12*(7-8), 941-945. doi:10.1007/s10008-007-0422-1

[23] Zhu, Y. , Mimura, K. , Isshiki, M., Oxidation Mechanism of Cu_2O to CuO at 600–1050°C, Oxidation of Metals, October 2004, Volume 62, Issue 3-4, pp 207-222

[24] Poizot, P.; Laruelle, S.; Grugeon, S.; Dupont, L.; Tarascon, J. M. Nature 2000, 407, 496−499.

Chapter 5. Synthesis of $CuWO_4$ / CuO photocatalyst and its application of photodegradation of organic hydrocarbons in water

5.1. Introduction

The recent disaster in the Gulf of Mexico, caused by the explosion and sinking of an oil rig, has resulted in a 600 miles wide spill of 9 million gallons of medium crude oil across the surface of the ocean, threatening to reach the shoreline [1]. Oil derivatives are amongst the most dangerous compounds for the environment, due to their long degradation time and ease of migration in aquatic settings [2, 3]. Immediate measures are required to contain and clean the spill preventing it from reaching the shore and from causing further destruction to the environment and to the wildlife in the Mexican Gulf. Efforts towards this goal include collecting part of the oil spill by large vessels (skimmers) by means of mechanical collection and sorption or use of dispersants (scattering), at high cost and with the threat of secondary pollution[3]. Even so, there are still large amounts of this oily water remaining [1], and this needs to be remediated rapidly, in a straightforward and economic manner. Among several a natural constituent of crude oil, benzene is known as one of the most basic petrochemicals.

Due to its high toxicity, confirmed carcinogenicity, benzene is regarded as a priority hazardous substance for which efficient treatment technologies are needed, but it is a great challenge due to the stable aromatic benzene structure, especially at ambient conditions [4].

Advanced oxidation process has been a promising area of research in the recent years, for it has shown great potential in liquid hydrocarbon remediation [5]. Titanium dioxide (TiO_2) is predominantly featured in this field due to its cost effectiveness and inert nature and photostability [6]. However, it is well known that TiO_2 only reacts with UV spectrum which is 4% of whole spectrum in the sunlight [7]. Consequently, utilizing visible spectrum is the key feature of next generation photocatalyst.

WO_3 is a visible-light responsive n-type photocatalyst for oxygen generation [8]. However, pure WO_3 exhibit poor light energy conversion efficiency compare to TiO_2 due to the relatively low reduction potential [9]. $CuWO_4$ is another possible metal oxide photocatalyst which utilize longer light wavelength (band gap: 2.30eV) with high photostability in neutral pH [10]. In addition, $CuWO_4$ was reported high energy Cu(3d) orbital near the top if its valance

band which is relatively higher than to the O(2p) orbitals characteristic of the d^0 WO_3 [11]. Several research efforts have been focused on surface and interface modification, surface sensitization, transition/noble metal doping, etc. Among the several strategies, compositing noble metal (Pt) showed an improvement in electro-oxidation of methanol and CO [12]. However, using Pd and Pt as co-catalysts cost too much which is not suitable for large scale industrial applications. Instead, cupric oxide (CuO) has been considered as an economical and efficient alternative co-catalysts studied WO_3-CuO composite [13]. Cupric oxide (CuO) is a p-type semiconducting oxide with a monoclinic crystal structure.

This chapter explores synthesis and characterization of $CuWO_4$-CuO nanocrystalline photocatalysts as a visible-light-activated photocatalysts. The unique morphology with large surface area and high crystallinity was achieved by sol-gel ceramic synthesis. Further morphology and phase studies have conducted using SEM, TEM and XRD. Photocatalytic activity was performed in UV and visible light with methylene blue dye and benzene in aqueous environment. In addition photoelectrochemical properties also studied from cyclic voltammetry and chronoamperometry results.

5.2. Experimental Procedure/Methods

Four main divisions of catalysts were synthesized for this project. All the chemicals were used as received without further purification.

5.2.1. I. $CuWO_4$-CuO synthesis without Copper grid as a template.

(a) A 15 ml of 9 % w/v PVP (Polyvinylpyrrolidone, M_W~1,300,000, Sigma-Aldrich) in ethanol solution was added to 5.74 x 10^{-3} mol W-iso (5% w/v in isopropanol tungsten isopropoxide, Alfa Aesar) with 0.2 ml water. This was done in a nitrogen environment. 3.1 x 10^{-3} mol of $3H_2O$• $CuNO_3$ (Sigma-Aldrich) and 3.3 ml of water was then added to the above solution and ultrasonicated for 2 hours till a one phase solution was seen. This solution was electrospun keeping the following working parameters: Voltage: 19 kV; Working Distance: 13 cm; Flow rate: 0.045 ml/min; Needle size: 22 gauge. Once the fibers were electrospun, they were peeled off from the collector and heat treated in a tube furnace. The temperature of the furnace

was programmed to work so it raises its temperature from 25^0C to 400^0C in 1 hour and stay at 400^0C for 1 hour, after which it comes down to room temperature in about an hour.

(b) Mixing Tungsten Isopropoxide 5.74 x 10^{-3} mol W-Iso + 0.2 ml water and 3.1 x 10^{-3} mol of CuNO3 + 0.5 ml water were then added into ultrasonicated for 2 hours or till a one phase solution was seen. The prepared solution then heat treated in a tube furnace. The temperature of the furnace was programmed to work so it raises its temperature from 25^0C to 400^0C in 1 hour and stay at 400^0C for 1 hour, after which it comes down to room temperature in about an hour.

5.2.2. II. $CuWO_3$-CuO synthesis with Copper Grids.

A 15 ml of 9 % w/v PVP solution containing 1.3g of PVP and 15ml Ethanol was added to 3.1 x 10^{-3} mol of W-Iso and 0.2ml water. This was done in a nitrogen environment. This solution was ultrasonicated for 1hour. After ultrasonicating, the solution was immediately poured into syringes for electrospinning. The collector plate was covered with Copper grid, so the electrospun fibers were deposited on the copper mesh (TWP Inc., 200 mesh, wire dia. 51 μm). This solution was electrospun keeping the following working parameters: Voltage: 19kV; Working Distance: 13 cm; Flow rate: 0.045 ml/min; Needle size: 22 gauge.Once all the solution was electrospun, the electrospun fibers along with the copper mesh were then kept in the furnace for annealing. The temperature of the furnace was programmed to work so it raises its temperature from 25 ^{0}C to 400 ^{0}C in 1 hour and stays at 400 ^{0}C for 1 hour after which it comes down to room temperature in about an hour. The copper diffusion mechanism and nanogrids formation were explained in previous study[14] .

5.2.3. III. $CuWO_3$-CuO synthesis

Nanostructured powder type catalysts were prepared with 3.1 x 10^{-3} mol of W-iso, 0.2 ml water, and commercial 0.1g copper (II) oxide (Sigma-Aldrich). The prepared solution then heat treated in tube furnace. The temperature of the furnace was programmed to work so it raises its temperature from 25 ^{0}C to 400 ^{0}C in 1 hour and stays at 400 ^{0}C for 1 hour after which it comes down to room temperature in about an hour..

5.2.4. IV. Synthesized nanostructured WO_3

a) A 15 ml of 9 % w/v of PVP with Ethanol was add to 3.1 x 10^{-3} mol of W-iso, 0.2ml water, 1.5m acetic acid and 1.5 ethanol then ultrasonicated for 2 hours or till a one phase solution was seen.This solution was electrospun keeping the following working parameters: Voltage: 19kV; Working Distance: 13cm; Flowrate: 0.045ml/min; Needle size: 22 gauge. Once all the solution was electrospun, the electrospun fibers were then kept in the furnace for annealing. The temperature of the furnace was programmed to work so it raises its temperature from 25^0C to 400^0C in 1 hour and stays at 400^0C for 1 hour after which it comes down to room temperature in about an hour.

b) A 15 ml of 9 % w/v of PVP with ethanol was add to 33.1 x 10^{-3} mol of W-iso, 0.2ml water, 1.5m acetic acid, and 1.5 ethanol then ultrasonicated for 2 hours or till a one phase solution was seen.This solution poured in ceramic tray and kept in the furnace for annealing. The temperature of the furnace was programmed to work so it raises its temperature from 25^0C to 400^0C in 1 hour and stays at 400^0C for 1 hour after which it comes down to room temperature in about an hour.

5.2.5. Photocatalytic degradation of benzene on synthesized photocatalysts

Once all the catalysts produced through I, II, and III processes, they were tested for photocatalytic activity by adding into a system of benzene and water. In order to identify a visible change in the amount of benzene, Unisol AS dye (Sigma-Aldrich) was added to benzene which gave it a blue color. 0.5 mg of Unisol was added to 20 ml benzene making up it a concentration of 250 ppm. The benzene-water system consisted of (10 ml water + 0.5 ml benzene), 0.01 g of the catalyst was added to this system and the set up was kept near the window to check for the photocatalytic activity with natural sunlight. In the case of II catalyst, as-revived $1cm^2$ of the oxidized copper grid template which had the synthesized catalysts was added to the benzene-water system. Selected test results were sent out to American Analytic Laboratories LLC. (Farmingdale, NY) for GC-MS (*Gas chromatography–mass spectrometry*) analysis.

5.2.6. Photocatalytic degradation of methylene blue on synthesized photocatalysts

In a typical experiment, 0.018g of the catalysts was added to a 4ml Methylene Blue (MB) dye solution of 50 ppm concentration in distilled water. This was kept in the dark for 1 hour to obtain an adsorption-desorption equilibrium. A light source with a 300 W Xenon light bulb (Newport) with AM 1.5 was used as the source for whole spectra and visible light by using a 400 nm cut-on filter in the same set up. The solution was then kept under the UV or visible light for 3 hours. Every 1 hour 2ml of the solution was taken out to measure its absorbance value with the spectrophotometer and it was poured back after the measurements. The degradation of methylene blue was evaluated by studying the changes in the absorbance value at a wavelength of 665nm using UV/Vis spectrophotometer (HR 4000, Ocean Optic) with halogen and deuterium as light sources.

5.2.7. Photoelectrochemical characterization

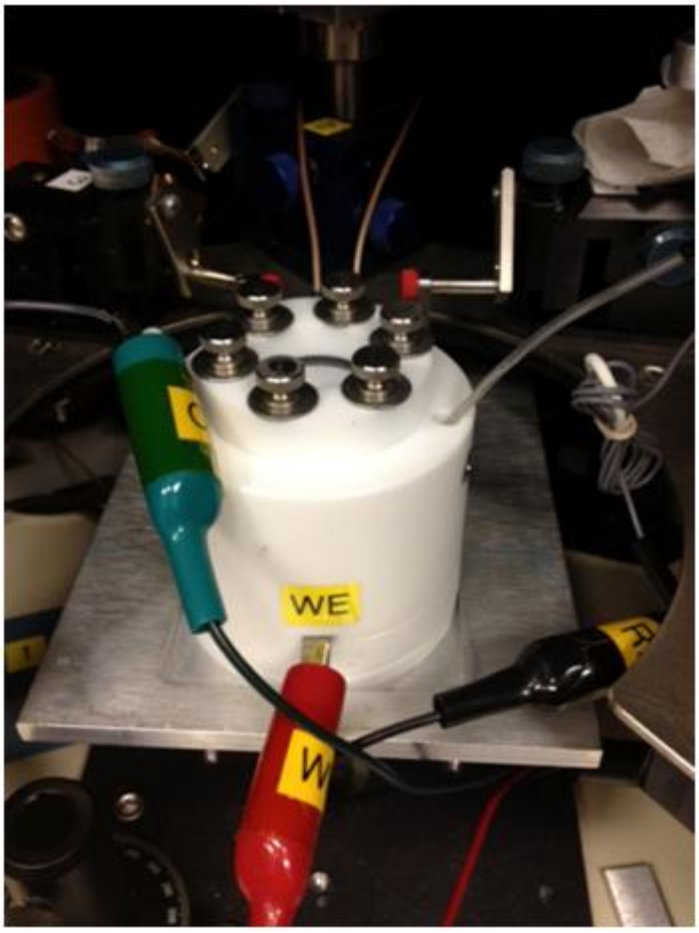

Figure 5.1 Image of three electrodes cell with quartz window equipped.

- Reference electrode: Ag/AgCl (World Precision Instruments Inc.)
- Counter electrode: Pt (Platinum wire, BASi)
- Working electrode : Synthesized catalysts deposited on ITO glass (Indium tin oxide)
- Electrolyte: 0.1M benzoic acid/0.1M KOH

Photo-electrochemical measurements were carried out in a three-electrode, single-compartment glass cell fitted with a quartz window (see Figure 5.1). Working electrodes were prepared by mixing synthesized catalysts with 0.1mM PVP in isopropanol alcohol and drop casting onto ITO glass substrate to form a thin film. The synthesized catalysts deposited on ITO glass were annealed at 400^{o}C in air for 2 hours. The electrolyte used was a 0.1M benzoic acid/0.1M KOH

solution. The working electrode was placed at the optical path. A potentiostat (Princeton Applied Research) was employed for the measurement. The illumination source was a 150 W Xenon lamp equipped with an AM1.5G filter and 400nm cut-off filter to simulated solar radiation and for visible spectrum of light intensity of 113.0 mW/cm^{2}on working electrode.

5.3. Result and discussion

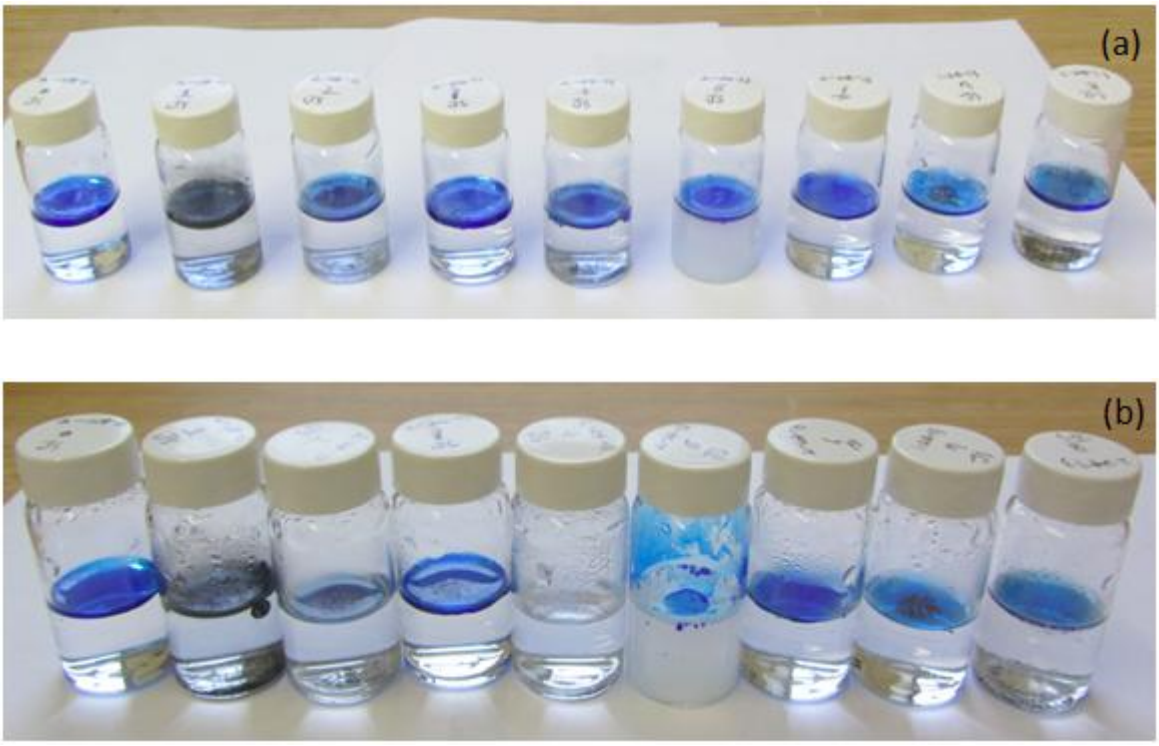

Figure 5.2 Natural light testing of 8 catalysts using the same solution of water(10ml) + dyed benzene(1 ml) (concentration of 87,650 ppm) ((a): Day 1 and (b): Day 9). Note that water in the fifth vial from the left is totally clear at Day 9.

A total of 9 vials were prepared for preliminary photocatalytic degradation of benzene testing:

0. No Catalyst
1. Catalyst I(a)
2. Catalyst II with Cu Mesh
3. Commercial WO_3 powder
4. Catalyst III $CuWO_3$-CuO synthesis

5. Commercial TiO_2 (Degussa P25)
6. Catalyst I(b)
7. Catalyst IV(a)
8. Catalyst IV(b)

As seen in Figure 5.2, the 5th vial from the left (catalyst III) showed that the blue layer of benzene removed after 9 days of natural sunlight illumination which was faster than 6th vial (Commercial TiO_2 (Degussa P25)). Since photocatalytic benzene degradation is photo-induced reaction with exothermal ($\Delta G<0$, down-hill) process, the final products of this reaction are CO_2 + H_2O + etc (other by product)[3]. Day 9 picture shows (see Figure 5.2) condensed water on the surface of vials which give evidence of benzene degradation from photocatalytic results. Further analysis may need that the 3rd vial (Catalyst II with Cu Mesh) also showed high rate of benzene removal.

To confirm the repeatability of the photocatalytic degradation of benzene in natural light, 0.01g of catalyst III was added into water (10ml) + dyed benzene (0.5ml) (Concentration 43,825 ppm) contained three vials.

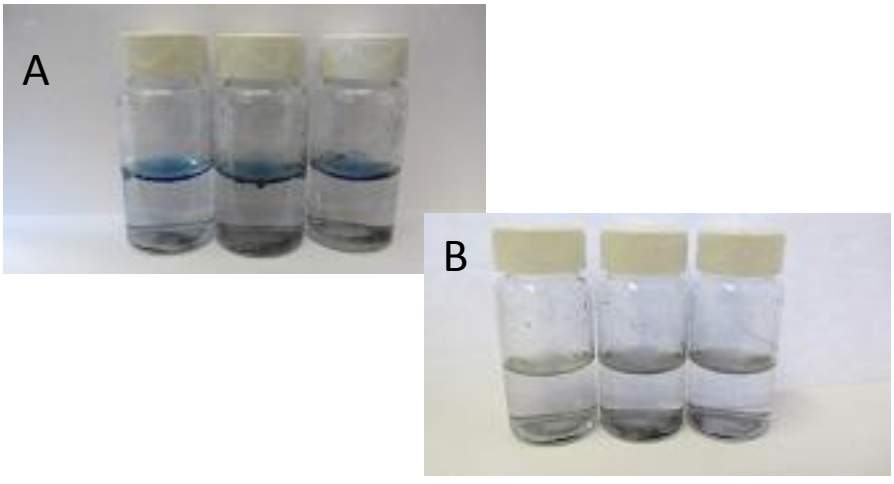

C

Certificate of Results

Analyses	Sample Result	LOD	LOQ	Qual	Units
VOLATILES BTEX BY 8260	Sample 3-3-13 4		SW8260C		
Benzene	2800	2.5	20		µg/L

Figure 5.3 Before (a) and after (b) photocatalytic activity test under natural sunlight for 3 days with (c) GC-MS results.

The repeatability test result showed that top benzene layer removed within 3 days. The clear solution was further analyzed in GC-MS testing. The benzene concentration from repeatability testing under natural sunlight showed that the level changed from 43,825 to 2.8 ppm (see Figure 5.3). It is worth to note that all the vials were closed cap for the testing therefore with enough air flow in may give better photocatalytic activity.

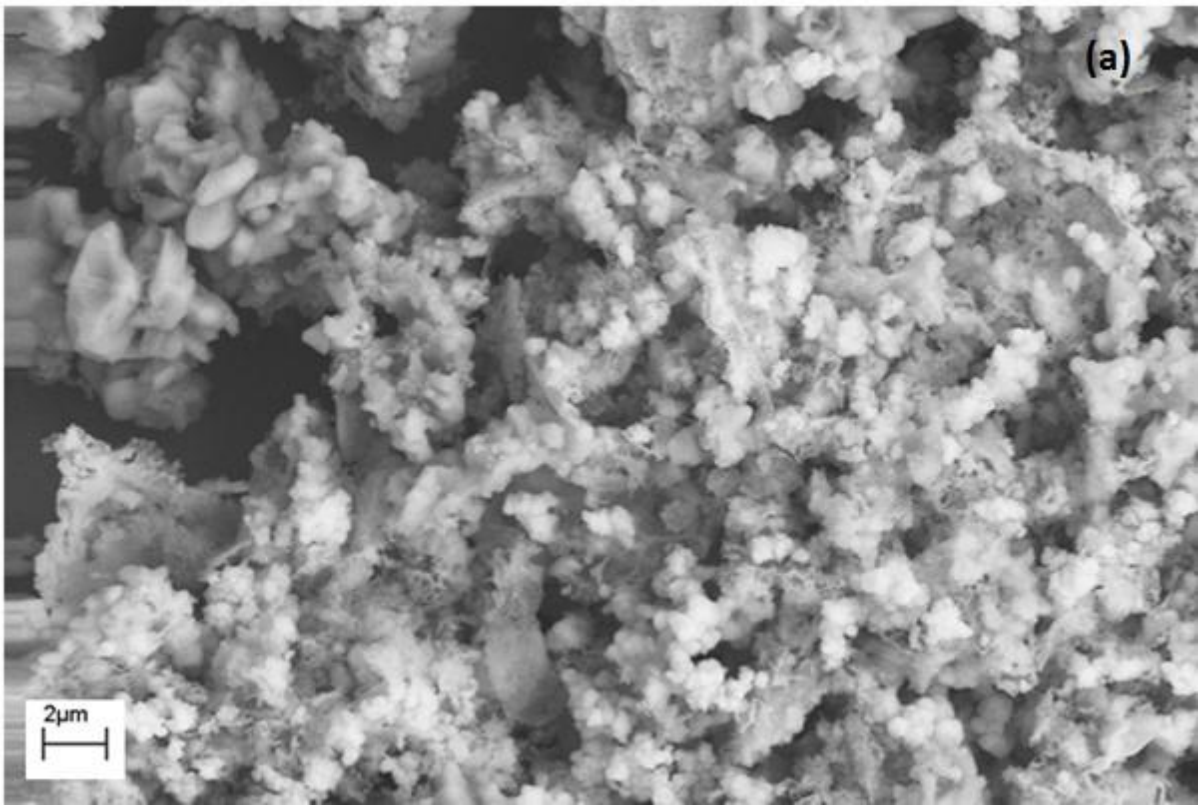

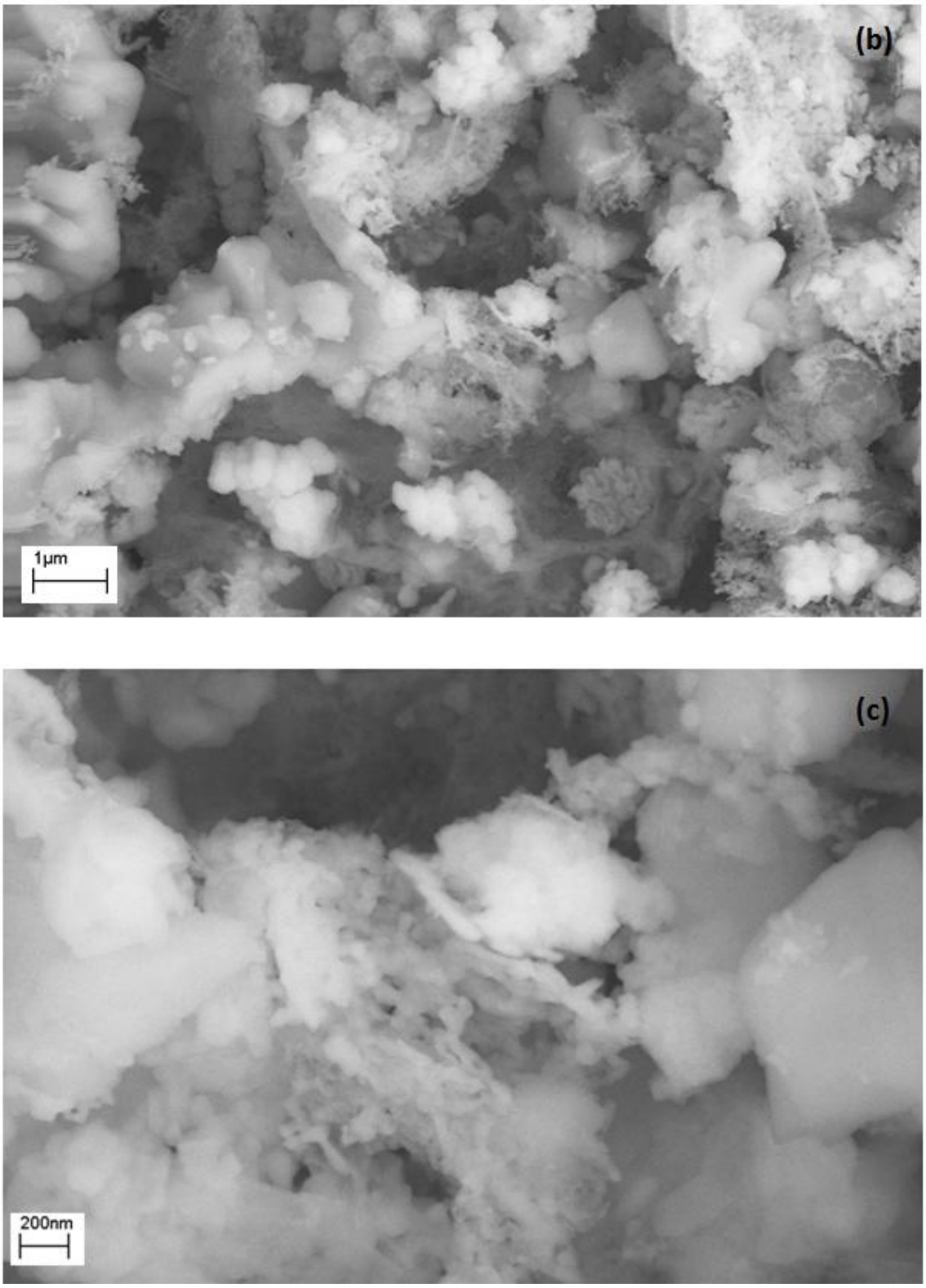

Figure 5.4 SEM micrographs of catalyst III heat treated 400^0C for 1h.

SEM micrographs of catalyst III are shown in Figure 5.4. SEM micrographs show that the two types of nano-sized particles interconnected each other. Smooth surface particles, diameter 100-800nm, showed darker than irregular shaped grid type particles, diameter 20-80nm. It is assumed that smooth surface particles are lighter elements (CuO) and irregular nanogrids particles considered heavier elements ($CuWO_4$).

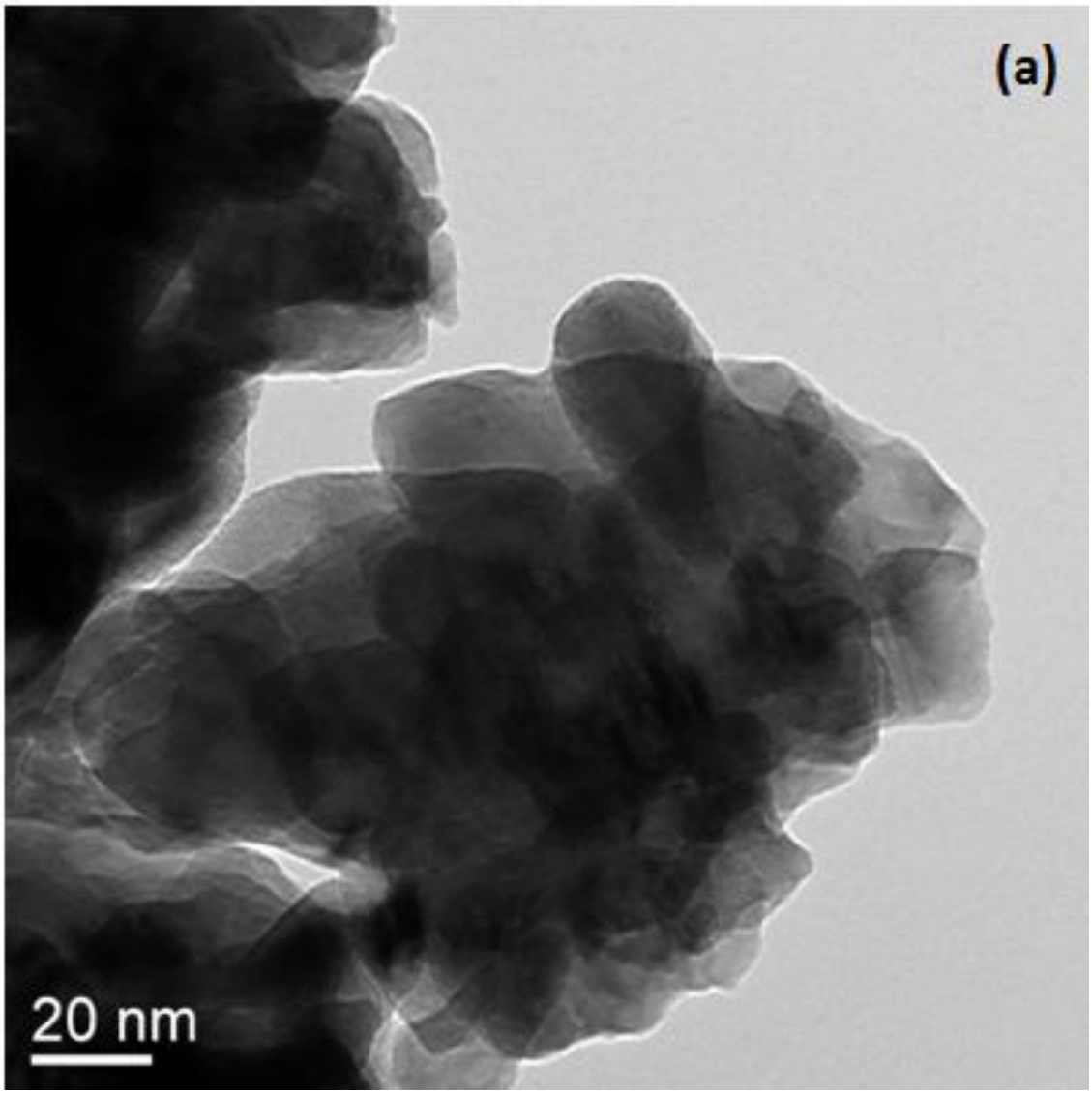

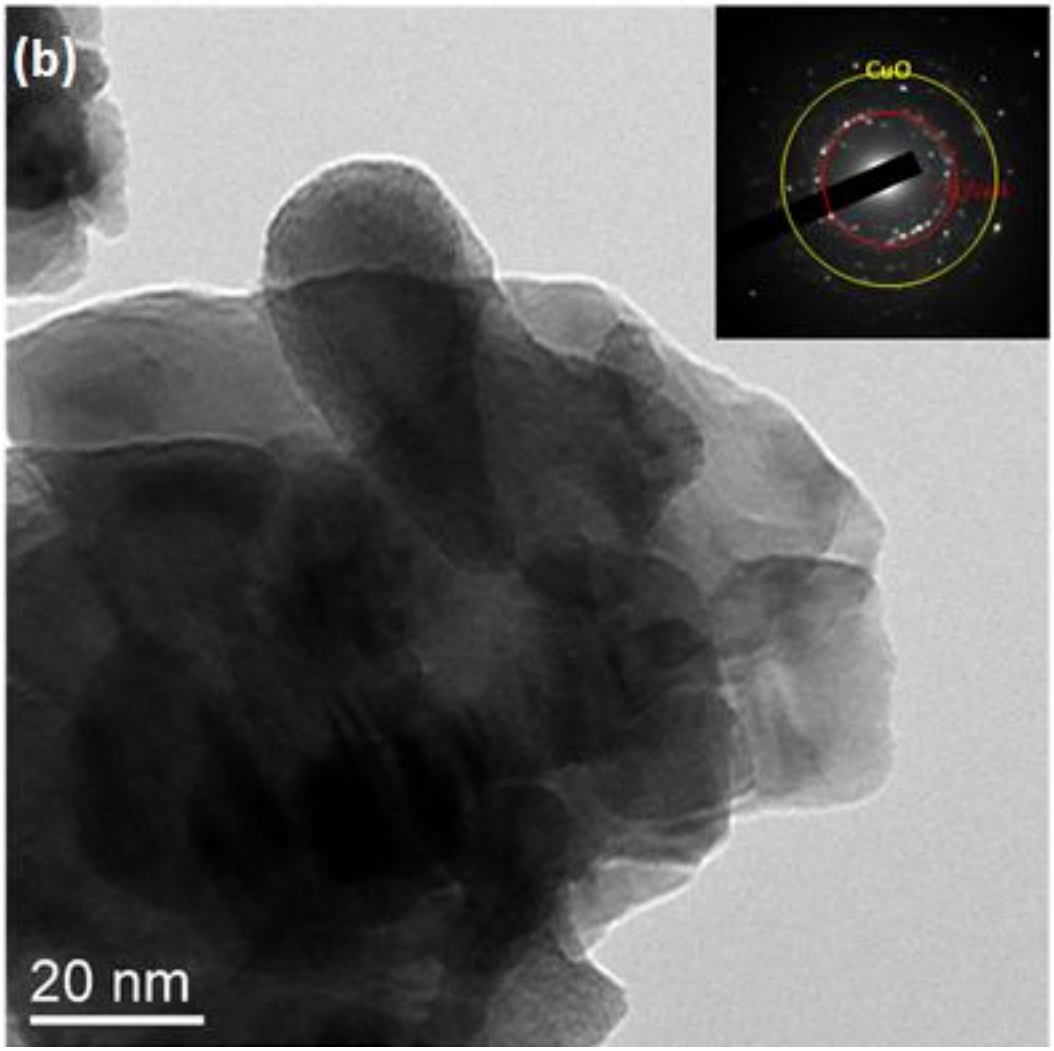

Figure 5.5 TEM micrographs of catalyst III heat treated 400^0C for 1h (inset: SAED image).

The TEM micrographs of $CuWO_4$ –CuO composite particles are shown in Figure 5.5. Inset of SAED on TEM image (see figure 4.6(b)) shows diffraction pattern match with $CuWO_4$ (002) and CuO(002).

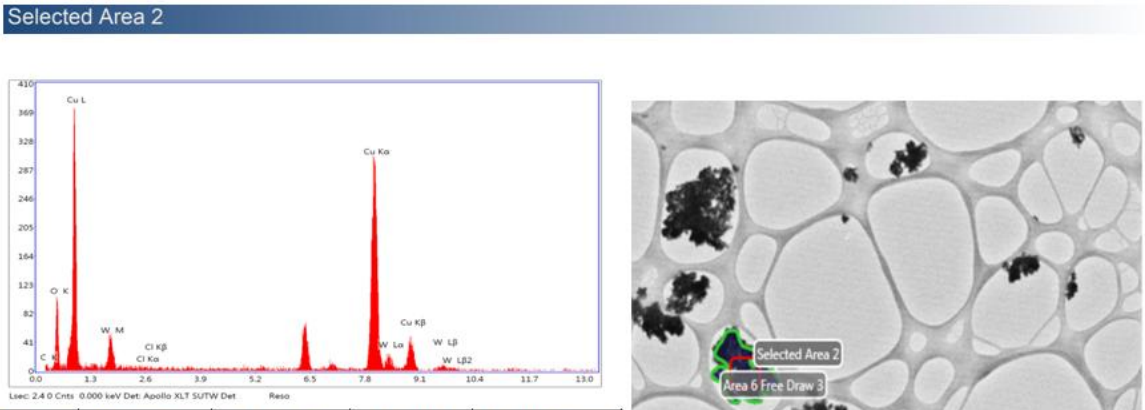

Element	Weight %	Atomic %	Net Int.	Net Int. Error
C K	0.85	3.86	27.95	0.17
O K	7.24	24.55	337.61	0.04
Cl K	0.27	0.41	21.64	0.47
Cu K	78.91	67.41	1989.71	0.02
W L	12.73	3.76	151.09	0.19

Figure 5.6 EDX(Energy-dispersive X-ray) result of selected area.

EDX analysis result (see Figure 5.6) shows the both qualitative and quantitative information about elemental and atomic percentage between $CuWO_4$ and CuO, respectively. The quantitative analysis of $CuWO_4$-CuO showed about 3.76% of W was present, consisting with amount of mixed W atom. The high Cu ratio may also contribute from the supporting copper grid.

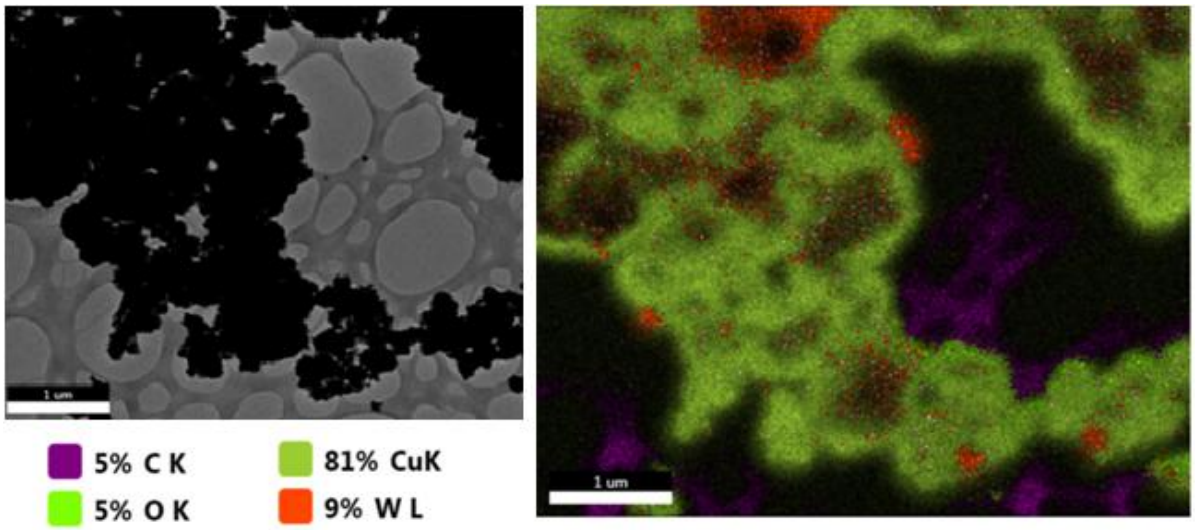

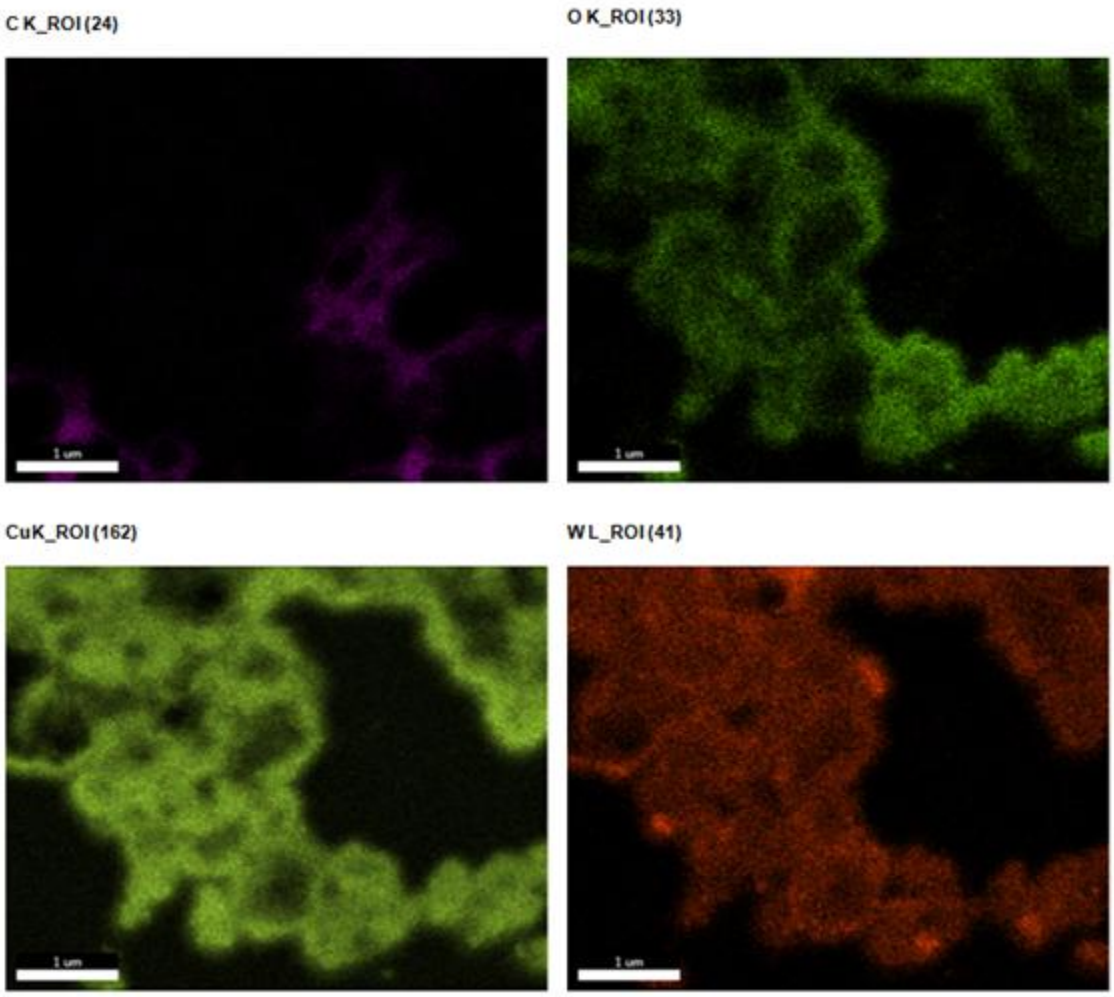

Figure 5.7 EDX element mapping result of $CuWO_4$-CuO nanoparticles.

It could be clearly seen from element mapping that the element of Cu, O, and W truly existed in the sample. The element mapping of C is shown because C exited in the support film of the TEM grid. As color distribution indicated Cu and O elements were uniformly spread over the particles whereas, W elements aggregated in certain areas.

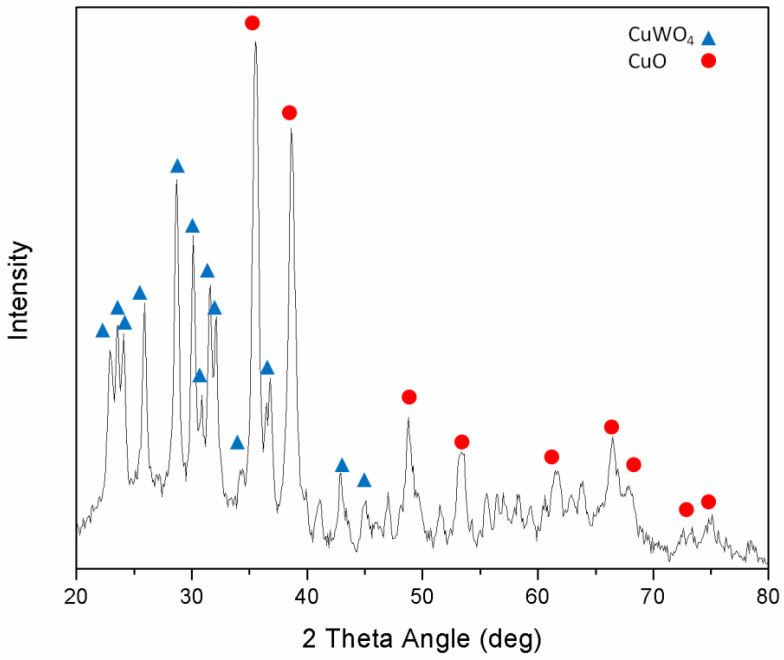

Figure 5.8 XRD (X-Ray Diffraction) pattern of $CuWO_4$-CuO nanocatalysts.

The degree of crystallinity and crystal structure of the synthesized $CuWO_4$-CuO were studied by XRD. XRD measurements (see Figure 5.8) confirmed the presence of $CuWO_4$ (JCPDS 21-307)-CuO (JCPDS45-937) corresponding to SAED analysis from Figure 5.6, respectively. The grain size calculated using the Scherrer equation were found that 80 nm, respectively[15].

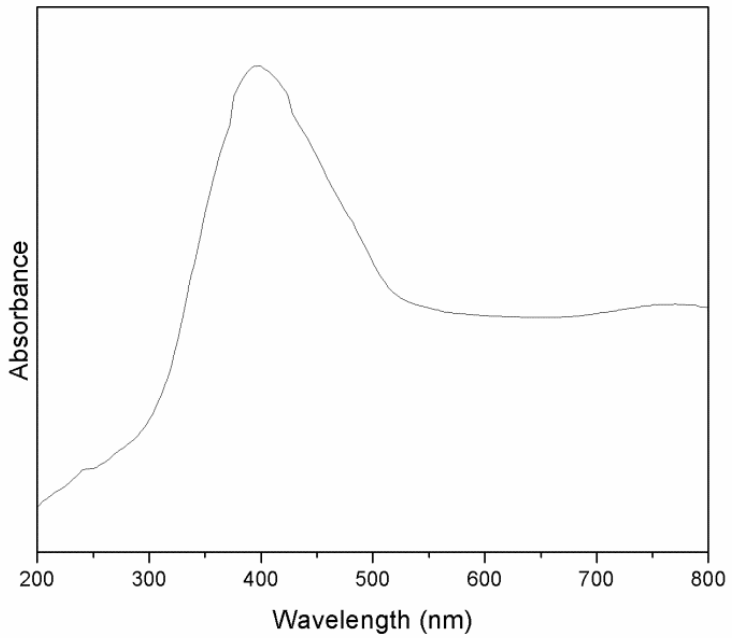

Figure 5.9 Uv-Vis diffuse reflectance spectrum of $CuWO_4$-CuO nanocatalysts.

Figure 5.9 shows the UV-visible absorption spectrum of the $CuWO_4$-CuO nanocatalyst annealed 400 ^{0}C for 1 h. The spectra clearly showed that intense absorption in the 350 to 500 nm. The onset of absorption of $CuWO_4$ was at ~520nm, which corresponds to the band gap energy 2.38 eV. This value is consist with previous reports (E^{CuWO4}_{BG} =2.3~2.4eV) [10, 16] Addition of CuO may extend relative high absorption rate in visible light range as well.

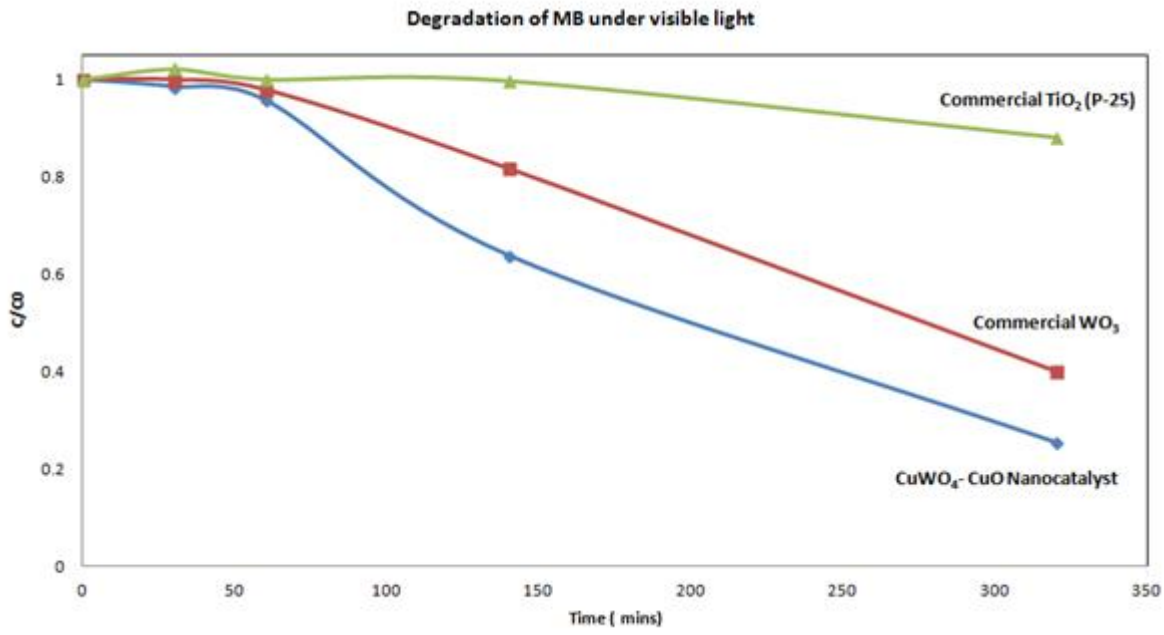

Figure 5.10 Photocatalytic activity results of oxide catalysts on methlyene blue under visible light.

It is important that a photocatalyst responds under visible light, since the natural sunlight consists of 47% of visible light, and only 4% of UV light.Therefore, $CuWO_4$-CuO nanocatalysts was tested, and along with it commercial titanium dioxide and commercial tungsten dioxide were also tested for the degradation of methylene blue solution, under visible light. Figure 5.10 shows photocatalytic degradation of Methylene Blue by using three catalysts, synthesized $CuWO_4$-CuO nanocatalysts, commercials WO_3, commercial TiO_2 (P25). Five hours of test results show that the $CuWO_4$-CuO degraded more than 80% which is faster that commercial TiO2.

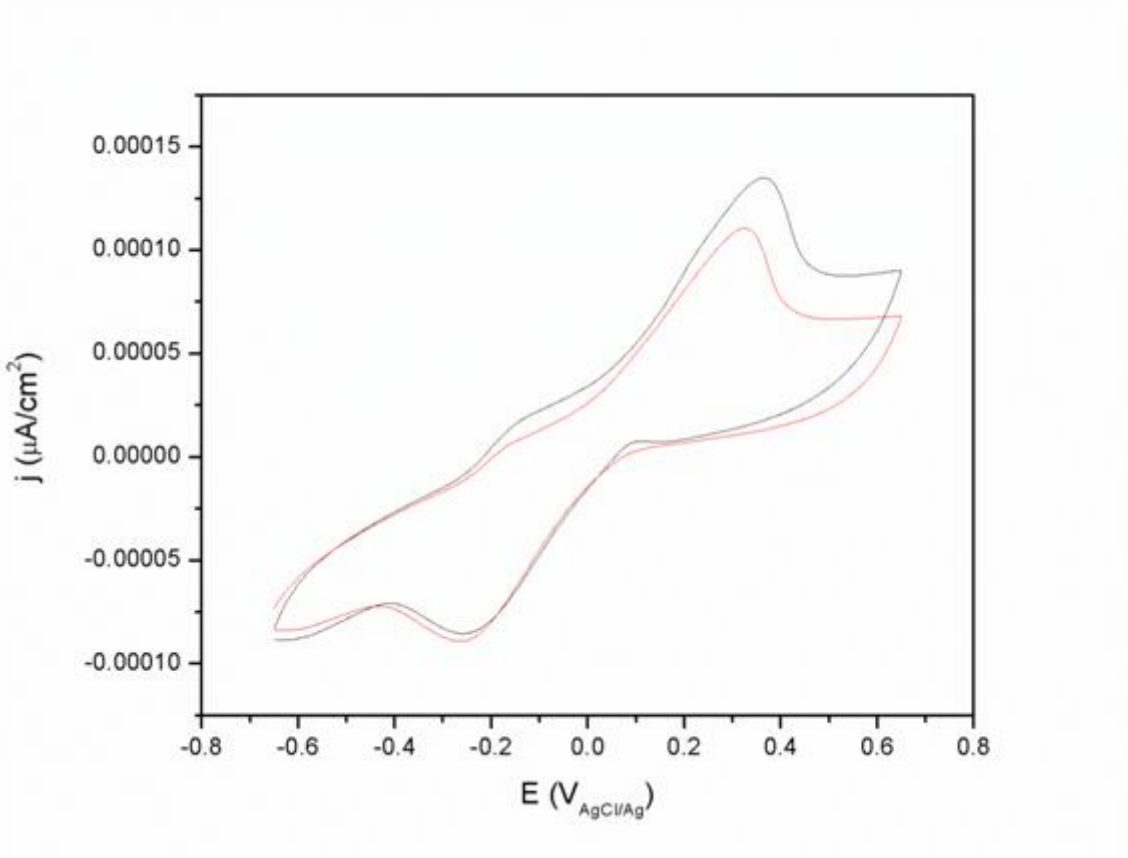

Figure 5.11 Current-potential curves of $CuWO_4$-CuO nanocatalysts electrode in 0.1M benzoic acid and 0.1M KOH in nitrogen-saturated water. A 150-W Xe lamp was light source (1)Blue-Catalyst III in the light and (2) Red- Catalyst III in the dark with scan rate 20mV/s.

The current-potential (i-V) behavior of a $CuWO_4$-CuO nanocatalysts in an aqueous solution containing 0.1M benzoic acid and 0.1M KOH in nitrogen-saturated water as the supporting electrolyte is shown in Figure 5.11. As the potential sweeps to the positive direction from -.65V to .65V vs Ag/AgCl, $CuWO_4$-CuO nanocartalyst show peaks potential E_{pa}= -0.25 V and E_{pc}= 0.33 V in N_2-purged cell [10]. Zheng et al.[17] showed the conversion of p-type to n-type behavior at +0.33 V vs Ag/AgCl of $CuWO_4$(p-type)/ CuO(n-type). The reduction peak at E_{pa}= -0.25 V may correspond to the one-electron CE mechanism of benzoic acid reduction where chemical dissociation of the acid preceeds the electron –transfer step [18, 19]:

$$C_6H_5COOH \underset{k_1}{\overset{k_{-1}}{\rightleftharpoons}} C_6H_5COO^- + H^+$$

$$H^+ + e^- \xrightarrow{ks} \frac{1}{2}H_2$$

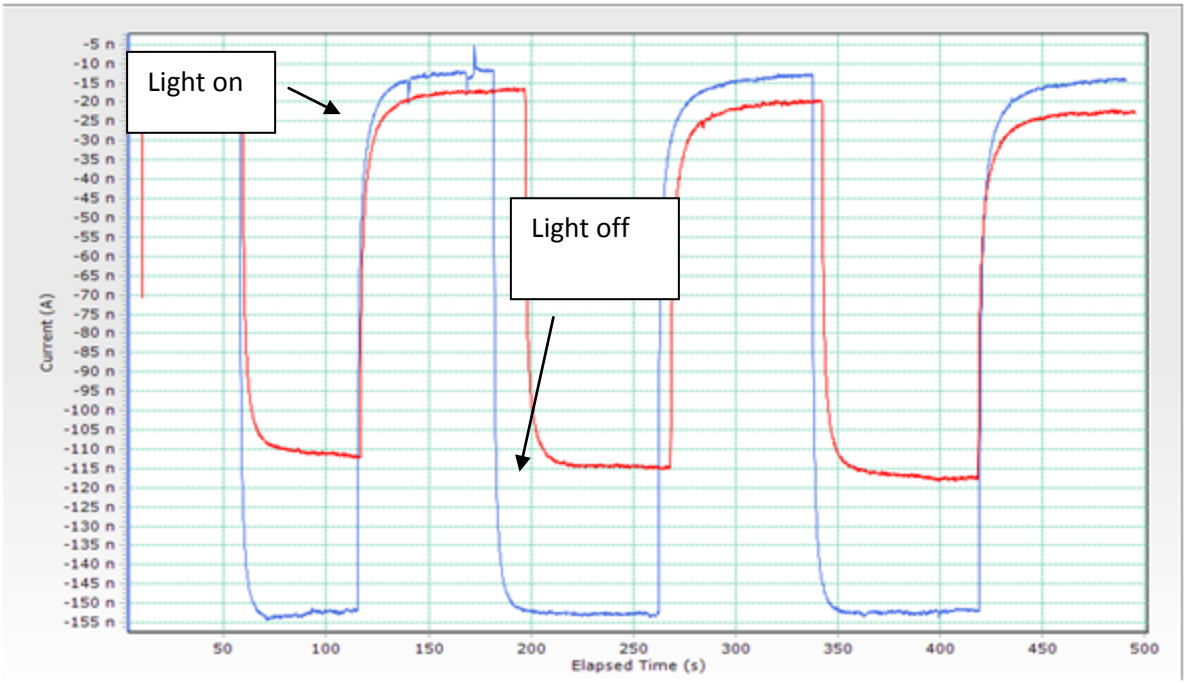

Figure 5.12 Chronoamperometric result of $CuWO_4$-CuO nanocartalyst under visible (Red) and simulated sunlight (Blue).

Figure 5.12 shows strong response of the $CuWO_4$-CuO nanocartalyst to visible light (λ>400nm) and simulated sunlight that resulted in current formation when the light (visible) is switched on-i.e. reduction of benzoic acid upon illumination of the catalyst. With a 0.5V applied bias, the dark reverse leakage current of the $CuWO_4$-CuO nanocartalyst was approximately -153 nA but the current increased rapidly to -12 nA upon simulated sunlight illumination. With visible light illumination, 90 nA of photocurrent was produced. The photocurrents should be produced electron hole separation at the p-n junction with electrons moving towards the electrolyte and holes moving towards the ITO.

The set up is optimized for continuous thin films deposited on ITO but due to the nano-scale and highly porous nature of our nanogrid catalyst there are current losses due to the poor contact made between the nanogrid and the ITO substrate. Zheng et al. showed electrochemical analysis on $CuWO_4$-CuO/ITO that lower recombination of electron-hole pairs since there are no great initial catholic photocurrent spikes [17].

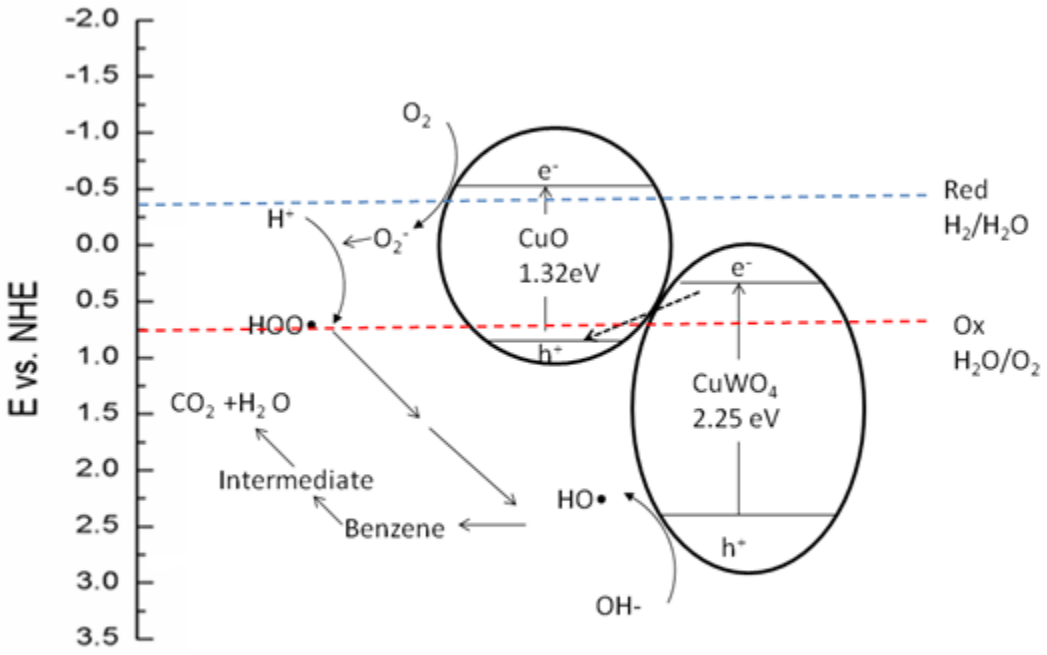

Figure 5.13 Schematic diagram of with band gap position of $CuWO_4$-CuO photocatalyst relative to energy levels at PH=7 with respect to the normal hydrogen electrode (NHE). [17].

The mechanism may be explained by the p-n type diode model. The majority carrier from each metal oxide, electrons in n-type $CuWO_4$ and holes in p-type CuO can migrate and recombine due to their band gap overlapping and interconnected structure. This model also corresponds to Zheng et al.[17]'s experimental results converting photocurrent from p-type to n-type. The

minority carriers from each metal oxides; holes in $CuWO_4$ and electrons in CuO react with water and oxygen to produce radicals.

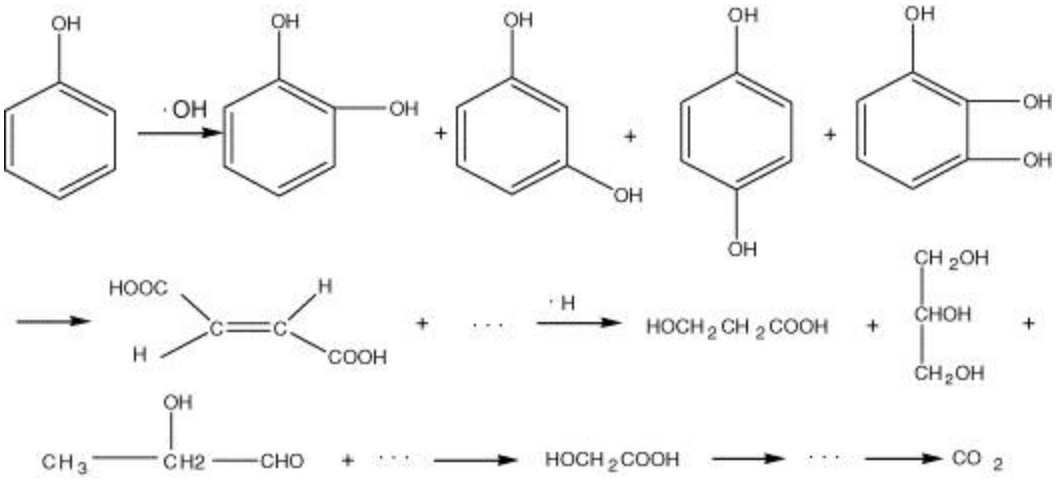

Figure 5.14 Benzene derivative(phenol) degradation upon sunlight illumination in aqueous environment [20].

The produced radicals, especially •OH radicals, result from H^+ or H• scavenge of oxygen attacks the benzene and transform to phenol and hydrouquine. The phenol degradation by •OH was well studied in several researchers[20].

5.4. Conclusion

$CuWO_4$ (n-type) - CuO (p-type) nanostructured photocatalyst were synthesized by sol-gel processing. The $CuWO_4$–CuO nanocatalysts are 20-800 nm of diameter with porous surface. The photocatalytic test on benzene degradation under natural light showed that concentration of benzene decrease from 43,825 to 2.8 ppm within 3 days. These catalysts generate 140 nA/cm2 under simulated sun light with 0.1M benzoic acid/0.1M KOH. Photocatalytic degradation on methlyene blue test showed that the $CuWO_4$-CuO degraded more than 80% which is faster that commercial TiO2. The high photocatalytic rate and relatively simple synthesis step of $CuWO_4$(n-type)– CuO (p-type) is a promising heterojunction visible light-activated photocatalyst.

.

Reference

1. Mascarelli, A., *Deepwater Horizon: After the oil,* in *Nature*2010. p. 22-24

2. Nair, M., Z.H. Luo, and A. Heller, *Rates of Photocatalytic Oxidation of Crude-Oil on Salt-Water on Buoyant, Cenosphere-Attached Titanium-Dioxide.* Industrial & Engineering Chemistry Research, 1993. **32**(10): p. 2318-2323.

3. Grzechulska, J., M. Hamerski, and A.W. Morawski, *Photocatalytic decomposition of oil in water.* Water Research, 2000. **34**(5): p. 1638-1644.

4. Huang, H., et al., *Efficient Degradation of Benzene over LaVO4/TiO2 Nanocrystalline Heterojunction Photocatalyst under Visible Light Irradiation.* Environmental Science & Technology, 2009. **43**(11): p. 4164-4168.

5. Heller, A., et al., *APPLICATION OF PHOTOCATALYTIC HOLLOW GLASS MICROBEADS IN THE CLEANUP OF OIL SPILLS.* International Oil Spill Conference Proceedings, 1993. **1993**(1): p. 623-627.

6. Gaya, U.I. and A.H. Abdullah, *Heterogeneous photocatalytic degradation of organic contaminants over titanium dioxide: A review of fundamentals, progress and problems.* Journal of Photochemistry and Photobiology C: Photochemistry Reviews, 2008. **9**(1): p. 1-12.

7. Hashimoto, K., H. Irie, and A. Fujishima, *TiO2 photocatalysis: A historical overview and future prospects.* Japanese Journal of Applied Physics Part 1-Regular Papers Brief Communications & Review Papers, 2005. **44**(12): p. 8269-8285.

8. Marsen, B., et al., *Progress in sputtered tungsten trioxide for photoelectrode applications.* International Journal of Hydrogen Energy, 2007. **32**(15): p. 3110-3115.

9. Xu, Z., et al., *Preparation of platinum-loaded cubic tungsten oxide: A highly efficient visible light-driven photocatalyst.* Materials Letters, 2011. **65**(9): p. 1252-1256.

10. Yourey, J.E., et al., *Chemical Stability of CuWO4 for Photoelectrochemical Water Oxidation.* The Journal of Physical Chemistry C, 2013. **117**(17): p. 8708-8718.

11. Doumerc, J.P., et al., *A photoelectrochemical study of CuWO4 single crystals.* physica status solidi (a), 1984. **82**(1): p. 285-294.

12. Jayaraman, S., et al., *Synthesis and Characterization of Pt−WO3 as Methanol Oxidation Catalysts for Fuel Cells.* The Journal of Physical Chemistry B, 2005. **109**(48): p. 22958-22966.

13. Arai, T., et al., *Reaction Mechanism and Activity of WO3-Catalyzed Photodegradation of Organic Substances Promoted by a CuO Cocatalyst.* The Journal of Physical Chemistry C, 2009. **113**(16): p. 6602-6609.

14. Lee, J. and P.I. Gouma, *Tailored 3D CuO Nanogrid Formation.* Journal of Nanomaterials, 2011. **2011**.

15. Patterson, A.L., *The Scherrer Formula for X-Ray Particle Size Determination.* Physical Review, 1939. **56**(10): p. 978-982.

16. Yourey, J.E. and B.M. Bartlett, *Electrochemical deposition and photoelectrochemistry of CuWO4, a promising photoanode for water oxidation.* Journal of Materials Chemistry, 2011. **21**(21): p. 7651-7660.

17. Zheng, J.Y., et al., *Facile preparation of p-CuO and p-CuO/n-CuWO4 junction thin films and their photoelectrochemical properties.* Electrochimica Acta, 2012. **69**(0): p. 340-344.

18. Treimer, S.E. and D.H. Evans, *Electrochemical reduction of acids in dimethyl sulfoxide. Comparison of weak C–H, N–H and O–H acids.* Journal of Electroanalytical Chemistry, 1998. **455**(1–2): p. 19-28.

19. Barrette, W.C. and D.T. Sawyer, *Determination of dissolved hydrogen and effects of media and electrode materials on the electrochemical oxidation of molecular hydrogen.* Analytical Chemistry, 1984. **56**(4): p. 653-657.

20. Guo, Z., R. Ma, and G. Li, *Degradation of phenol by nanomaterial TiO2 in wastewater*. Chemical Engineering Journal, 2006. **119**(1): p. 55-59.

Chapter 6. Super-Hydrophobic Fibrous Cellulose Acetate (CA) Mats as Oil Selective Sorbents and Photocatalysts Suopport.

6.1 Introduction

Oil derivatives are among the most dangerous compounds for the environment, due to their long degradation time and ease of migration in aquatic settings[1]. Oil spill disasters can be of large scale, such as the Gulf of Mexico oil spill in 2010 that resulted in a 600 miles wide zone of 9 million gallons of medium crude oil spread across the surface of the ocean, and have reached the shoreline in some cases [2]. Immediate reaction is required to contain and clean such a spill preventing it from harming the environment and to the wildlife. While there are several efforts made toward oil spill remediation, including mechanical collection, combustion, chemical dispersant, and photocatalytic decomposition[3], there are many disadvantages using these approaches, cost being the prominent one. However, limited options that concern biodegradable and affordable technologies are available Absorption-based methods using in particular nonwoven absorbent mats, have drawn a lot of attention recently because of the low density, high sorbent capacity and readily available in large-scale of the product [4, 5].The ideal absorbent for oil spill cleanup should exhibit hydrophobicity, oleophilicity, high sorption capacity, buoyancy, long retention time and biodegradability [6]. This paper focuses on a fibrous nanotechnology that meets all of the above requirements.

Cellulose acetate (CA) is known as hydrophilic materials [7], produced by acetylation of cellulose, one of the most abundant and low-cost renewable natural polymers, used in a broad field of application such as textile, membranes and filters. [8] Unlike cellulose, CA has amorphous structure thus is more soluble in common organic solvents such as acetone, and it is biodegradable [8], [9]. The number and position of functional polar groups of CA, such as OH and COOH, may substantially change the sorption properties due to the oriented interaction and formation of strong hydrogen bonds[10]. Studies of CA fibrous structure produced via the electrospinning process have been conducted extensively in recent years[11, 12]. Electrospinning is a simple and versatile method for fabrication of continuous fibrous mats with diameter ranging from a few nanometers to a few micrometers. The as-spun fibrous mats show low density, high surface roughness and surface-to-volume ratio. The purpose of this work is to investigate the oil sorption properties of electrospun CA fiber produced in various different configurations.

6.2. Experimental section

All chemicals were used as received without any purification. The procedure followed involved dissolving CA (*Sigma*-Aldrich, M_w=29,000) in 60% acetone/40% acetic acid solvent at a concentration of 15wt/vol%. After 1h of mixing by ultrasonication, the solution was loaded into a syringe with a blunt stainless needle. The syringe was placed in a syringe pump (KD Scientific) and the needle was connected to a high-voltage supply and positioned perpendicularly 7 cm from a piece of aluminum foil grounding electrode. Upon applying a high voltage of 18-20kV, a solution jet was ejected from the needle tip. The solvent evaporated and web of fibers deposited on the aluminum foil. The syringe pump was programmed to dispense the solution at a flow rate of 30µl/min.

Thin films of CA were also prepared on glass slides by using a two-stage spin coating (Spin Coater KW-4A, Chemat Technology) technique at steps of 600/2,500 rpm for 5 and 10 s for evenly spreading the 15wt/vol% of CA solution. The thin CA films thus obtained were dried in air for 30 min.

The water contact angle of CA fiber mats and CA thin film were measured on optical contact angle meter (CAM 200, KSV Instruments Ltd). FTIR spectrometer (Nicolet Magna 560 FTIR Spectrometer) was used to analyze the chemical components of CA fibers. Experiments were run in triplicate and the results were normalized.

Three types of liquid hydrocarbons, No. 6 fuel oil, vegetable oil, and benzene, were employed to compare sorption ability of CA fibrous mats and commercial polypropylene (PP) sorbent (New Pig, USA). The sorption capacity of CA fibrous mats and commercial PP sorbent were determined by ASTM 23 F726-99 [13]. Sample pieces of sorbents were cut into squares (3 by 3 cm) then weighted. The weighted sorbents were placed into different types of oils and distilled water for 5 min. The sorbent materials were strained through mesh basket and drained for 30s before measuring their weight. The oil-absorbency, Q, as the ratio of oil adsorbed to dry sorbent weight, was calculated by following equation:

$$Q = \frac{W_e - (W_o + W_w)}{W_o}$$

Where W_o is the initial weight of the specimen, W_w is the weight of the adsorbed water, and W_e is the weight of specimen at end of sorption test. The quantity of adsorbed oil was recorded as grams per gram of sorbent (g/g). All tests were performed at 22±2 ℃.

6.3. Results and discussion

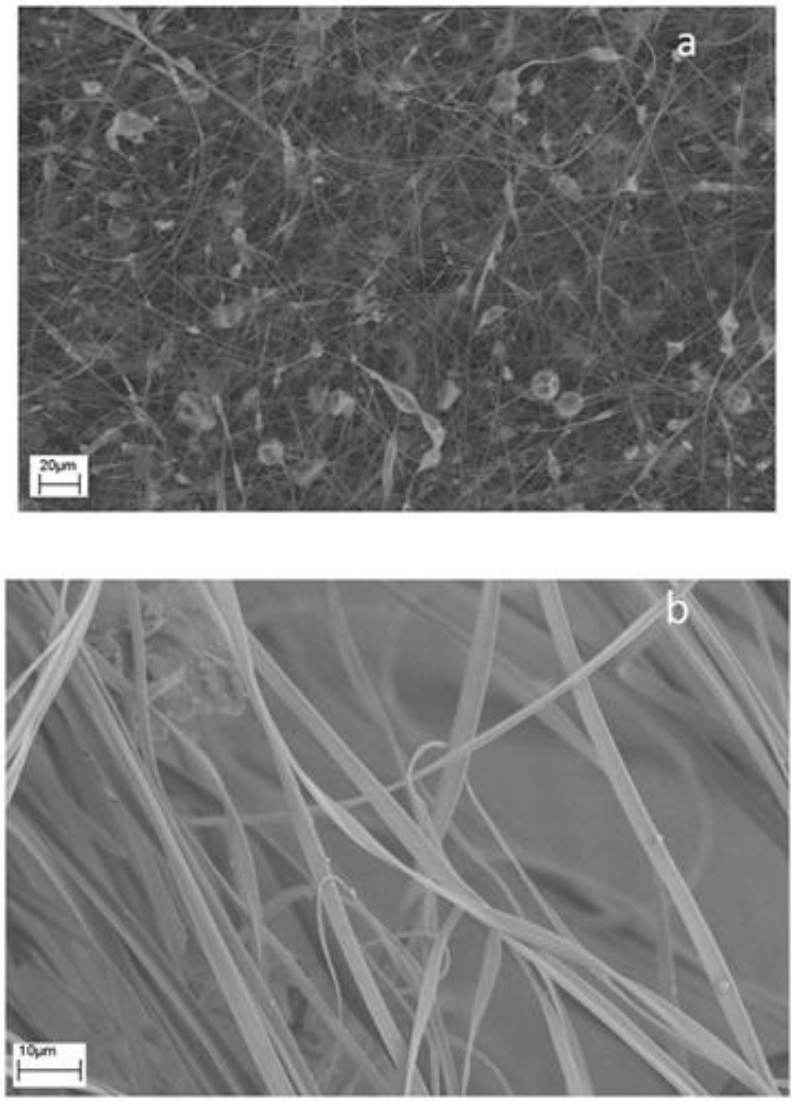

Figure 6.1 SEM micrographs of the CA fiberous mats in (a) low magnification and in (b) high magnification.

The morphology of the electrospun CA fibrous mats was studied in a scanning electron microscopy (SEM) (LEO 1550 electron microscope) (see Figure 6.1). The as-spun mats looked

cotton-like and were formed as several layers of randomly oriented fibers with open porosity throughout their thickness. SEM images showed the non–woven CA mats with fiber diameters of 1-3µm.

The high magnification SEM micrographs showed some folded ribbons with microsized beads. The ribbon shape is typically caused by the fast evaporation of solvent forming strong skins on the jet and as the solvent evaporation progresses, the skin remains and a hollow tube collapses into a flat ribbon with porous interiors[14]. The beads usually form the result of a surface tension driven instability by a nanoscale extrusion process[14].

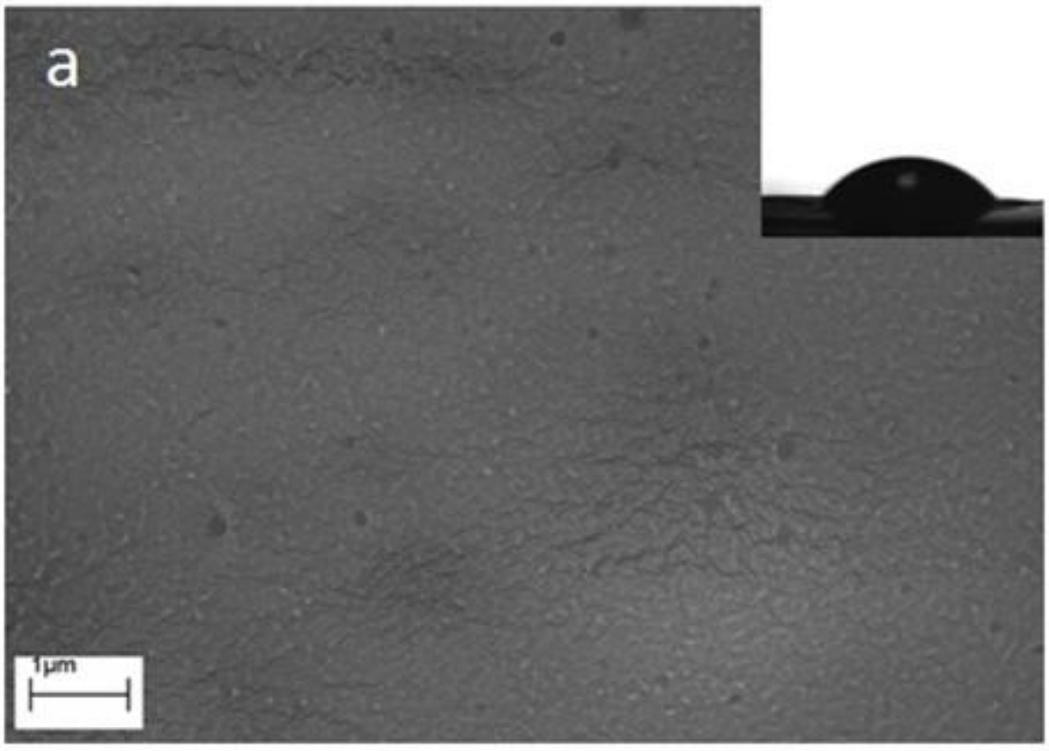

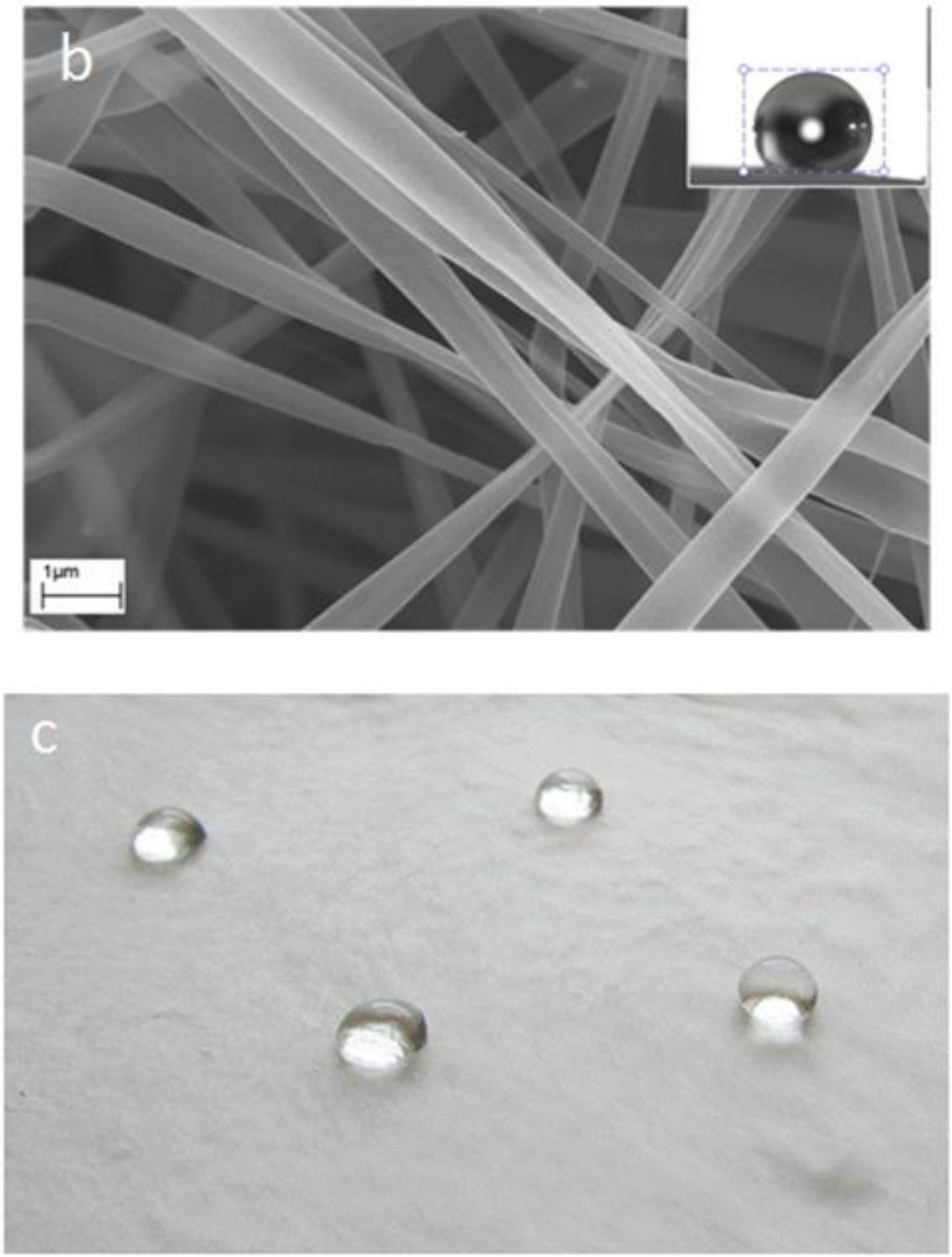

Figure 6.2 SEM images (a) spin-coated CA film and b) electrospun CA fibrous mats and their water contact angle measurement. Inset: (a) 57.4^{o} and (b) 137^{o}, respectively. (c) Image of water droplets on CA fibrous mats.

Figure 6.2 shows the results of a droplet test on the fibrous mat vs. a spin-coated thin film of the same material. It is generally agreed that a hydrophobic surface shows high water contact angle ($\theta > 90°$)[15]. The spin-coated CA film, Figure 2(a), shows relatively continuous and smooth surface. Measurement of water contact angle on spin-coated CA thin film reads 57.4^{o}, indicating hydrophilic. Whereas the water droplet on CA fibrous mats, Figure 2(b), gives a contact angle of 137^{o} thus being highly hydrophobic. The porous surface of CA fibrous mats may traps air between bottom surface and water droplets resulting in high contact angle. [16]

Bin *et al*. [17] reported on conversion of CA mat surface from super-hydrophilic to super-hydrophobic with sol-gel coating of decyltrimethoxysilane(DTMS) and tetraethyl orthosilicate (TEOS). However, the above results reveal that surface property has been converted from hydrophilic to hydrophobic by simply changing the morphology of the material from bulk to fibrous. As an oil sorbent application, hydrophobic surface of CA fibrous mats are more desirable since the hydrophilic absorbent has low oil/water selectivity.

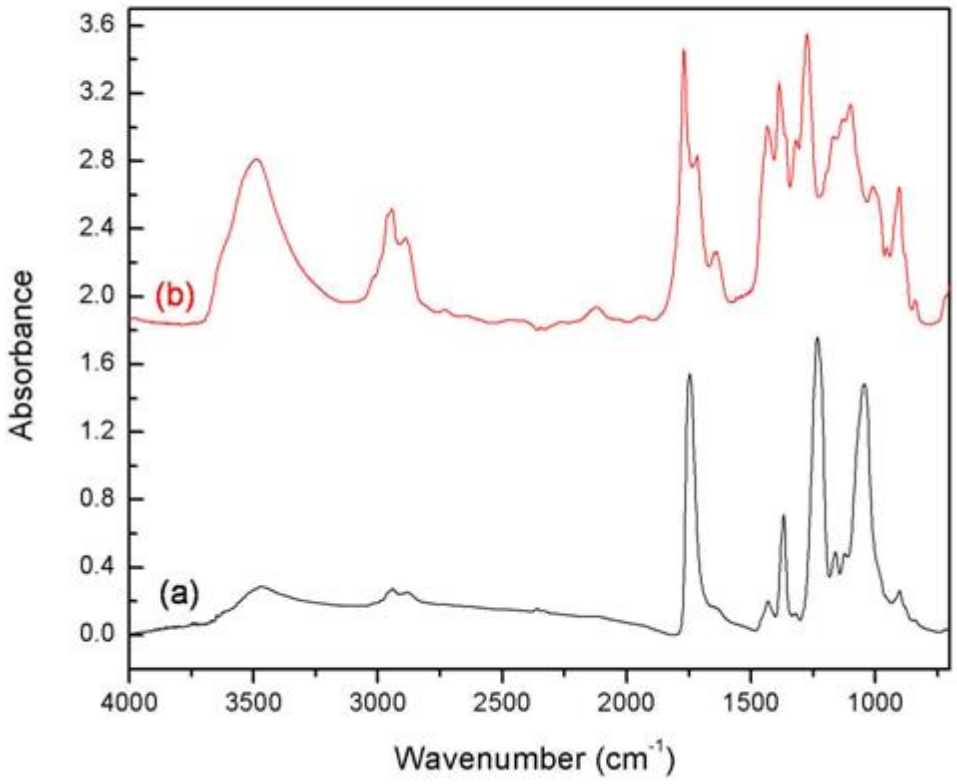

Figure 6.3 FT-IR spectra of as-electrospun (a) CA fibrous mats and (b) spin-coated CA thin film.

Figure 6.3 draws the comparison between the FTIR spectra of the electrospuned CA fiberous mats and spin-coated CA thin film. The three ester bands present in FTIR spectra of CA fibrous mats and spin-coated CA thin film at 1,740-1,745 cm^{-1}, which are attributed to the symmetric stretching carbonyl group (C=O) of the acetyl group ($-COCH_3$) in cellulose acetate[18], 1369 (C-H in $–O(C=O)-CH_3$) and 1234 cm^{-1}(C-O stretching of acetyl group)[19] . The intensity of the band at 3480-3485 cm^{-1}, representing the hydroxyl group (-OH) [20] and OH in-plane bending bands at 1337,1310 and 1200 cm^{-1} [19] is relatively lower on electrospun CA fibrous than that of spin-coated CA thin film. [10]

Yamane *et al.* [21] has claimed the hydrophilic and hydrophobic behavior of cellulose is due to the location of hydroxyl groups at the equatorial positions of glucopyranose rings and

hydrogen atoms at the axial positions of glucopyranose rings. In this experiment, the CA fibrous mats may have anisotropic physical properties due to the alignment of extended molecular chain whereas the thin film's isotropic properties resulting in high density of hydroxyl groups on the surface area. [22] As a result, the electrospun CA fibrous mats had significant hydrophobic surfaces while the spin-coated CA thin film was hydrophilic.

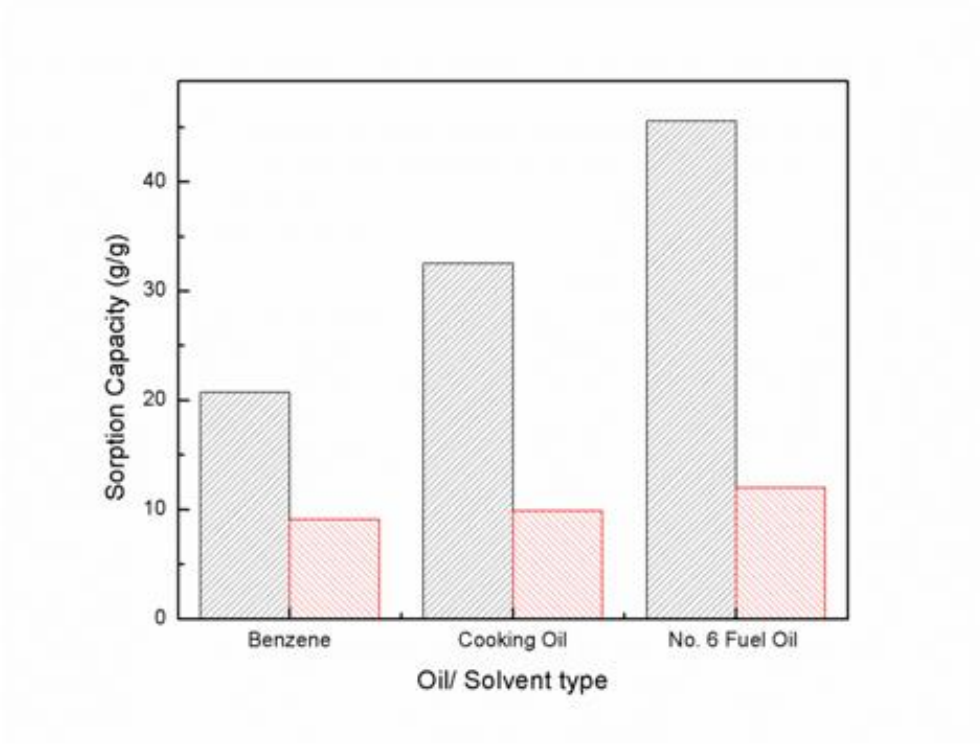

Figure 6.4. Sorption capacity of the CA fibrous mats(black) and commercial PP sorbent(red) for the three different oils.

Figure 6.4 shows the sorption capacity of CA fibrous mats and commercial PP sorbent (New Pig, USA) for the three different oils. The sorption capacity of CA fibrous mats and commercial PP sorbent for benzene, vegetable oil, and No. 6 fuel oil are 20.7, 32.5, and 45.6 g/g and 9.1, 9.9, and 12.0 respectively. The sorption capacity of the CA fibrous mats increase in the following order: benzene, vegetable oil and No. 6 fuel oil. The commercial PP sorbent also shows similar sorption behavior for all 3 chemicals. The different sorption capacity may be caused by their viscosity and density [6]. The overall sorption capacity of CA fibrous mats show 2-4 times better than commercial PP sorbent. In addition, the CA fibrous mats are biodegradable and will not cause supplementary pollution.

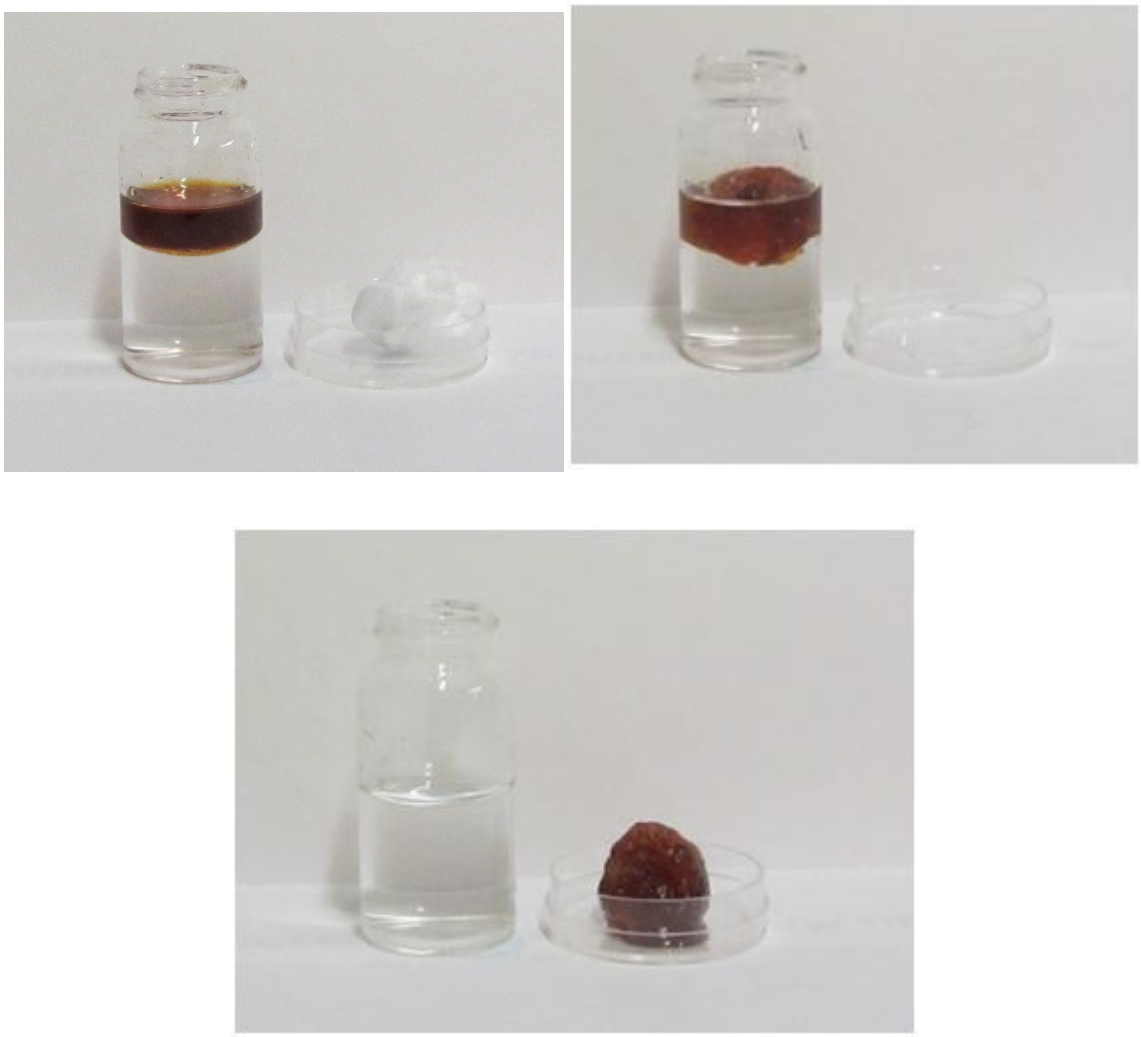

Figure 6.5 Buoyancy and sorption test of No. 6 fuel oil on water by CA fibrous mats.

Figure 6.5 shows the sorption and buoyancy test result in water oil-water bath. A layer of No. 6 fuel oil (2ml) is instantly removed by addition of the CA fibrous mats and the sorbent was stayed on the top of the water. The high buoyancy of CA fibrous mats before and after the oil sorption over the water surface is an important factor for practical use of the CA sorbent in oil spills cleanup in aqueous environment.[6]

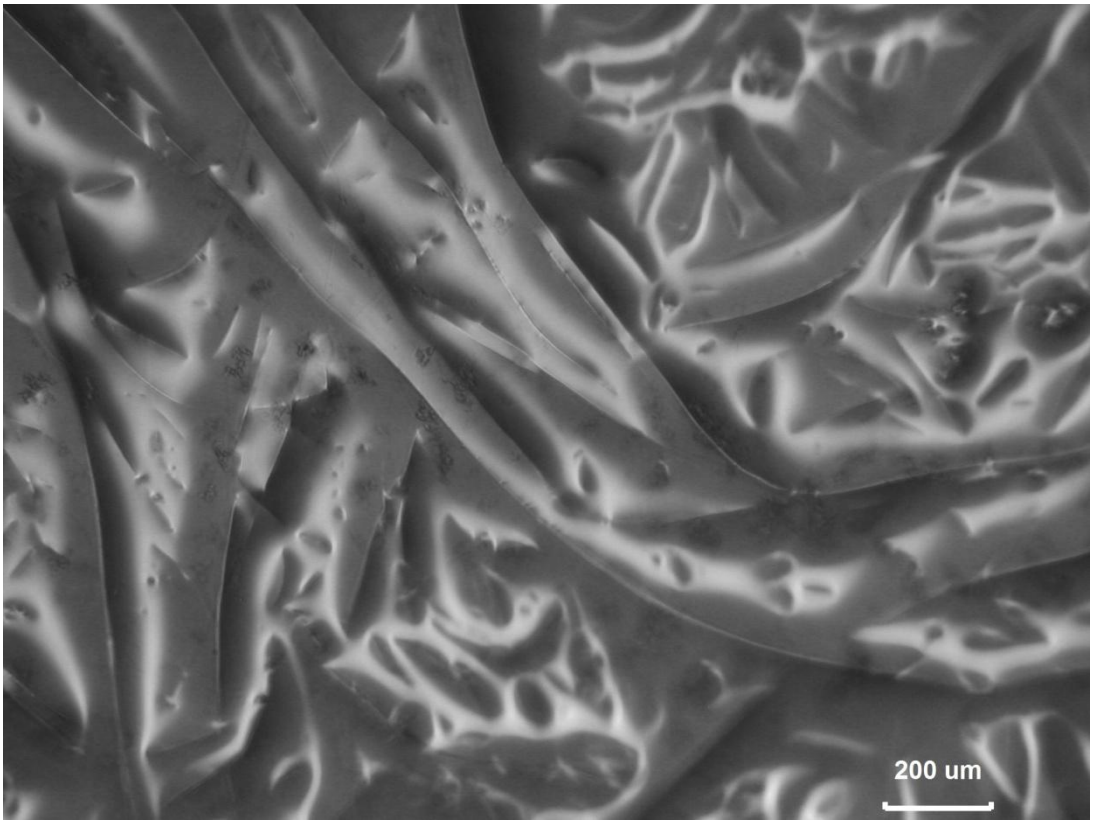

Figure 6.6 Optical microscope image of CA fibrous mats after sorption of fuel No.6 oil.

The CA fibrous mats 5 minutes after exposure to fuel No.6 oil saturated was observed with optical microscope (see Figure 6.6) to investigate the sorption mechanism. The voids within the fibrous mats are filled with oil and the oil adheres to the surface of fibers. The main sorption mechanism for fibrous oil sorbents can be absorption through a capillary action, or a combination of these.[23] As seen in Figure 6, the most oil is retained in void area and fibers' surface and having high porosity with high surface-to-volume ratio show advantages over other commercial synthetic oil sorbents, such as polypropylene.

6.4. Conclusion

CA non-woven nanomats with a 3D fibrous structure were successfully prepared by the electrospinning process. The unique hydrophobic surface of these mats with water contact angle of 137° had relatively less hydroxyl groups (-OH) compared to typical CA thin films. The

increased sorption capacity, simple fabrication method, high surface-area-to mass or volume ratios, high buoyancy, and biodegradable CA fibrous mats make them suitable candidates for commercial products to clean up oil spills.

Reference

1. Barth, T., *Weathering of crude oil in natural marine environments: The concentration of polar degradation products in water under oil as measured in several field studies.* Chemosphere, 1984. 13(1): p. 67-86.

2. Mascarelli, A., *Deepwater Horizon: After the oil*, in *Nature* 2010. p. 22-24.

3. Grzechulska, J., M. Hamerski, and A.W. Morawski, *Photocatalytic decomposition of oil in water.* Water Research, 2000. 34(5): p. 1638-1644.

4. Crini, G., *Recent developments in polysaccharide-based materials used as adsorbents in wastewater treatment.* Progress in Polymer Science, 2005. 30(1): p. 38-70.

5. Adebajo, M.O., et al., *Porous materials for oil spill cleanup: A review of synthesis and absorbing properties.* Journal of Porous Materials, 2003. 10(3): p. 159-170.

6. Zhu, H.T., et al., *Evaluation of Electrospun Polyvinyl Chloride/Polystyrene Fibers As Sorbent Materials for Oil Spill Cleanup.* Environmental Science & Technology, 2011. 45(10): p. 4527-4531.

7. Fischer, S., et al., *Properties and Applications of Cellulose Acetate.* Macromolecular Symposia, 2008. 262(1): p. 89-96.

8. Puls, J., S.A. Wilson, and D. Hölter, *Degradation of Cellulose Acetate-Based Materials: A Review.* Journal of Polymers & the Environment, 2011. 19(1): p. 152-165.

9. Sassi, J.-F. and H. Chanzy, *Ultrastructural aspects of the acetylation of cellulose.* Cellulose, 1995. 2(2): p. 111-127.

10. Skornyakov, I.V. and V.P. Komar, *IR spectra and the structure of plasticized cellulose acetate films.* Journal of Applied Spectroscopy, 1998. 65(6): p. 911-918.

11. Tungprapa, S., et al., *Electrospun cellulose acetate fibers: effect of solvent system on morphology and fiber diameter.* Cellulose, 2007. 14(6): p. 563-575.

12. Sassi, J.F. and H. Chanzy, *ULTRASTRUCTURAL ASPECTS OF THE ACETYLATION OF CELLULOSE.* Cellulose, 1995. 2(2): p. 111-127.

13. ASTM, *Standard Test Method for Sorbent Performance of Adsorbents* 1999, ASTM: Philadelphia, PA.

14. Reneker, D.H. and A.L. Yarin, *Electrospinning jets and polymer nanofibers.* Polymer, 2008. 49(10): p. 2387-2425.

15. Förch, R., Schönherr,H., Jenkins, A.T. A. , *Surface design: applications in bioscience and nanotechnology*. 1 ed2009: Wiley-VCH. p. 471.

16. Cassie, A.B.D. and S. Baxter, *Wettability of porous surfaces.* Transactions of the Faraday Society, 1944. 40(0): p. 546-551.

17. Bin, D., et al., *Conversion of an electrospun nanofibrous cellulose acetate mat from a super-hydrophilic to super-hydrophobic surface.* Nanotechnology, 2006. 17(17): p. 4332.

18. Tserki, V., et al., *A study of the effect of acetylation and propionylation surface treatments on natural fibres.* Composites Part A: Applied Science and Manufacturing, 2005. 36(8): p. 1110-1118.

19. Adebajo, M.O. and R.L. Frost, *Acetylation of raw cotton for oil spill cleanup application: an FTIR and 13C MAS NMR spectroscopic investigation.* Spectrochimica Acta Part A: Molecular and Biomolecular Spectroscopy, 2004. 60(10): p. 2315-2321.

20. Sun, X.F., R. Sun, and J.X. Sun, *Acetylation of rice straw with or without catalysts and its characterization as a natural sorbent in oil spill cleanup.* J Agric Food Chem, 2002. 50(22): p. 6428-33.

21. Yamane, C., et al., *Two different surface properties of regenerated cellulose due to structural anisotropy.* Polymer Journal, 2006. 38(8): p. 819-826.

22. Iwamoto, S., A. Isogai, and T. Iwata, *Structure and Mechanical Properties of Wet-Spun Fibers Made from Natural Cellulose Nanofibers.* Biomacromolecules, 2011. 12(3): p. 831-836.

23. Choi, H.-M., H.-J. Kwon, and J.P. Moreau, *Cotton Nonwovens as Oil Spill Cleanup Sorbents.* Textile Research Journal, 1993. 63(4): p. 211-218.

Chapter 7. Summary and future work

7.1. Summary

The novel morphology of CuO-TiO_2 nanofibrous mats were fabricated by blend electrospinning using a sol-gel precursor. The photocatalytic activities of the pure TiO_2 and CuO-TiO_2 nanofibrous mats catalysts have been demonstrated under UV light and under visible light. The UV-Vis spectroscopy results indicated that, based on the degradation of MB solution, the nanofibrous mats are strongly effective visible light activated photocatalysts that offer 97% dye degradation under visible light. The relatively high photocurrent-to-dark-current contrast ratio and the fast responses also suggest that the CuO-TiO_2 nanofibrous mats described are potentially useful for highly efficient visible light-activated photocatalysts for environmental and energy applications.

CuO nanogrids were synthesized by direct thermal oxidation of composite substrates consisting of a Cu mesh and PVP nanofibers deposited on it by electrospinning. It results from the templating action of electrospun nanomats of polymers deposited on Cu mesh. The estimated band gap energy is ~1.33eV, which is larger than reported value for bulk CuO (E_g= 1.2eV).

$CuWO_4$ (n- type)–CuO (p-type) nanostructured photocatalyst were synthesized by sol-gel processing. The $CuWO_4$–CuO nanocatalysts are 20-800 nm of diameter with porous surface. The preliminary photocatalytic test on benzene degradation under natural light showed that concentration of benzene decreased from 43,825 to 2.8 ppm within 3 days. Photocatalytic degradation on methlyene blue test showed that the $CuWO_4$-CuO degraded more than 80% which is faster that commercial TiO2. The $CuWO_4$–CuO catalyst generated photocurrent 140 nA/cm^2 under simulated sun light with 0.1 M benzoic acid/0.1 M KOH.

A nonwoven cellulose acetate (CA) nanofibrous mats was prepared by electrospining process for selective oil sorbent. The morphology and chemical analysis have done by scanning electron microscope (SEM) and Fourier transform infrared spectroscopy (FT-IR). The sorption capacity results of the CA nanofibrous sorbent for No. 6 fuel oil, vegetable oil, and benzene showed 44, 33, and 22 g/g, respectively. The CA mats have hydrophobic surface with a contact angle 137^o and high buoyancy. The electrospun CA fiber mats is biodegradable, high sorption

capacity, fast, and cost-effective solution to remediate oil spill in aqueous environment and potential template of nanostructured catalysts.

7.2. Future research directions

Synthesized nanostructured visible light-activated photocatalysts showed high water remediation properties but they can also be used as solar-powder water splitter. For that, more studies need to be done on chemical stability in aqueous environment and direct H_2 production rate measurement from the water splitting effect.

Synthesized nanostructured TiO_2-CuO and $CuWO_4$-CuO have high surface area with self supporting structure. However, these nanocatalysts are too brittle to handle in large scale applications which require supporting structure. Super hydrophobic CA nanofibrous mats can be a potential template structure due to its hydrophobic and high surface area. Core-shell structure and nanoparticles embedding composite structure are future research.

The fabricated CuO nanogrids from chapter 3 were tested for anode of lithium battery and the result showed stable capacity around 680 $mAhg^{-1}$. Recently, scientists are focusing on silicon anode, which could have potentially ten times more than that of the current carbonate anodes. However, its structural instability during charging and discharging cycle is one of the disadvantages. Therefore, CuO nanogrids' structural stability during charging/discharging cycles needs to be investigated.

Stable ε-WO_3 particle studied in appendix 2 showed high sensitivity on N_2 gas in room temperature. The ε-WO_3 is also known as a sensing material for acetone detection due to high dipole moments but it showed phase change during sensor operation temperature (>300℃). Therefore, phase stability upon heat treatment and sensing ability on acetone gas need has to be studied for future.

Appendix 1. CuO as Anode in Lithium Ion Batteries

A1.1. Introduction

Since a lithium ion battery (LIB) with carbonaceous anode (e.g. graphitic) has been dominated in commercial market from 1990, researchers tried to look for an alternative anode material. Especially, transition metal oxides (TMO) are consider as potential anode materials which under goes conversion reaction with lithium following equation [1]:

$$M_xO_y + 2y\ Li^+ + 2y\ e^- \leftrightarrow x\ M^0 + y\ Li_2O$$

where M is transition metals such as Fe, CO, Ni, Cu, etc. This leads to the formation metallic state (M^0) and Li_2O nanoparticles [24]. Due to the multiple electron reaction, the TMO's reversible capacity (>400 $mAhg^{-1}$) exceed that of the graphitic anodes.

A1.2. Lithium-ion battery assembly

A 2032 type coin cell was assembled in argon atmosphere. The CuO based positive electrode was consisting of synthesized CuO (80 wt%, as active materials), Polyvinylidene Fluoride (PVDF) (10 wt%, as binder) and super P carbon (10 wt%, as a conductive additive), and the negative electrode was lithium metal (0.37 mm thickness). A porous glass fiber soaked with the electrolyte was used as the separator. For the electrolyte, 1 M of $LiPF_6$ dissolved in a 1:1 volumetric mixture of anhydrous ethylene carbonate (EC) and anhydrouas dimethyl carbonate (DMC) was used. The cycled galvanostatic charge-discharge test was performed by using Arbin Instruments galvanostat/potentiostat at ambient temperature. The potential limit was set up in 0.02 – 3.00 V at a rate of C/6.

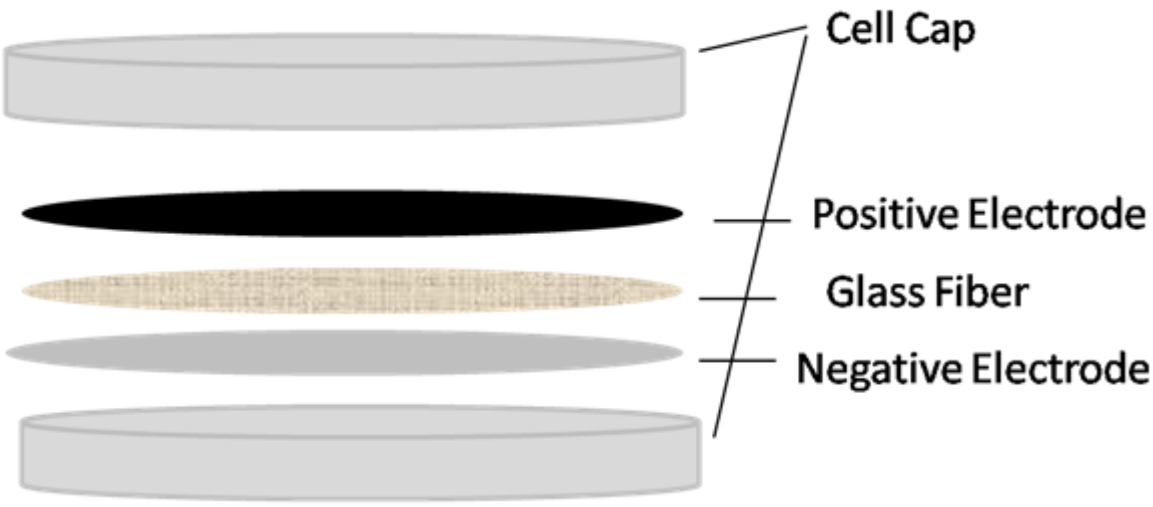

Figure A1.1 Schematic diagram of coin cell 2032.

A 2032 type coin cell was assembled in argon atmosphere (see Figure A1.1) as anode for CuO grids.

A.1.3. Test result/discussion

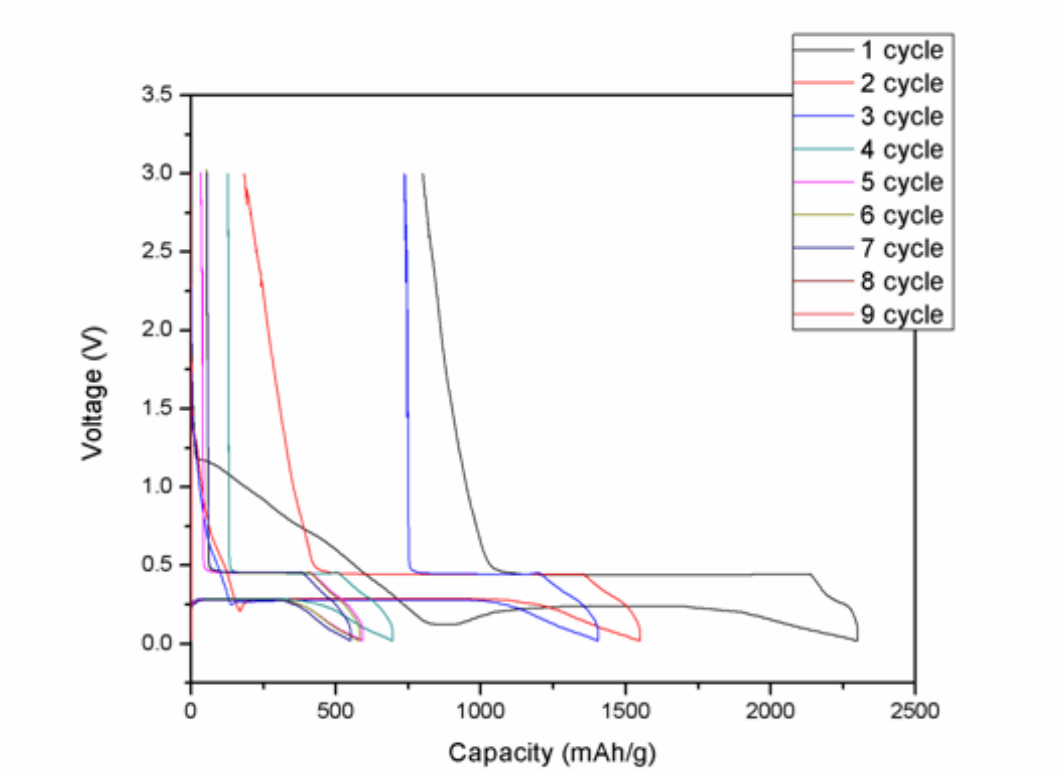

Figure A1.2 Charge-discharge curve of synthesized CuO anode made from 8h of oxidation at 500C.

In general, the reaction of CuO with Li ions at low potential values was ascribed to following chemical reaction,

$$Cu_nO + 2Li \Leftrightarrow nCu + Li_2O$$

The theoretical electrochemical capacities of transition metal electrode was reported, 674mAg^{-1}, with 100% capacity retention for up to 100 cycles and high recharging rates. Figure 5.10 shows the Galvanostatic charge-discharge test results of 3D CuO nanostructure based electrode within voltage range 0.02 – 3.00 V at the current density 31mA g^{-1}. In first cycle, the cell voltage starts with 3.0V then sharply drops to 0.5V. The initial discharge capacity of CuO is 2305mAhg^{-1}, which was more than three times higher than previously reported result from other researchers. This may result of electrolyte participation in the electrochemical process. After the third cycle,

the capacity becomes stable around 680 $mAhg^{-1}$. The electrochemical reduction may process not only caused phase change of CuO to Cu_2O and Cu. The particle size and structure of electrode are critical components for electrochemical performance [2]. The synthesized 3D CuO nanogrids shows different properties from those reported for bulk CuO. The electrochemical performance of this synthesized CuO electrode is result of nanometric and high surface structure, which increases the electrochemical activities.

Appendix 2- A. FSP synthesis of a novel WO3 phases and composite nanostructures

A2.1. Introduction

Flame-Spray Pyrolysis (FSP) is a versatile rapid solidication process that allows the synthesis of nanoparticles with non-equilibrium phases. Wang et al. [1] produced nanoparticles of the rare ε-WO_3 phase ammonium tungstate hydrate solutions by using FSP process, however , to the best of our knowledge, there have been no reports on using tungsten (VI) isopropoxide. Here, ε-WO_3 nanoparticles have been produced from FSP. The produced powder was characterized with SEM, TEM, XRD, and Raman spectroscopy.

A2.2. Experimental Section

A2.2.1. Flame Spray Pyrolysis (FSP)

Flame-Spray Pyrolysis (FSP) is a versatile method of synthesis to produce nanoparticles in large scale with short time. Leading catalyst companies, such as Cabot, Cristal, PuPont, Degussa, and Ishihara, produce millions of tons, valued at more than $15 billion/yr, using flame aerosol synthesis method[2]. These flame-made materials, Carbon Blacks, SiO_2, TiO_2, Al_2O_3, and other ceramic nanoparticles, are widely used in applications such as reinforcing agent, pigments, flowing aids, as well as environmental and energy applications due to increasing need of complex and functional materials[3]. Aerosol synthesis is divided into three groups [4]: (a) vapour-fed aerosol flame synthesis (VAFS) utilize metal precursor in gas phase by using volatile solution such as $SiCl_4$ and $TiCl_4$ [5], (b) flame-assisted spray pyrolysis(FASP) utilize liquid precursor solution sprayed in flame sustained by a fuel where the state of low combustion enthalpy solution(less than 50% of total combustion energy) in aqueous solvent[6]; and (c) flame spray pyrolysis(FSP) is similar to FASP, but with significantly higher combustion enthalpy (higher than 50% of total energy of combustion) due to combustion driven from the flam process[7].

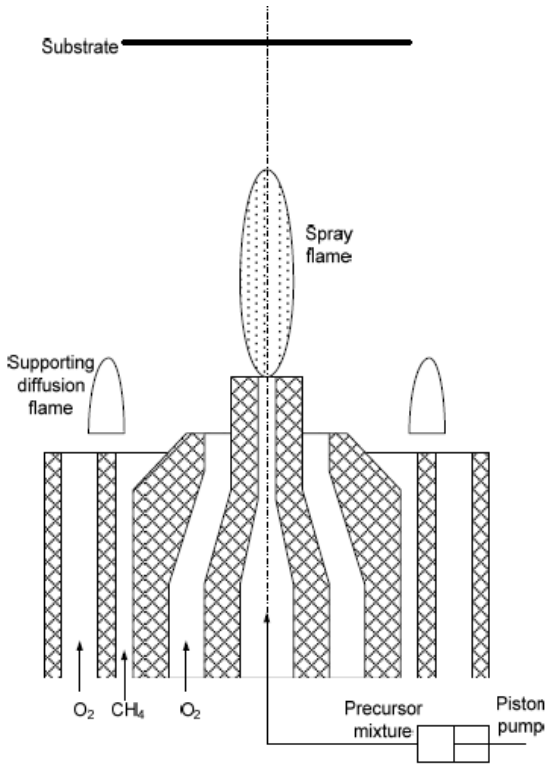

Figure A2.1 Schematic diagram of Flame Spray Pyrolysis (FSP) setup.

The amount O_2 present need to be kept minimum, since the main products from FSP process are the form of metal oxide, yet sufficient for complete combustion of hydrocarbon fuels. The details of FSP for metal oxide nanoparticles synthesis have been described in several review papers [3], [4]. Schematic diagram of Flame Spray Pyrolysis (FSP) setup is shown in figure A2.1.

A.2.2.2. Materials synthesis

WO_3 nanoparticles were synthesized using flame spray pyrolysis (FSP) (NP10, Tethis). To prepare the precursor solution, Tungsten isopropoxide (W-iso) was dissolve in 2-propanol in 0.38 M concentration in N_2 filled glove box. This solution was supplied at a rate of 5 ml/ min through the FSP nozzle and dispersed to a find spray to a fine spray with 5 l/min oxygen. The fine spray was ignited by a supporting gas rate (CH_4: 1.5 l/min and O_2: 3.2 l/min). The synthesized powder was deposited on glass-fiber filter (Whatman).

A2.3. Results and Discussion

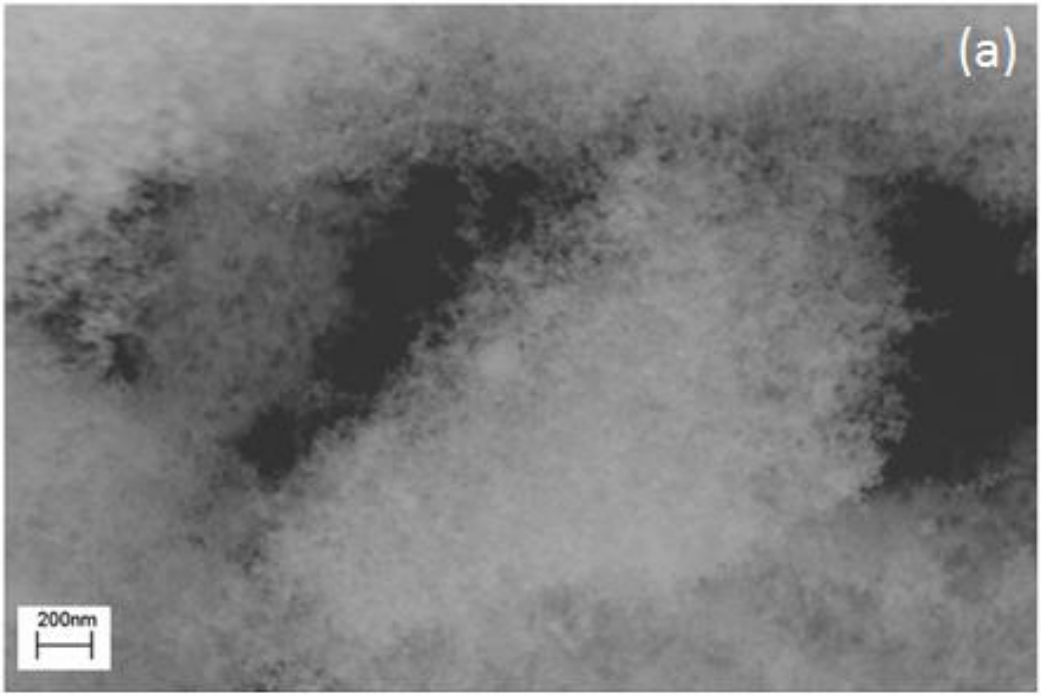

Figure A2.2 SEM image of the synthesized ε-WO_3 nanocrystals.

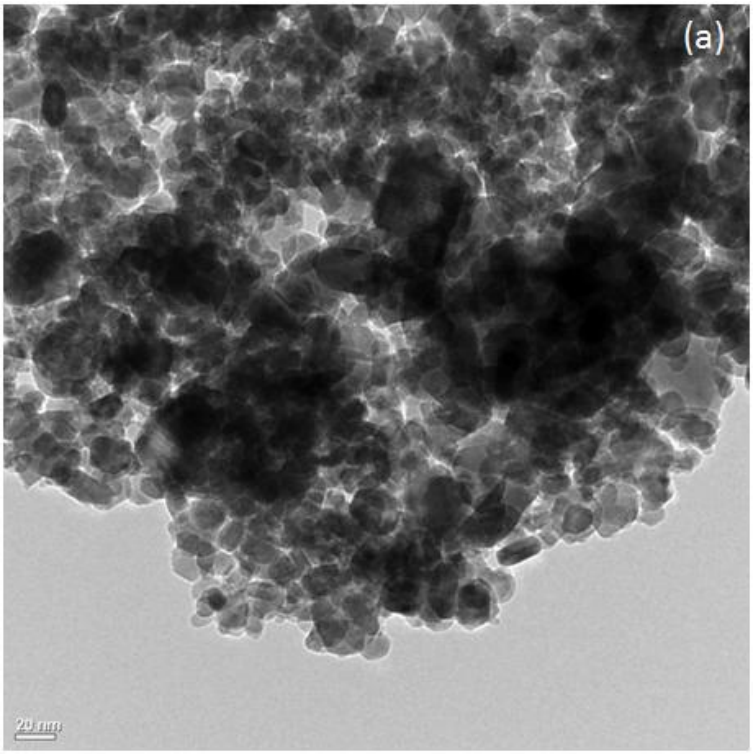

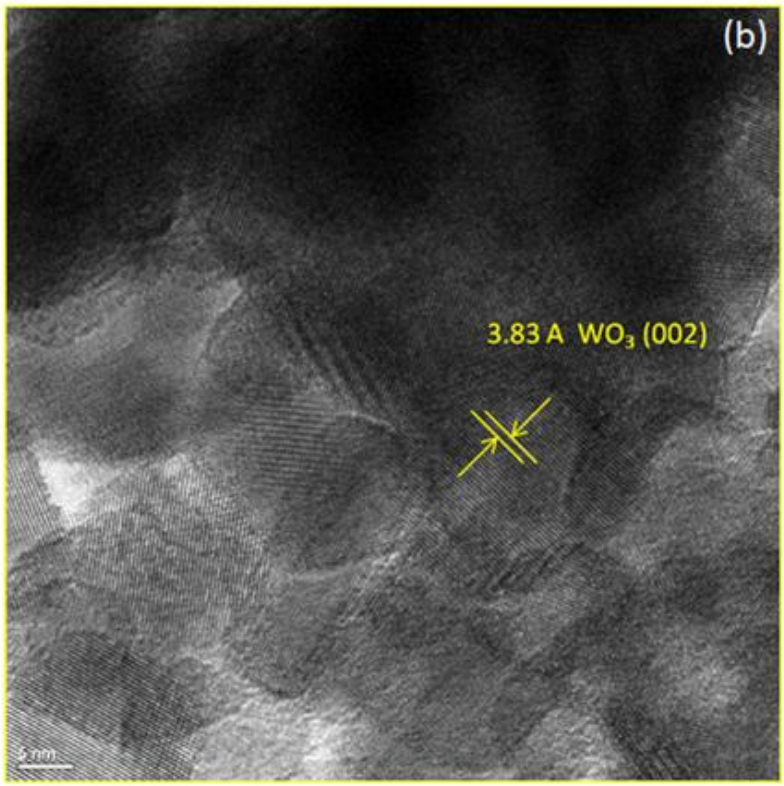

Figure A2.3. HRTEM micrograph of the synthesized WO_3 at different magnification.

The SEM and HRTEM micrograph show agglomerate of WO_3 nanoparticles is spherical approximately 10 – 40 nm in diameter (See Figure A2.2 and 2.3). The majority of the powders are single crystals that are loosely aggregated. The d-spacing measurement result, 3.83 Å, suggests that in accordance with ε-WO_3 (002) (JCPDS No.: 87-2386).

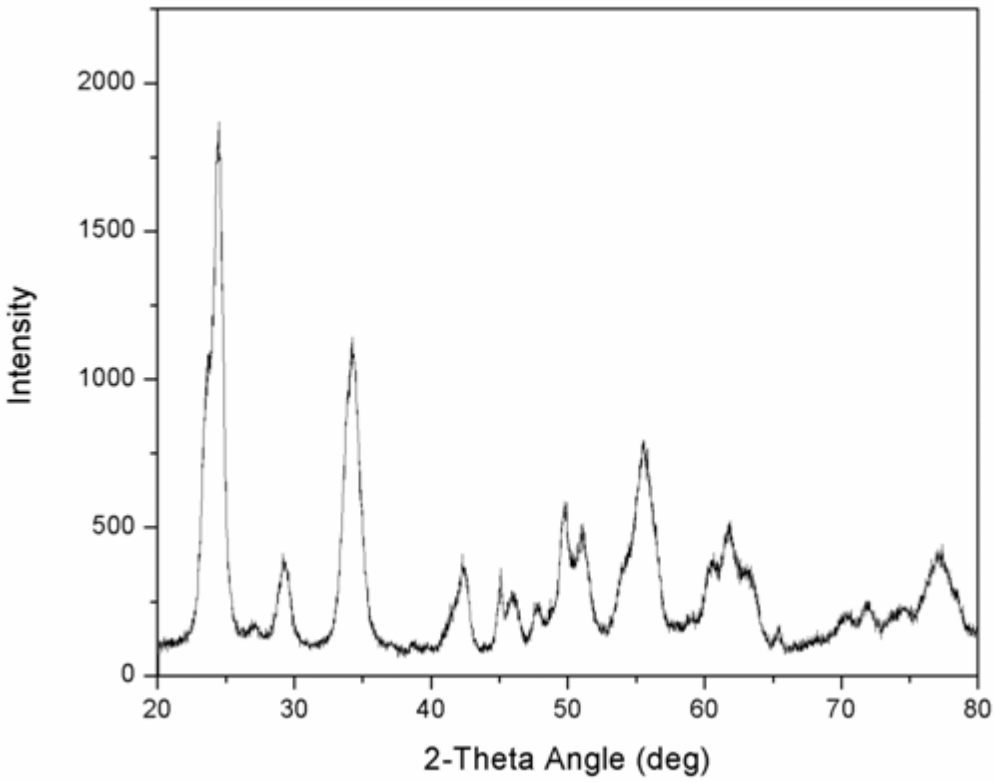

Figure A2.4 X-ray powder diffraction patterns of the WO_3 nanocrystals.

Figure A2.4 shows the XRD patterns of WO_3 nanocrystals prepared from FSP process. The main peaks the size be assigned to monoclinic WO_3 phase (JCPDS No.: 87-2386), respectively. The calculated particle size from the Scherrer's formula was 18 nm corresponding to previous results from TEM analysis.

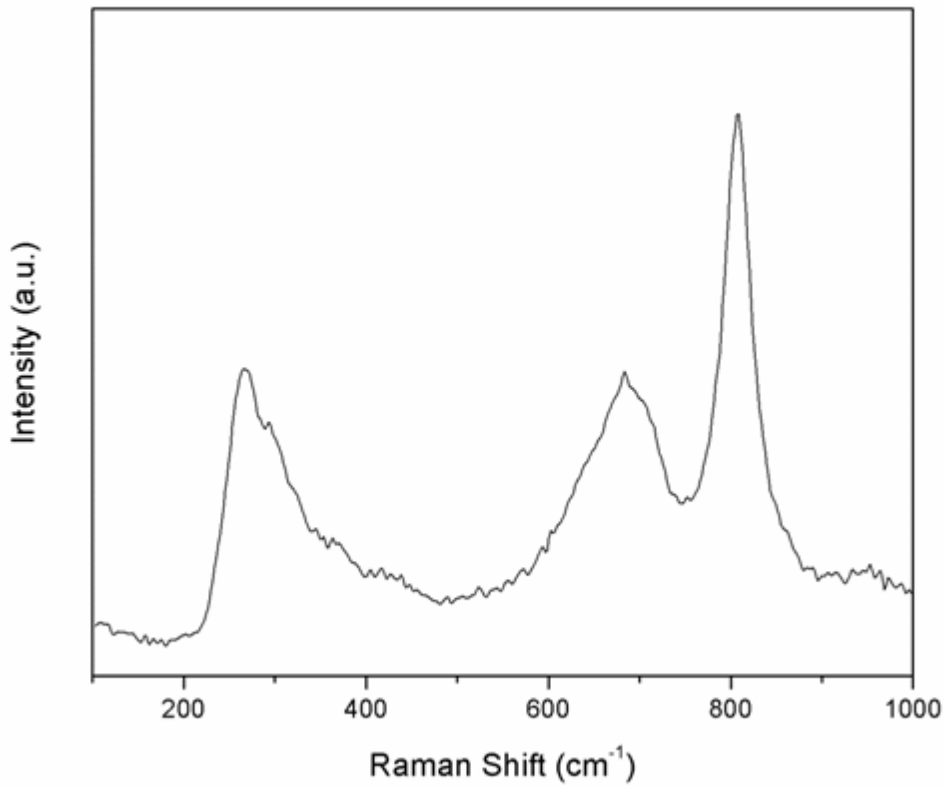

Figure A2.5 Raman spectra of WO_3 microcrystals from FSP process.

Figure A2.5 shows the corresponding raman spectra of WO_3 nanoparticles. The peaks at 272, 303,688 and 805 cm^{-1} acentric ε-phase (space group: *Pc*)[8]. It is clear that as-synthesized WO_3 microcrystals from FSP process contain ε-WO_3.

Nanosized Cu-WO_3 metal oxide particles with 20-40 nm from mixing $Cu(NO_3)_2 \cdot 3H_2O$ and W-iso. Uniform structure and small particle size has advantage for sensing and catalyst applications.

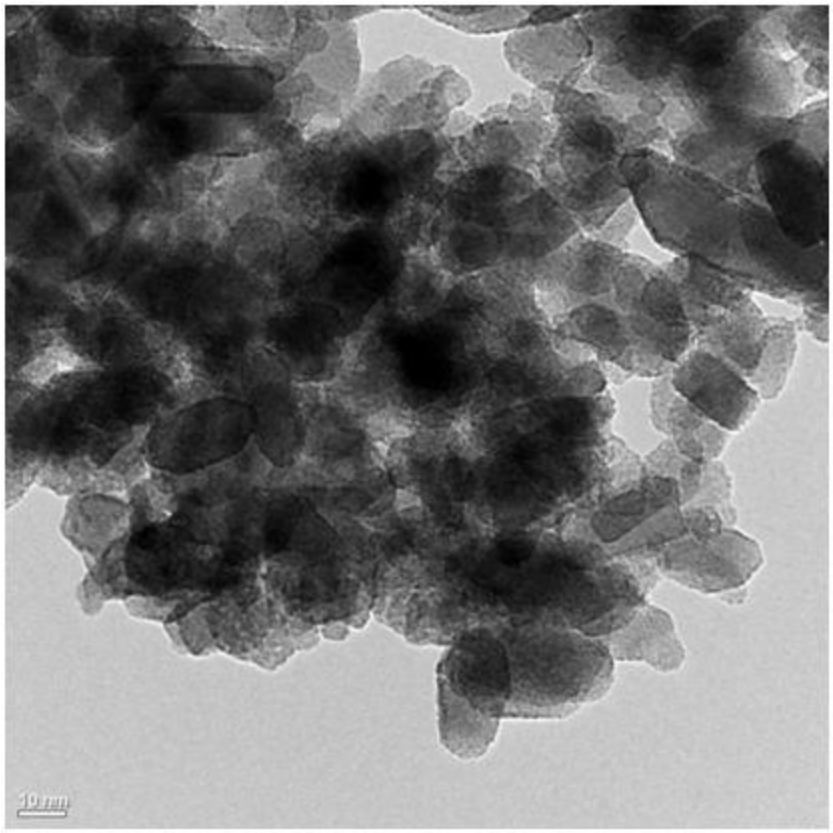

Figure A2.6 10 at% copper doped WO_3 nanoparticles from FSP process.

Appendix 2-B: RT NO sensing by the FSP processed WO3 nanocrystals

Nitrogen Oxides (NO_x= NO + NO_2) are toxic air pollutants, released from automobiles and combustion facilities, with threshold limit values (TLV) as low as 25 ppm for NO and 3 ppm for NO_2 [9]. In addition, a photolytic decomposed NO_2 by solar radiation is one the source of Ozone (O_3), casing smog[10]. Therefore, the need for effective NO_x monitoring becomes highly demanding. Metal oxide gas sensor studies (e.g. SnO_2 [11], ZnO[12], $LaFeO_3$[13]) have shown high sensitive properties to NO_x gases. Among the several metal oxide gas sensors. Stable phase WO_3 gas sensors are well known for stable and high selectivity to NO_x gases [14]. However, the ε-WO3 is a ferroelectric material which has high selectivity to acetone detection [1]. The bulk ε-WO_3 is usually stable at temperatures below -30 ^oC [1]. However, ε-WO_3 also can be stable in room temperature with particle size 5-20 nm [15]. ε-WO_3 is often doped with Cr [1] or SiO2[16] to obtain thermal stability at metal oxide gas sensor operation temperature

(>300^{o}C). In most commercial industries, low power consumption (low temperature) gas sensors are more favorable since it can be incorporated with remote and battery powered applications.

In this work the as-synthesized ε-WO_3 was tested as a RT NO sensor. 0.02g of the synthesized WO_3 powder was mixed with ethanol and the solution is ultrasonically stirred for 30 min. 15 drops of the suspension are deposited on an Pt electrode-coated Al_2O_3 substrate. The substrate is dried in air for 1 h then placed in oven for additional drying at 75℃ for 1h. Above processes repeated 3 times to get uniformly deposited WO_3 sensing substrate.

To NO sensing test, a unilateral gas flow system containing a mixture of N_2 goes through the Electronic nose chamber (EOS v004, Sacmi). The measured resistance is the base line value. When the NO gas sensing test starts, a certain level of NO gases added into the flow at a controlled concentration and the resistance change will be recorded. The measuring temperature was set for room temperature.

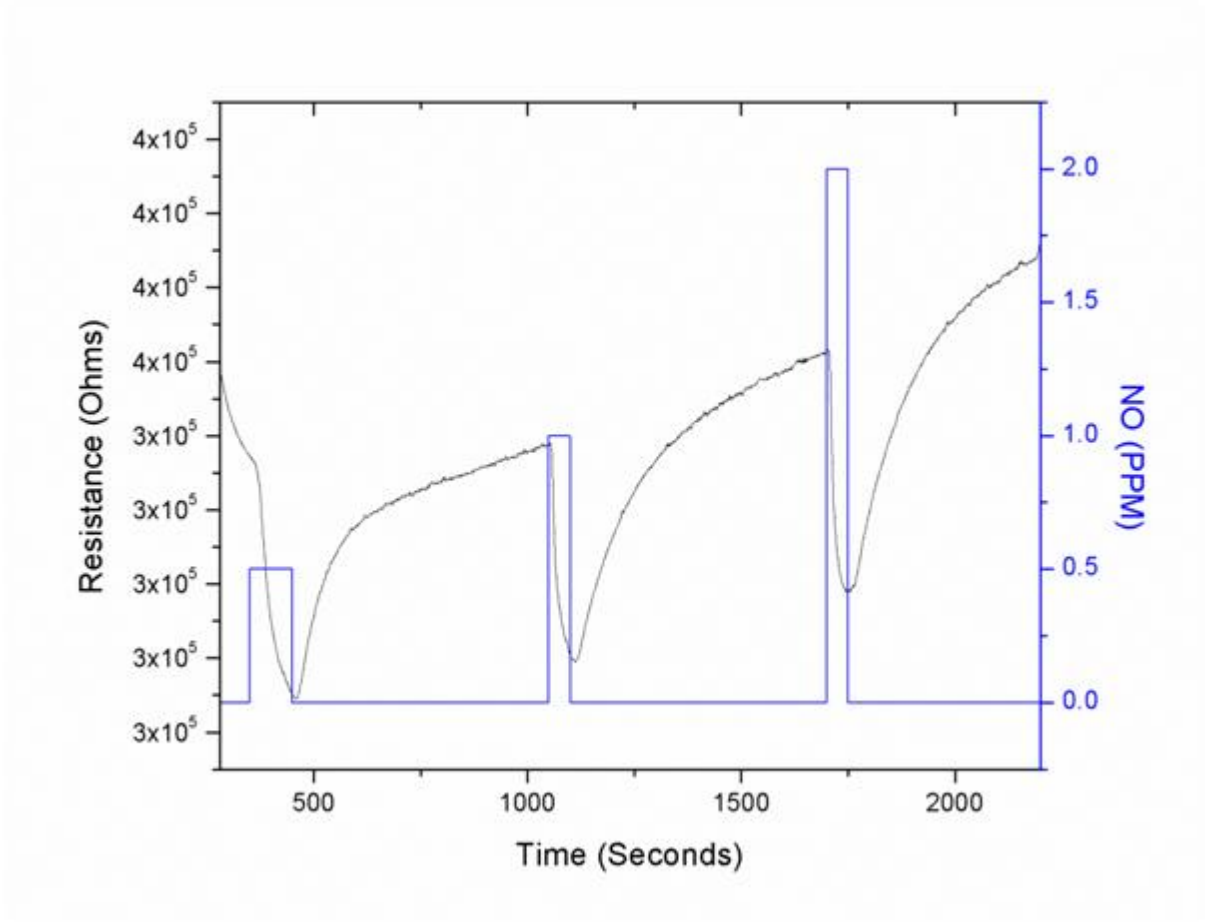

Figure A2.7 A response transients to different concentrations of NO at room temperature.

The sensing properties of fabricated WO_3 exposed to NO were investigated in a dynamic mode switching from nitrogen to the concentration of NO (0.5, 1 and 2 ppm). The response transients of synthesized WO_3 nanocrystals are shown in Figure A2.7. During the injection of 0.5 ppm of NO, the sensor resistance is decrease from 0.337 to 0.305 MOhm and took a few minutes to recover to the baseline with N_2 gas flushing. It showed same trend as increasing N_2 concentration, 1 and 2 ppm. Sharp response of the sensor to NO is indication of sensor quality and is a direct consequence of extremely small particles size and high specific surface area. The resistance base was shifted up during measurements.

In conclusion, ε-WO_3 nanocrystals with uniform diameter (about 18 nm) were synthesized by FSP process. The sensing measurements showed that the synthesized ε-WO_3 nanocrystals are sensitive to NO as low as 500 ppb. High sensitivity with low operating temperature for the sensor is an advantageous. The fast and economical way to produce WO_3 by FSP make this technology important to remote and battery powered sensor applications.

Reference

1. Wang, L., et al., *Ferroelectric WO3 Nanoparticles for Acetone Selective Detection.* Chemistry of Materials, 2008. **20**(15): p. 4794-4796.

2. Wegner, K. and S.E. Pratsinis, *Scale-up of nanoparticle synthesis in diffusion flame reactors.* Chemical Engineering Science, 2003. **58**(20): p. 4581-4589.

3. Teoh, W.Y., R. Amal, and L. Madler, *Flame spray pyrolysis: An enabling technology for nanoparticles design and fabrication.* Nanoscale, 2010. **2**(8): p. 1324-1347.

4. Strobel, R., A. Alfons, and S.E. Pratsinis, *Aerosol flame synthesis of catalysts.* Advanced Powder Technology, 2006. **17**(5): p. 457-480.

5. Ulrich, G.D., *Theory of Particle Formation and Growth in Oxide Synthesis Flames.* Combustion Science and Technology, 1971. **4**(1): p. 47-57.

6. Marshall, B.S., I. Telford, and R. Wood, *A field method for the determination of zinc oxide fume in air.* Analyst, 1971. **96**(1145): p. 569-578.

7. Sokolowski, M., et al., *The "in-flame-reaction" method for Al2O3 aerosol formation.* Journal of Aerosol Science, 1977. **8**(4): p. 219-230.

8. Arai, M., et al., *Raman studies of phase transitions in gas-evaporated WO3 microcrystals.* Solid State Communications, 1990. **75**(7): p. 613-616.

9. Ho, J.-J., *Novel nitrogen monoxides (NO) gas sensors integrated with tungsten trioxide (WO3)/pin structure for room temperature operation.* Solid-State Electronics, 2003. **47**(5): p. 827-830.

10. Comini, E., G. Faglia, and G. Sberveglieri, *UV light activation of tin oxide thin films for NO2 sensing at low temperatures.* Sensors and Actuators B: Chemical, 2001. **78**(1–3): p. 73-77.

11. Williams, G. and G.S.V. Coles, *NOx response of tin dioxide based gas sensors.* Sensors and Actuators B: Chemical, 1993. **16**(1–3): p. 349-353.

12. Matsushima, S., et al., *NO2 GAS-SENSING PROPERTIES OF GA-DOPED ZNO THIN-FILM.* Sensors and Actuators B-Chemical, 1993. **14**(1-3): p. 621-622.

13. Traversa, E., et al., *NO2 sensitive LaFeO3 thin films prepared by r.f. sputtering.* Sensors and Actuators B: Chemical, 1995. **25**(1–3): p. 661-664.

14. Akiyama, M., et al., *Tungsten Oxide-Based Semiconductor Sensor Highly Sensitive to NO and NO₂*. Chemistry Letters, 1991. **20**(9): p. 1611-1614.

15. Hayashi, S., et al., *Phase Transitions in Gas-Evaporated WO₃ Microcrystals: A Raman Study.* Journal of the Physical Society of Japan, 1992. **61**(3): p. 916-923.

16. Righettoni, M., A. Tricoli, and S.E. Pratsinis, *Thermally Stable, Silica-Doped ε-WO3 for Sensing of Acetone in the Human Breath.* Chemistry of Materials, 2010. **22**(10): p. 3152-3157.